12-15-2020

Development of Multiscale Spectro-microscopic Imaging System and Its Applications

Fei Zhao

Recommended Citation

Zhao, Fei, "Development of Multiscale Spectro-microscopic Imaging System and Its Applications." Dissertation, Georgia State University, 2020.
doi: https://doi.org/10.57709/20307578

DEVELOPMENT OF MULTISCALE SPECTRO-MICROSCOPIC IMAGING SYSTEM AND ITS APPLICATIONS

by

FEI ZHAO

Under the Direction of Ning Fang, PhD

ABSTRACT

A novel multi-modality spectro-microscopic system that combines far-field interferometry based optical microscopy imaging techniques (differential interference contrast microscopy and cross-polarized light microscopy), total internal reflection microscopy (total internal reflection fluorescence and scattering microscopy) and confocal spectroscopy (Raman spectroscopy and photoluminescence spectroscopy) is developed. Home-built post treatment stages (thermal annealing stage and solvent annealing stage) are integrated into the system to realize *in situ* measurements. Departing from conventional characterization methods in materials science mostly focused on structures on one length scale, the *in situ* multi-modality characterization system aims to uncover the structural information from the molecular level to the mesoscale. Applications of the system on the characterization of photoactive layers of bulk heterojunction solar cell, two-dimensional materials, gold nanoparticles, fabricated gold nanoparticle arrays and cells samples are shown in this dissertation.

INDEX WORDS: Interferometric optical microscopy, Raman spectroscopy, Photoluminescence spectroscopy, Multiscale *in situ* characterization

DEVELOPMENT OF MULTISCALE SPECTRO-MICROSCOPIC IMAGING SYSTEM AND ITS APPLICATIONS

by

FEI ZHAO

A Dissertation Submitted in Partial Fulfillment of the Requirements for the Degree of

Doctor of Philosophy

in the College of Arts and Sciences

Georgia State University

2020

DEVELOPMENT OF MULTISCALE SPECTRO-MICROSCOPIC IMAGING SYSTEM AND ITS APPLICATIONS

by

FEI ZHAO

Committee Chair: Ning Fang

Committee: Gangli Wang
Gregory Poon

Electronic Version Approved:

Office of Graduate Services
College of Arts and Sciences
Georgia State University
December 2020

DEDICATION

I would like to thank the help and support of my parents. Their understanding and love support me during my downtime in pursuing the degree and to pursue my dream. I would like to thank my advisor and mentor Dr. Ning Fang, who is always patient and understanding to his students and willing to share his career experience as a mentor to his students. I also would like to thank every lab member in Dr. Fang's lab who has discussed with me, offered their advice to me when I have questions in my research and encouraged me when my experiments failed.

ACKNOWLEDGEMENTS

I would like to thank my advisor and mentor Dr. Ning Fang for his help in my writing this dissertation. I also would like to thank my dissertation committee members: Dr. Gangli Wang and Dr. Gregory Poon for their advice and help for me to finish this dissertation.

TABLE OF CONTENTS

ACKNOWLEDGEMENTS V

LIST OF TABLES XI

IST OF FIGURES.. XII

LIST OF ABBREVIATIONS XX

1 GENERAL INTRODUCTION... 1

1.1 Dissertation Organization 1

1.2 Introduction to Differential Interference Contrast (DIC) Microscopy.................. 1

1.3 Introduction to Cross-polarized Light Microscopy 3

1.4 Introduction to Total Internal Reflection Fluorescence/Scattering Microscopy ... 4

1.5 Introduction to Raman Spectroscopy 6

1.6 Introduction to Photoluminescence Spectroscopy 7

1.7 Introduction to Spectro-microscopic Imaging System 7

1.7.1 Integration of Optical Microscopy with Raman Spectroscopy 8

1.7.2 Integration of Optical Microscopy with Infrared Spectroscopy 9

1.7.3 Integration of Optical Microscopy with Transient Absorption Spectroscopy...... 10

1.7.4 Integration of Optical Microscopy with Fluorescence Spectroscopy................... 11

2 DEVELOPMENT OF MULTISCALE SPECTRO-MICROSCOPIC IMAGING SYSTEM 17

2.1 Introduction.. 17

2.2 Experimental Section 19

2.3 Results and Discussion 20

2.3.1 Reflected Differential Interference Contrast (DIC) Microscopy Module 20

2.3.2 Reflected Cross-polarized Light Microscopy Module 22

2.3.3 Total Internal Reflection Microscopy Module 22

2.3.4 Confocal Spectroscopy Module 23

2.3.5 Post Treatment Sample Stages Module 24

2.4 Conclusions 24

2.5 Figures 25

3 IN SITU CHARACTERIZATION OF PHOTOACTIVE LAYERS IN BULK HETEROJUNCTION SOLAR CELL UNDER THERMAL STRESS BY THE MULTI-MODALITY MULTISCALE SPECTRO-MICROSCOPY IMAGING SYSTEM 30

3.1 Introduction 30

3.2 Sample Preparation and Experimental Measurements 34

3.2.1 Film Preparation 34

3.2.2 Temperature Control 35

3.2.3 Cross-polarized Light Microscopy Images Measurement 35

3.2.4 Raman Spectroscopy Measurement 35

3.2.5 Photoluminescence Measurement 35

3.3 Data Analysis 36

3.3.1 Cross-polarized Light Microscopy Images Analysis 36

3.3.2 Raman Spectra Analysis 38

3.3.3 Photoluminescence Spectra Analysis 39

3.3.4 T_{cc}^{min}, T_{cc}^{max} and T_{cc} Calculation 40

3.4 Results and Discussion 41

3.4.1 Thermotropic Realignment of Mesoscale Orientational Ordered Domains Characterized by Cross-polarized Light Microscopy Module under Thermal Stress 41

3.4.2 Thermotropic Evolution of Relative Crystallinity (Molecular Order) of Photoactive Layers Characterized by Confocal Raman Spectroscopy Module under Thermal Stress 43

3.4.3 Thermotropic Transformation of Aggregate Type Characterized by Confocal Photoluminescence Spectroscopy Module under Thermal Stress 45

3.4.4 Multiscale Evolution of the Photoactive Layers in Bulk Heterojunction Solar Cells 46

3.4.5 Effect of Programmable Temperature Dropping and Uncontrolled Temperature Dropping Processes on the Photoactive Layers in Bulk Heterojunction Solar Cells 48

3.5 Conclusion 49

3.6 Figures 50

4 OTHER APPLICATIONS OF THE MLTI-MODALITY SPECTRO-MICROSCOPY IMAGING SYSTEM 71

4.1 Introduction 71

4.2 Sample Preparation and Experimental Measurement 72

4.2.1 Isotropic Nanospheres and Anisotropic Nanorods 72

4.2.2 Graphene 72

4.2.3 Bulk Heterojunction Solar Cell Photoactive Layers 73

4.2.4 Cells 73

4.3 Results and Discussion 73

4.3.1 Characterization of Nanomaterials 73

4.3.2 3D Scanning of Cell Samples 77

4.4 Conclusions 77

4.5 Figures 79

5 LOCALIZATION ACCURACY OF GOLD NANOPARTICLES IN SINGLE PARTICLE ORIENTATION AND ROTATIONAL TRACKING 87

5.1 Abstract 87

5.2 Introduction 88

5.3 Experimental Section 89

5.3.1 Sample Slide Preparation 89

5.3.2 Instrumentation 90

5.3.3 Computer Simulation of DIC PSFs 90

5.3.4 Shear Distance Measurement 91

5.3.5 Gold Nanorod Localization-Weighing Algorithm 92

5.4 Results and Discussion 92

5.4.1 Localization Uncertainty for Inclined Gold Nanorods 92

5.4.2 Lateral Shear of DIC Microscope 94

5.4.3 Experimental and Simulated DIC Images 95

5.4.4 Improving Localization Accuracy with Measured Shear Distance 96

5.4.5 Localization Accuracy and Precision in Real DIC Images 97

5.5 Conclusions 98

5.6 Figures 100

6 OVERALL CONCLUSIONS 107

REFERENCES 109

LIST OF TABLES

Table 1. Shear distances for different configurations. 102

IST OF FIGURES

Figure 1.1 Schematic light path of transmitted DIC microscope.. 12

Figure 1.2. Total internal reflection illumination light path. 13

Figure 1.3. Schematic light path of objective-based TIRF/TIRS microscopy............................ 14

Figure 1.4. Schematic light path of prism-type TIRF/TIRS. 15

Figure 1.5. Jablonski energy diagram of stokes Raman scattering, anti-stokes Raman scattering and resonance Raman scattering processes.. 16

Figure 2.1 (A)Instrumentation scheme; Components with dashed outline are removeable among different modules; M:Mirror; L:Lens; F:Filter; B/D: Beamsplitter or Dichoric Mirror; P:Polarizer; A:Analyzer; FM: Flip Mirror; TL: Tube lens; NP: Nomarski prism. (B)Thermal annealing stage and its temperature controller. (C)Solvent annealing stage. (D)Prism-type TIRF/TIRS sample stage. 25

Figure 2.2. Schematic light path of reflected DIC microscope.. 26

Figure 2.3. Schematic light path of reflected cross-polarized light microscope.......................... 27

Figure 2.4. Schematic light path of prism-type TIRF/TIRS. 28

Figure 2.5. (A)Schematic light path of the confocal spectroscopy module. (B) Schematic light path of total internal reflection scattering light path.. 29

Figure 3.1. Schematic illustration of charge transport in conjugated polymers. 50

Figure 3.2. Schematic setup of cross-polarized light microscope and the sample. 51

Figure 3.3. Optical microscopy images of a 1:1 P3HT: PCBM blend thin film and their corresponding image intensity distributions. (A) The crossed-polarized light microscopy image. (B) The bright field microscopy image. (C) Image intensity distribution of the

crossed-polarized light microscopy image in (A). (D) Image intensity distribution of the bright field microscopy image of (B)... 52

Figure 3.4. Raman spectra of regio-regular (RR) P3HT and regio-random (RRa) P3HT. 53

Figure 3.5. Raman spectrum of the (A) as-cast and (B) annealed P3HT: PCBM blend thin film. The Raman spectra are obtained by averaging the spectra obtained at 10 different regions in the sample area... 54

Figure 3.6. Approximate Jablonski diagram of ideal (A) H-aggregates and (B) J-aggregates corresponding to the weak exciton coupling regimes. 55

Figure 3.7. Photoluminescence (PL) spectrum of the (A) as-cast and (B) annealed P3HT: PCBM blend thin film. The photoluminescence spectra are obtained by averaging the spectra obtained at 10 different regions in the sample area. 56

Figure 3.8. The evolution of crystallinity under thermal stress and the first derivative curve of the crystallinity fitting curve. Tc is the cold crystallization temperature, which is identified by the peak position of the first derivative curve. The solid line is the sigmoid fitting line of the change of crystallinity with temperature. 57

Figure 3.9. (A)The cross-polarized light microscopy image of P3HT: PCBM blend thin film on Si substrate. (B) Image intensity distribution of (A). The scale bar is 5 µm. 58

Figure 3.10. The evolution of P3HT: PCBM blend thin film under the cross-polarized light microscopy. The scale bar is 2.5 µm. 59

Figure 3.11. Thermotropic evolution of image intensity distributions of 1:1 P3HT: PCBM photoactive layer from 20°C to 100 °C. 60

Figure 3.12. The change of overlap percentage of peak 1, peak 2 and peak 2, peak 3 in Figure 3.11 with temperature. The dash line is a guide to show the potential trend. 61

Figure 3.13. The evolution of Raman spectra of P3HT: PCBM blend thin film. 62

Figure 3.14. Raman spectra of 1:1 P3HT: PCBM blend thin film from 20°C to 100 °C. The Raman spectra are obtained by averaging the spectra obtained at 10 different regions in the sample area. 63

Figure 3.15. The evolution of crystallinity calculated from Raman spectra. The solid line is the sigmoid fitting line of the change of crystallinity with temperature. The error bars show the standard deviations of 10 measurements. 64

Figure 3.16. The evolution of Photoluminescence (PL) spectra of the P3HT: PCBM blend thin film. 65

Figure 3.17. Photoluminescence (PL) spectra of 1:1 P3HT: PCBM blend thin film from 20°C to 100 °C. The PL spectra are obtained by averaging the spectra obtained at 10 different regions in the sample area. 66

Figure 3.18. The evolution of I_{0-0}/I_{0-1} calculated from PL spectra. The dash line is the two piecewise linear fitting of the change of I_{0-0}/I_{0-1} with temperature. The error bars show the standard deviations of 10 measurements. 67

Figure 3.19. Proposed mechanism of the thermal evolution process. 68

Figure 3.20. Comparison of 1:1 P3HT: PCBM blend thin film processed by programmed and uncontrolled temperature dropping. (a)The top two images are the P3HT: PCBM blend thin films as-cast and its corresponding film after programmed temperature dropping (PTD), respectively. The bottom two images are the P3HT: PCBM blend thin films as cast and its corresponding film after uncontrolled temperature dropping (UTD), respectively. (b)Typical Raman spectra of as-cast, PTD and UTD P3HT: PCBM blend thin film. (c)Typical PL spectra of as-cast, PTD and UTD P3HT: PCBM blend thin films.

(d)The I_{0-0}/I_{0-1} and crystallinity of as-cast, PTD and UTD P3HT: PCBM blend thin films. The error bars show the standard deviations of 10 measurements. 69

Figure 3.21. Cross-polarized light microscopy images of 1:1 P3HT: PCBM blend thin film (A) As-cast. (B) After programmed temperature drop (PTD). (C) Image intensity distribution of (A). (D) Image intensity distribution of (B). Cross-polarized light microscopy images of 1:1 P3HT: PCBM blend thin film (E) As-cast. (F) After uncontrolled temperature drop (UTD). (G) Image intensity profile of (E). (H) Image intensity profile of (F). The scale bar is 5 μm. 70

Figure 4.1. Examples of PS nanobeads and gold nanospheres imaged under RDIC. (A-C) correspond to 80 nm, 60 nm, and 40 nm gold nanospheres in diameter respectively. (D) is the same area as (C) with 20 images summed. (E-H) correspond to 240 nm, 200 nm, 150 nm, and 100 nm in diameter PS nanospheres respectively. All exposure times are 50 ms. Scale bar is 2 μm... 79

Figure 4.2. Gold nanorods (40x118 nm) imaged under RDIC. (A) Random assortment of AuNRs with different 3D orientations. (B-F) Examples of AuNRs with different in-plane orientations. Patterns range from nearly completely dark to nearly completely bright. (G-F) Examples of AuNRs with different 3D orientations. The positions of the dark and bright “lobes” are orientation dependent. All images are the sum of 20 frames exposed for 50 ms. Scale bar is 2 μm. 80

Figure 4.3. RDIC images of a gold nanorod (40x118 nm) imaged at different in-plane orientations. (A). The in-focus image patterns of the gold nanorod at different orientations relative to the optical axes. The sample slide is rotated from 10° to 360° in 10° per per step. The scale bar represents 1 μm. (B). The normalized bright part (red) and

dark part intensities (blue)of the images on the top in each pair. Periodic changes of the bright/dark intensities of a gold nanorod when rotating under a DIC microscope and being illuminated at the 700 nm wavelengths. All intensities are relative to the background level. (C). Schematic illustration of a fixed dipole with polar angle ψ and azimuthal angle θ. One of the polarization direction (x-axis) may be referred to as the dark optical axis because a gold nanorod would generate a nearly all dark image when its long axis is aligned with this polarization direction; similarly, the other orthogonal polarization direction (y-axis) may be called the bright optical axis in accordance to the presentation of nearly all bright DIC image 81

Figure 4.4. Characterization of monolayer graphene made by chemical vapor deposition. (A) Bright field microscopy image of the film on Si substrate. (B) RDIC microscopy image of the same sample area in (A) on Si substrate. The scale bar is 5 µm. (C) Raman spectra of the area 1 and 2 (pointed by the arrows) in the sample in (B)..................................... 82

Figure 4.5. SEM and RDIC images of nanostructures fabricated in silica wafer templates at orientational angles of 0, 45 and 90 degrees. Monomers within the template (A) SEM. RDIC image with (B) 0 degrees orientation. (C) 45 degrees orientation. (D) 90 degrees orientation. Dimers within the template (E) SEM. RDIC image with (F) 0 degrees orientation. (G) 45 degrees orientation. (H) 90 degrees orientation. Trimers within the template (I) SEM. RDIC image with (J) 0 degrees orientation. (K) 45 degrees orientation. (L) 90 degrees orientation. Tetramers within the template (M) SEM. RDIC image with (N) 0 degrees orientation. (O) 45 degrees orientation. (P) 90 degrees orientation. RDIC images taken with 100 ms exposure. the scale bar of SEM images is 500 nm and RDIC images is 2 µm. 83

Figure 4.6. Characterization of 1:1 P3HT: PCBM blend thin film at room temperature. (A) Bright field microscopy image of the film on Si substrate. (B) RDIC microscopy image of the same film on Si substrate. The scale bar is 5 μm. (C) Raman and (D) PL spectra of the same sample in (B). (E) A PCBM crystal in P3HT matrix. (F) Image intensity and crystallinity of P3HT along the dotted red line. Each scanning step is 500 nm. The Raman and PL spectra are averaged from 10 measurements in the sample area. 84

Figure 4.7. RDIC image of A549 cell samples on Si wafer. 85

Figure 4.8. 3D scanning of A549 Cells on Si wafer. 86

Figure 5.1 (a) Schematic illustration of a fixed dipole with polar angle ψ and azimuthal angle θ. One of the polarization direction (x-axis) may be referred to as the dark optical axis because a gold nanorod would generate a nearly all dark image when its long axis is aligned with this polarization direction; similarly, the other orthogonal polarization direction (y-axis) may be called the bright optical axis in accordance to the presentation of nearly all bright DIC image. These definitions of optical axes are used consistently in all the experimental and simulated images of gold nanorods in this study. (b) Experimental DIC images of a gold nanorod with the azimuthal angles from 0° to 180° in 15° steps. Note that 0° and 180° are equivalent due to the symmetry. (c) The corresponding bright-part intensity (blue) and dark-part intensity (red) traces for the experimental DIC images in b. (d) Computer simulated DIC images of a gold nanorod with a polar angle of 90° and azimuthal angles from 0° to 180° in 15° steps. (e) The corresponding bright-part intensity (blue) and dark-part intensity (red) traces for the simulated DIC images in d. 100

Figure 5.2 Two intermediate bright-field images of an 80-nm gold nanosphere obtained when the angle between the first and second polarizer is (a) 45° and (b) -45°. (c) The merged image. The two crosses are the centers of the two intermediate bright-field images (a) and (b) by fitting with 2D Gaussian functions. The distance between the two centers is the shear distance. The shear direction is from northwest to southeast, which is indicated by the relative positions of the two centers. 101

Figure 5.3 Experimental and simulated DIC images of (a) a 40 nm × 118 nm gold nanorod (90° polar angle and 45° azimuthal angle) and (b) an 80-nm gold nanosphere under 540 or 700 nm incident light with either Nikon standard/high-contrast (100XI) or high-resolution (100XI-R) prisms. 103

Figure 5.4 (a) Localization of the simulated gold nanorod images with a constant polar angle of 90˚ and various azimuthal angles. Red and blue: the x and y coordinates of the weighed centers of the bright part. Black and green: the x and y coordinates of the weighed centers of the dark part. Cyan and magenta: the x and y coordinates of the midpoint between the weighed centers of the bright part and dark part. Grey and yellow: the x and y centroid coordinates of the gold nanorod when either bright or dark part dominates. Yellow squares are hardly visible in the figure because they are closely overlapped with grey squares. (b) Standard deviations of the localized x (black) and y (red) coordinates of gold nanorods at four polar angles: 45˚, 60˚, 75˚and 90˚. Each data point is calculated from the simulated images with various azimuthal angles from 0-180˚, in 5˚ step size. The localization is determined from the weighed centers of the bright part and the dark part of the images. 104

Figure 5.5 Localization of the simulated gold nanorod images with constant polar angles at 75° (a), 60° (b) and 45° (c) and with various azimuthal angles. Red and blue: the x and y coordinates of the weighed center of the bright part. Black and green: the x and y coordinates of the weighed center of the dark part. Cyan and magenta: the x and y coordinates of the midpoint between the weighed centers of the bright part and dark part. Grey and yellow: the x and y centroid coordinates of the gold nanorod when either the bright or dark part dominates; they are calculated as the weighed bright center minus half of the shear distance or the weighed dark center plus half of the shear distance. 105

Figure 5.6 (a). The DIC images of two neighboring gold nanorods (labeled with 1 and 2) during 360° in-plane rotation. The scale bar represents 2 μm. (b) The bright (blue) and dark (red) DIC intensity traces of particle 1 (solid square) and 2 (hollow square) during the 360° in-plane rotation. (c) Localization of particle 2 relative to the position of particle 1. The radius of the green circle indicates the average distance between these two particles. 106

LIST OF ABBREVIATIONS

Differential Interference Contrast (DIC)

Cross-polarized Optical Microscopy (PM)

Photoluminescence (PL)

Total Internal Reflection Fluorescence (TIRF)

Total Internal Reflection Scattering (TIRS)

Bulk Heterojunction (BHJ)

Two-dimensional (2D)

Charge-coupled Device (CCD)

Numerical Aperture (N.A.)

Three-dimensional (3D)

Total Internal Reflection (TIR)

Infrared (IR)

Synchrotron Fourier Transform Infrared (S-FTIR)

Direct Stochastic Optical Reconstruction Microscopy (dSTORM)

Transient Absorption (TA)

Electron-multiplying CCD (EMCCD)

Reflected Differential Interference Contrast (RDIC)

Electron Microscopy (EM)

Atomic Force Microscopy (AFM)

Bulk Heterojunction (BHJ)

Organic Photovoltaics (OPVs)

Light-emitting Diodes (LEDs)

Field-effect Transistors (FETs)

Grazing Incidence X-ray Scattering (GIXS)

Differential Scanning Calorimetry (DSC)

Atomic Force Microscopy (AFM)

Transmission Electron Microscopy (TEM)

Scanning Electron Microscopy (SEM)

Poly(3-hexylthiophene) (P3HT)

[6,6]-phenyl C61 Butyric Acid Methyl Ester (PCBM)

Power Conversion Efficiency (PCE)

Regioregular P3HT (RR-P3HT)

Regiorandom P3HT (RRa-P3HT)

Programmed Temperature Dropping (PTD)

Uncontrolled Temperature Dropping (UTD)

Surface Enhanced Raman Scattering (SERS)

Surface Plasmon Resonance (SPR)

Anisotropic Gold Nanorods (AuNRs)

Chemical Vapor Deposition (CVD)

Full Width at Half Maximum (FWHM)

Single Particle Orientation and Rotational Tracking (SPORT)

Fluorescence Imaging with One-nanometer Accuracy (FIONA)

Point Spread Function (PSF)

Localized Surface Plasmon Resonance (LSPR)

1 GENERAL INTRODUCTION

1.1 Dissertation Organization

This dissertation is composed of six chapters. Chapter 1 is the general introduction of the dissertation. It includes the overall organization, introduction to spectro-microscopic techniques, and their applications. It also includes the introductions of optical microscopic and spectroscopic techniques that are integrated in the design of the multi-modality multiscale spectro-microscopic imaging system: differential interference contrast (DIC) microscopy, cross-polarized light microscopy (PM), total internal reflection fluorescence and scattering (TIRF/TIRS) microscopy, Raman spectroscopy, and photoluminescence (PL) spectroscopy. Chapter 2 describes the development of the multi-modality multiscale spectro-microscopic imaging system. Instrumentation details about each module in the multiscale spectro-microscopic imaging system are discussed in this chapter. Chapter 3 is the application of the multi-modality spectro-microscopic imaging system on the *in situ* multiscale characterization of photoactive layers in bulk heterojunction (BHJ) solar cells under thermal stress. Chapter 4 is the applications of the multi-modality multiscale spectro-microscopic imaging system on nanoparticles, two-dimensional (2D) materials, fabricated gold nanoarrays and cell samples. Chapter 5 is the study of localization accuracy of gold nanoparticles in single particle orientation and rotational tracking under DIC microscopy. Chapter 6 is the overall conclusion of the dissertation.

1.2 Introduction to Differential Interference Contrast (DIC) Microscopy

DIC microscopy introduced by Nomarski in the 1950s (1), is in principle an interferometric detection technique capable of visualizing objects below the diffraction limit of light without fluorescence labeling (2; 3). It has been used for decades to visualize cellular samples with higher contrast, better resolution, and shallower depth of field than other far-field optical imaging techniques (4; 5). In addition, spectrally resolved DIC microscopy has been developed for multiplexing imaging (2; 6). Over the last decade, DIC microscopy has been transformed into a primary research tool for single particle orientation and rotational tracking (SPORT) of plasmonic nanoparticles in various chemical and biological systems (7-11).

In the transmitted DIC setup (Figure 1.1), light firstly passes through a linear polarizer. The linearly polarized light passes through the first Nomarski prism to generate two orthogonally polarized light which are mutually shifted by a shear distance along the shear direction. Then the two sheared light beams are collimated by the condenser and shine on the sample. The two light beams after passing through the sample are collected by the objective and recombined by the second Nomarski prism. Finally, the recombined light beam passes through a second linear polarizer (also called analyzer) and generates interference images of the sample which are detected by the charge-coupled device (CCD) camera.

Benefitting from the high numerical apertures (N.A.) of the objective and condenser used in DIC microscopy, DIC microscopy can provide higher lateral and axial resolutions than bright-field and dark-field microscopies (4). Three-dimensional (3D) DIC microscopy has been developed by taking advantage of the optical sectioning capability (better axial resolution) of DIC microscopy and harnessed to study a complete cell division process in situ (12). Moreover, live cells and their morphology changes without staining can be monitored by DIC microscopy *in situ*. For example, DIC microscopy has been used to characterize the diffusion and transport of nanoprobes and cell morphology changes during the endocytosis process of live cells (2; 13).

Resulting from the working principle of interference, DIC images of nanoparticles show bright and dark patterns, in which the 2D Gaussian fitting methods cannot be used in the study of localization of nanoparticles (4; 14). In chapter 5, the localization accuracy and inherited uncertainties of gold nanoparticles in single particle orientation and rotational tracking using DIC microscopy is studied with the assistance of computer simulation. These discussions provide guidance for researchers to properly evaluate their data and avoid making claims beyond the technical limits. The understanding of the intrinsic localization errors and the principle of DIC microscopy also leads us to propose a new localization strategy that utilizes the experimentally-measured shear distance of the DIC microscope to improve the localization accuracy (14).

1.3 Introduction to Cross-polarized Light Microscopy

For more than a century, cross-polarized light microscopy has been applied to characterize submicroscopic alignments in specimens that are usually unrevealed and invisible under other optical microscopy techniques (15). Images generated under a cross-polarized light microscope result from the interaction between polarized incident light and polarizable chemical bonds in regioregular molecules and are orientationally sensitive. Phase shifts between sampling beams due to the different refractive indexes along different optical axes of birefringent samples lead to interference patterns of the sample and reveal submicroscopic orientational information. Moreover, cross-polarized light microscopy can also provide quantitative measurements such as phase retardation, which can be used to calculated refractive index differences and the thicknesses of samples (16; 17).

In 2015, Shribak et al. developed the polychromatic polarization microscope and realized direct characterization of both phase retardance and slow-axis orientation in samples (15; 18). Dynamic changes of birefringence in samples such as various types of fast-moving bdelloid rotifers were successfully characterized by polychromatic polarization microscope (18). In 2016, Mehta et al. invented an instantaneous fluorescence polarizing microscope in which total internal reflection (TIR) illumination was combined with custom image splitter to image fluorescence emission signals along four polarization directions and realize orientation and position tracking of single molecules in live cells (19).

The transmitted cross-polarized light microscopy setup is the same as transmitted DIC microscopy without the pair of Nomarski prism (Figure 2.1), light firstly passes through a linear polarizer. Then the linearly polarized light passes through the birefringent sample to generate two orthogonally polarized light with different phase information of the sample which are then collected by the objective. The two orthogonally polarized light beams project onto the transmission axis of a second linear polarizer (also called analyzer) and interfere with each other. Finally, interference images are detected by the camera.

1.4 Introduction to Total Internal Reflection Fluorescence/Scattering Microscopy

Total internal reflection fluorescence microscopy (TIRFM) is arguably the most sensitive mode of fluorescence microscopy and has been successfully applied in studies of chemistry (20-24), biochemistry (25-27) and biology (28-30). Under total internal reflection (TIR) illumination (Figure 1.2), the incident angle of light is varied upon a material with a high index of refraction (n1). At angles beyond the critical angle, the incident light is completely reflected, and an evanescent wave is created in the adjacent medium (n_2), which must have a lower index of refraction than n_1. The penetration depth of the evanescent wave varies with the angle of incidence, the wavelength of light, and the indices of refraction of the two media (31). The penetration depth into the sample medium, *dSPR*, is

$$d_{SPR} = I\left[\frac{\lambda}{4\pi n_c}\sqrt{(\varepsilon_m + n_c^2)}\right]$$

where ε_m is the dielectric constant of gold. The penetration depth at SPR varies from ~100 nm up to 5 µm as the wavelength increases from 600 nm to 4 µm as predicted theoretically (32-34) and also verified experimentally (35).

The TIR geometry provides excellent background rejection for interfacial measurements. The ratio of fluorescence intensities from sequential acquisitions with fixed-angle TIRFM and wide-field microscopy (36; 37) or from two-angle TIRFM (38) can give good estimates of axial distances, while more depth-resolved information is obtainable with prism or objective-based variable-angle TIRFM (22; 39-42) where a stack of multi-angle images contains the integrated fluorescence intensity over various thicknesses of the sample.

There are basically two types of optical configurations for TIRF/TIRS microscopy: objective-based TIRF/TIRS in which a high numerical aperture (N.A.) objective is used for both TIR excitation and emission, and prism-based TIRF/TIRS, in which a prism is used to direct incident light to the interface and an objective is used only to collect emission signals. (Figure 1.3 and 1.4)

Figure 1.3 shows the optical configuration of objective-based TIRF/TIRS microscopy. A beam expander is placed after the laser to expand the convergence/divergence angle of the laser light beam at the back focal plane of the objective and to enlarge the illumination area at the sample plane. The focusing lens is used to change the incident angle of laser beam and realize TIR illumination. Objective-based TIRF/TIRS microscopy suffers from the impure illumination resulting from excitation scattering light inside the objective and impure emission collection resulting from luminescence signals from the objective internal components (31).

Figure 1.4 shows the schematic light path of prism-based TIRF/TIRS microscopy. A pair of mirrors (Mirror 1 and Mirror 2) is used to change the incident angle of laser beam in TIR illumination. A focusing lens is used in the light path to control illumination area at the sample plane which should be smaller than the field of view. Prism-based TIRF/TIRS microscopy provides cleaner evanescence field illumination and wider range of incident angle than objective-based TIRF/TIRS microscopy (31).

1.5 Introduction to Raman Spectroscopy

Raman spectroscopy is a commonly used spectroscopic technique to investigate the vibrational and rotational modes of a system (43; 44). As shown in Figure 1.5, Raman scattering is an inelastic scattering process, the molecule is photo-excited into a virtual state and then emits photons to a vibrational state higher (Stokes) or lower (anti-Stokes) than the original state. The quantum yield of Raman scattering is on the order of 10^{-6}. In resonance Raman spectroscopy (Figure 1.5), the molecule is photo-excited into an excited state instead of a virtual state and lead to much higher intensity of the scattering.

Raman spectroscopy has been considered to be a powerful technique for structural analysis (45; 46). By using lasers of different frequencies from the near-ultraviolet to the near-infrared red in the Raman module, different samples can be excited under their optimum excitation conditions. By choosing lasers with appropriate frequencies, certain electronic transitions can be excited and resonance Raman studies of certain components of a sample or parts of a molecule can be realized (7; 47). Raman spectroscopy can provide rich information about chemical structures without special sample preparation requirements, making it capable for in situ experiments (48; 49). Also, since the measurements can be operated in an open and ambient environment, different conditions such as temperature, pH and electronic voltages can be applied to the sample with various designs of sample holder. By changing the immersion objectives, sampling in different environments like water or air is made possible.

The spatial and temporal resolution of Raman scattering measurements are determined by the excitation laser spot size and pulse length. In confocal Raman technique, Raman signals from femtoliter volumes (~1 μm^3) can be measured, which realizes spatially resolved measurements in chromosomes and cells (47; 50). Moreover, by using different data analysis techniques based on multivariate analysis, more information about the sample chemical structure and chemical composition of complex systems can be obtained (51).

1.6 Introduction to Photoluminescence Spectroscopy

Photoluminescence (PL) spectroscopy has been widely recognized as an useful technique for the optical and electronic characterization of materials such as quantum dots (52), crystalline semiconductors (53) and carbon nanotube bundles (54) and dynamic processes of materials (53). PL spectroscopy is widely applied to study different defects (55; 56), the photocatalysis of semiconductors and quantum effects in nanocrystals (52; 57), complex molecules and their chemical environments and locations in biochemistry (58). Moreover, PL spectroscopy as a nondestructive technique is applied to in situ and operando measurements in electrochemical reactions revealing defect formation (59-62).

In PL spectroscopy, sample is firstly photo-excited with electrons promoted into excited states and then excess energy releases in the form of light emission when excited electrons return to the ground state. The energy of the emission light is related to the energy difference between the two electron states in the transition. Therefore, PL spectroscopy can be used to measure the direct band gap of semiconductors (53).

1.7 Introduction to Spectro-microscopic Imaging System

Optical microscopy imaging has been playing an increasingly important role in the investigations of nano- and bio-materials and fundamental chemical processes (e.g., diffusion, adsorption and reaction) at the molecular and nanoscale level. However, its wide chemical applications have been hindered by the absence of definitive chemical information of the sample in light microscopy images. Spectroscopic techniques (Raman, Infrared, etc.) are often required as companion tools to gain structural fingerprints of the sample.

Various types of spectroscopic measurements (such as Raman, infrared, absorption, and fluorescence) can add valuable chemical and/or structural information as a new dimension of information to samples' optical microscopy images when integrated with optical microscopes. Optical spectroscopic measurements provide rich molecular fingerprint information of samples and has shown capability in visualizing the molecular composition of subcellular structures noninvasively (63-65). Through the combination of microscopic and spectroscopic techniques, physical and chemical processes can also be correlated and discerned.

1.7.1 Integration of Optical Microscopy with Raman Spectroscopy

Raman spectroscopy is a non-invasive and label-free spectroscopic technique that is highly sensitive to chemical composition and structural information. Raman spectroscopy has been successfully integrated with different optical microscopy techniques such as light-sheet microscopy (66), confocal microscopy (67-69), scattering microscopy (70; 71), fluorescence microscopy (72), mid-infrared photothermal microscopy (73) and multi-photon imaging system (74). The integration helps to characterize chemical distribution within samples (67; 75), confirm reversible chemical reactions detected by other imaging modality (71), provide real-time information of chemical bonds (70), decrease acquisition time and increase imaging specificity (68), avoid interference between encoding and label signal and increase accuracy in multiplexed biological detection (72), and elucidate various tissues with their molecular details with no lengthy procedures such as fixation, sectioning and staining when study pathological transformations (74).

1.7.2 Integration of Optical Microscopy with Infrared Spectroscopy

Similar to Raman spectroscopy, Infrared (IR) spectroscopy is another nondestructive spectroscopic technique that provides fingerprint spectra of samples and therefore can characterize sample with rich chemical information without staining and labeling. Different from Raman spectroscopy which arise from the change of polarizability of the molecular vibration (76), IR spectroscopy is due to a net change in the dipole moment of a molecular vibration (73) and provides comprehensive characterization for samples with Raman spectroscopy.

Improvements in spatial resolution and detection sensitivity have been made by replacing the conventional thermal emission sources used in FTIR spectro-microscope with a synchrotron IR source (77; 78), which is 100-1000 times brighter than conventional thermal emission sources (79). The high signal to noise ratio resulting from the enhanced source brightness not only improves the spatial resolution but also benefits its applications on studies of very weak IR signals from isotopic shifts (80) and makes in situ experiments in solution possible. On the other hand, to improve the spatial resolution, the integration of atomic force microscope with an infrared laser source (AFM-IR) (81), which utilizes an AFM tip to sense and map IR-induced thermal expansion, is invented and achieved a spatial resolution of 20 nm (82). Another IR technique developed to overcome the poor spatial resolution is infrared photothermal imaging (63-65; 83), in which the resolution is determined by the diffraction limit of the visible probe wavelength. Cheng et al. developed a system that combines mid-infrared photothermal microscopy with confocal Raman spectroscopy realizing fast infrared photothermal imaging of living cells with submicrometer resolution and full-spectrum Raman analysis (73).

Whelan and Bell integrated synchrotron Fourier transform infrared (S-FTIR) spectroscopy with direct stochastic optical reconstruction microscopy (dSTORM) to study biochemical changes induced by different cell fixation methods at single cell level (84). dSTORM imaging was applied to characterize cell structures and distribution of targeted biomolecules. IR spectroscopy, limited by the spatial resolution of ~5 µm, was used to characterize the biochemical changes of an entire cell. dSTORM images and corresponding IR spectra were taken before and after chemical fixation of the cell preparation protocol of the dSTORM using different fixatives. By interpreting IR spectra, fixation effects of different fixatives on the composition of lipid bilayer and overall DNA secondary structure were investigated and correlated to the changes of dSTORM images.

1.7.3 Integration of Optical Microscopy with Transient Absorption Spectroscopy

Transient absorption (TA) spectroscopy has been widely applied to provide valuable insights into the dynamics of excited-state molecules (85). TA microscopy, integrating TA spectroscopy with scanning microscopy (86) (both near-field (87; 88) and far-field super-resolution techniques (89-96)), provides both time-resolved and space-resolved measurements of TA.

By combining the spatial information with TA spectroscopy, signals from heterogenous samples can be located spatially and temporally. In material science, characterization of both temporal and spatial behaviors of the carriers is very helpful in understanding the relationship between excited state properties and material morphological features such as interfaces (97-103). It also benefits heterogeneity studies of nano-objects (104-111) and interaction studies between materials and substrates (104; 105; 112-114). Recent advances have been made to improve the performance of TA microscopy in detection sensitivity (115-117), spatial resolution (86-96) and imaging speed (86; 118).

1.7.4 Integration of Optical Microscopy with Fluorescence Spectroscopy

Super resolution microscopy, which overcomes diffraction limit of light and provides spatial resolution of ~10 nm however typically can only offer monochrome images, has been widely integrated with fluorescence emission spectroscopy to realize multicolor or ‘true color’ imaging.

In earlier studies, fluorescence emission spectroscopic information is reflected as the ratio of photon numbers which are detected by two split detection channels covering two different wavelength regions. The ratio of photon numbers is then used to distinguish signals from different markers and realize simultaneous multicolor fluorescence imaging (119-121). During the experiments, fluorescence signal from switch-on molecules was split into two light paths according to wavelength (by inserting different emission filters into light collection path) and detected by the different areas on the electron-multiplying CCD (EMCCD) detector. The 2D frequency histogram of the photon number ratio of molecules from different detection channels are used to distinguish molecules with different emission spectra. In recent studies, the fluorescence emission spectroscopic information is obtained by dispersing the fluorescence signal through a prism before it is detected by one of the detection channels (122-125). With recent studies, high-throughput single-molecule spectroscopy combined with super-resolution microscopy has achieved recording spectra of ~102 molecules per few-millisecond and 3 D characterization both spectrally and spatially (122). There are also studies replacing the prism with a grating and realizing simultaneous spatial and spectral characterization (126; 127). The optical microscopy integrated with fluorescence spectroscopy has been utilized to investigate physicochemical changes of local environments (125; 127) and reaction pathways of single molecules (128).

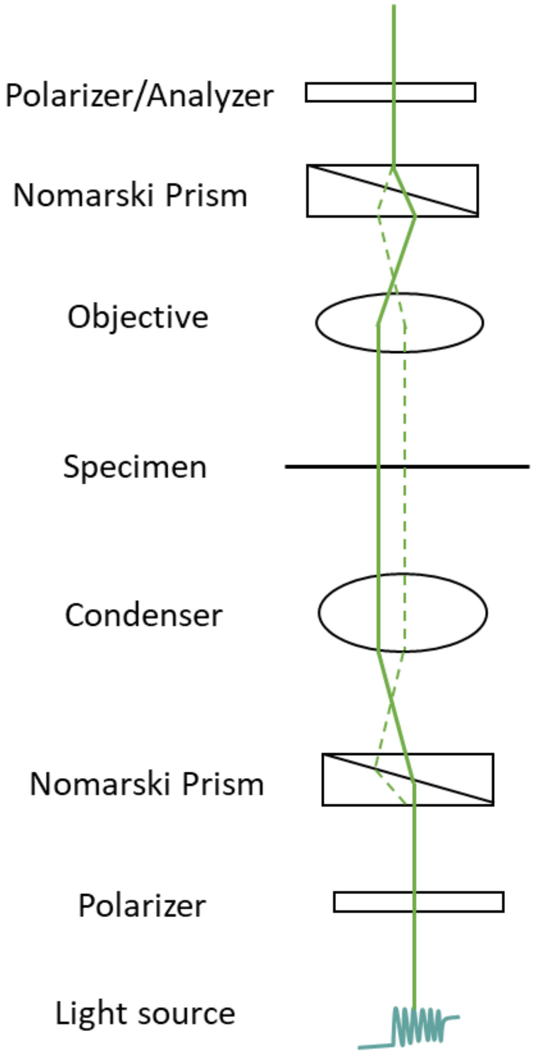

Figure 1.1 Schematic light path of transmitted DIC microscope.

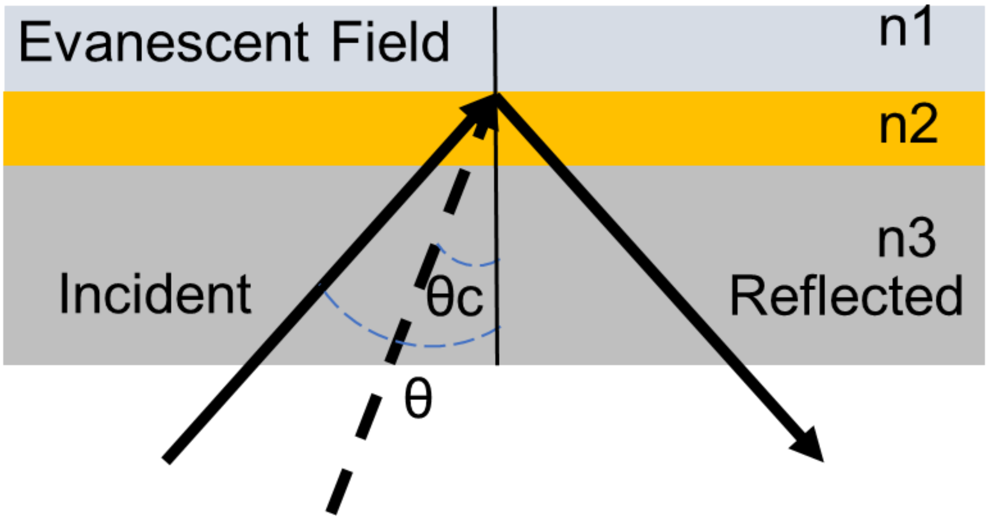

Figure 1.2. Total internal reflection illumination light path.

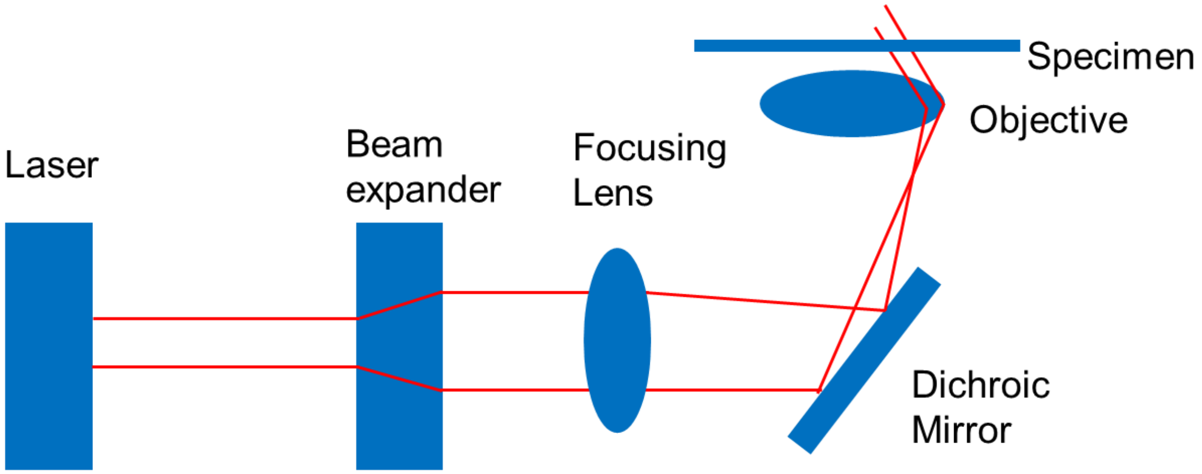

Figure 1.3. Schematic light path of objective-based TIRF/TIRS microscopy.

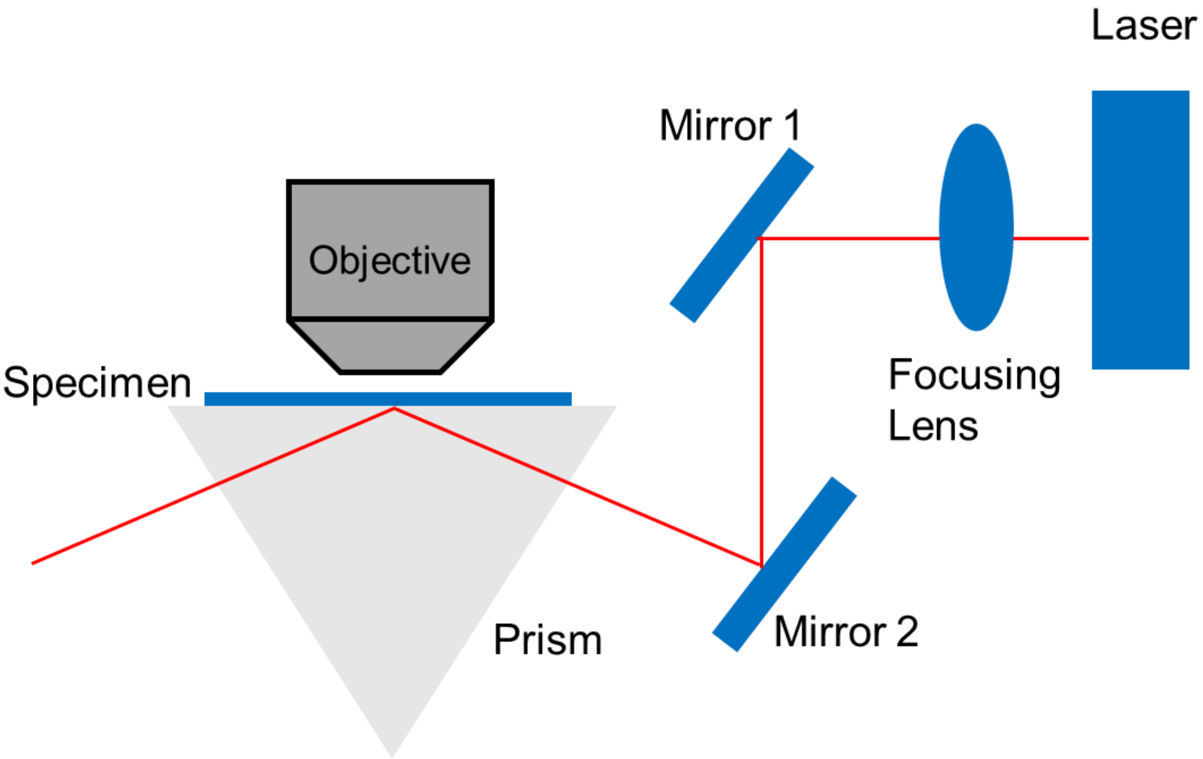

Figure 1.4. Schematic light path of prism-type TIRF/TIRS.

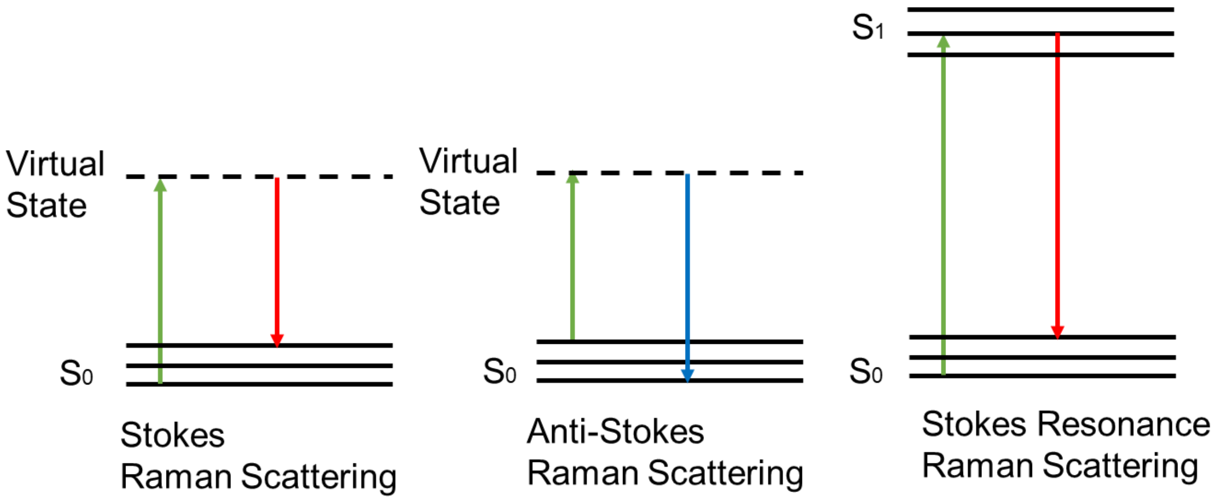

Figure 1.5. Jablonski energy diagram of stokes Raman scattering, anti-stokes Raman scattering and resonance Raman scattering processes.

2 DEVELOPMENT OF MULTISCALE SPECTRO-MICROSCOPIC IMAGING SYSTEM

2.1 Introduction

To this date, it is still challenging to perform in situ microscopic and spectroscopic measurements of the exact same sample (or the exact same region of a sample), especially for samples undergoing continuous transformations (129-135). The existing multi-modality spectro-microscopic systems employ microscopy modes mostly for relatively simple purposes, such as sample positioning and fluorescence image acquisition as discussed in Chapter 1. The more advanced features, including single molecule sensitivity, sub-diffraction-limited spatial resolution, and fast (millisecond range) temporal resolution, that have become the trademarks of microscopy development in the past decade, have rarely been combined with spectroscopic measurements. In the meanwhile, a system that can characterize both physical and chemical properties of samples in situ is necessary for a fuller understanding of physicochemical characteristics (48; 136-143).

On the other hand, new challenges and opportunities evolve at the intermediate scales (length scales from ~10 nm to 10 μm) between nano- and traditional macro-scale (bulk) materials. A fundamental challenge is to observe and characterize the inherent imperfection and statistical variation in mesoscale materials. It has been realized that many functional materials begin to manifest their functional behaviors starting at mesoscale, where nanoscale building blocks are assembled into more complex functional architectures for more diverse interactions with the environment and greater functionality (144-146). Significant progresses have been made on our understanding of nanoscale structures in the past decades; however, mesoscale structures, which are intrinsically dynamic and metastable, remain relatively unexplored. Mesoscale structures have a relatively lower energy cost to change their configurations or introduce boundaries and generate more distinct phases, resulting from more densely spaced energy levels comparing to nanoscale structures (144). The lack of knowledge in mesoscale has restrained our ability to predict and optimize the performance of functional materials and often limited their application to trial and error. In situ multi-modality characterization systems, capable of performing and correlating various physical and chemical measurements of the same sample area undergoing continuous transformations under environmental stimuli, are much needed to monitor and understand the evolution of materials from molecular level to mesoscale.

Optical microscopy imaging is inherently suited for studying mesoscale structures and dynamics for its matching resolution range (tens to hundreds of nanometers). It is much less invasive compared to electron microscopy (EM), where high-energy electron beams could easily damage the sample, especially fragile crystalline structures in organic films (147). In most cases, special sample preparation is not needed for optical microscopy, therefore allowing high-throughput in situ characterization and screening. High throughput is an advantage of wide-field optical microscopy imaging techniques over other high resolution and high contrast techniques, such as EM, scanning probe microscopy, atomic force microscopy (AFM) and near-field scanning optical microscopy. Near-field scanning optical microscopy has low incident light intensity hindering excitation of weak fluorescent molecules and is not suitable for imaging soft materials because of the high spring constants of the optical fibers (48). When a transformation is subtle or spectroscopic measurements of fine sample structures are needed, high resolution and high contrast microscopic techniques that can quickly locate and observe the subtle structures are required while spectroscopic measurements are taken. Therefore, the high resolution and high contrast images of physical morphology changes of the sample can be correlated with the spectroscopic changes, which indicates the chemical property changes of the sample.

Optical microscopic imaging techniques are also advantageous because they are less invasive; thus, the sample integrity is usually maintained throughout the sampling process enabling the study of dynamic progressions over an extended timeframe. Usually for samples observed under optical microscopy imaging techniques, no special sample preparations are needed; therefore, samples can be observed and studied under their working conditions.

On the application side, samples like polymeric blend thin films used in bulk heterojunction (BHJ) organic photovoltaics (OPVs) and organic field transistors are deposited on silicon surfaces which is nontransparent and highly reflective. Therefore, techniques that can test samples on reflected surface is necessary to study the properties of those materials since material properties may change during its transferring to a regular microscope glass slide.

Therefore, the multi-modality multiscale imaging system which combines far-field optical microscopy imaging (DIC microscopy, crossed-polarize light microscopy, TIRF microscopy and TIRS microscopy) with confocal spectroscopy (Raman and photoluminescence spectroscopy) is developed to provide chemical (by Raman and photoluminescence spectroscopy) and morphological (by DIC microscopy, cross-polarized light microscopy, TIRF microscopy and TIRS microscopy) information of samples in situ from molecular level to mesoscale. Integrated with the home-built post treatment (thermal annealing and solvent annealing) sample stages, the system provides a platform to study the relevant multiscale structures and their response to environmental stimuli in situ. This chapter provides the instrumentation details of each imaging module in the multi-modality multiscale spectro-microscopy imaging system.

2.2 Experimental Section

The optical microscopy imaging module was equipped with a Dhyana 400BSI sCMOS camera (Tucsen Photonics, Fuzhou, China) and a Zeiss EC Epiplan-Apochromat 100X objective

(N.A. 0.95) and Zeiss Apo Plan 100X oil immersion objective (N.A. 1.40). The confocal spectroscopy module was equipped with an IsoPlane 160 spectrometer and a PIXIS 100B camera (Teledyne Princeton Instruments, Acton, MA), and a 488nm laser as the excitation source for both Raman and photoluminescence spectroscopy measurements. Filters and the dichroic mirror were purchased from Semrock (Rochester, NY). All other optics and optomechanical components were purchased from Thorlabs (Newton, NJ).

2.3 Results and Discussion

The multi-modality multiscale spectro-microscopic imaging system consists of differential interference contrast (DIC) microscopy module, cross-polarized light microscopy module, total internal reflection fluorescence/scattering (TIRF/TIRS) microscopy module, confocal spectroscopy (Raman and photoluminescence) module (Figure 2.1A) and home-built post treatment (thermal annealing and solvent annealing) sample stages module (Figure 2.1 B and 2.1 C).

2.3.1 Reflected Differential Interference Contrast (DIC) Microscopy Module

Different from the transmitted light DIC setup (Figure 1.1) which adopts a two-prism transmitted-light configuration, the reflected light DIC setup (Figure 2.2) only adopts one Nomarski prism. The objective is used both as a condenser to collimate incident light onto the sample and a detection optics to collect scattering signals from the sample. The reflected DIC microscope was optimized for the detection of individual nanoscale building blocks and intermediate features of mesoscale materials on reflective surfaces such as silicon wafers, gold coated substrates, etc. The advantages of reflected DIC microscopy on characterization of samples on reflective surfaces over other conventional methods such as EM and scanning probe microscopy include noninvasive and nondestructive rapid characterization, relatively simple sample preparation, dynamic measurements in real time, and relatively less expensive.

It is worthwhile to note that reflected DIC configuration was demonstrated as early as 1979 by Lessor et. al. and applied towards surface topography studies (148). Traditionally, reflected DIC has been used to both qualitatively and quantitatively report surface roughness while studying polishing techniques, and it has also found much use in visualizing details and defects in semiconductor chips made on silicon wafers. However, all of the previously developed reflected DIC microscopes are limited to standalone systems with relatively low magnification and low resolution due to design and instrumental challenges. An oil-immersion objective with a high numerical aperture and high magnification is necessary to achieve high resolution and high sensitivity imaging in reflected DIC. Yet, this requires sophisticated instrumentation due to the limited space and short working distance.

Figure 2.1A shows the key components of the reflected light DIC microscope. Light emitted from a light-emitting diode (LED) light source was collimated by a group of lenses, passed through a linear polarizer, and was reflected by a beamsplitter plate placed at 45° angle to the incident light beam. Then, the light was focused onto the Nomarski prism which was positioned at the rear focal plane of the objective. The Nomarski prism can be translated laterally across the optical path to introduce bias retardation to achieve best image contrast for different samples. The objective then collimated sheared orthogonally polarized wavefronts onto the sample. Then, light scattered from the sample was collected by the same objective and focused onto the interference plane of the Nomarski prism where they were recombined to eliminate the shear. After passing through the Nomarski prism, the same beamsplitter and a second linear polarizer (also called analyzer), the light was focused on the CCD camera by a 200 mm tube lens.

2.3.2 Reflected Cross-polarized Light Microscopy Module

The configuration of the reflected cross-polarized light microscope is similar to the reflected light DIC microscope, except for the Nomarski prism (Figure 2.3). These two modes can be easily switched by changing the position of the Nomarski prism in the light path. Instead of being separated by the birefringent Nomarski prism into two orthogonally polarized light wavefronts, the linearly polarized incident light in cross-polarized light microscopy is separated by the anisotropic sample itself along its longitudinal axis and transverse axis. The light beams passed through the sample along different optical axes of the sample and experienced different refractive indexes resulting in different phase retardation. Then the two orthogonally polarized light beams projected onto the transmission axis of a second linear polarizer and interfered with each other. Finally, the interference pattern of the sample with orientation information was detected by the camera.

2.3.3 Total Internal Reflection Microscopy Module

The prism-type TIRF/TIRS microscopy module with 532 nm and 488 nm excitation lasers is integrated into the multi-modality multiscale spectro-microscopic imaging system (Figure 2.1A). The light path of the signal collection in the reflected light DIC microscope module was shared with the TIRF/TIRS microscopy module. A home-built sample stage (Figure 2.1D) was used to couple prism-type TIRM/TIRS into the imaging system. Excitation light was guided by the prism towards the solid-liquid interface at an incident angle larger than the critical angle and generated an evanescent field (Figure 2.4), which excited samples near the interface. Fluorescence or scattering signals from the sample were collected by the objective and delivered to the camera. This design enabled us to directly mount sample slides on top of the prism and allowed the simultaneous acquisition of TIRF/TIRS microscopy images and Raman spectra. Special substrate such as quartz slides coated with a thin layer of gold film (149; 150) can be used to support the sample. The gold film was at the interface of a glass substrate and the sample (e.g., cells or aqueous medium). The incident light was converted to surface plasmon resonance (SPR) at the electronically conducting gold film. The plasmon then created an evanescent wave field that extended into the medium on either side of the gold film. The gold film also served as the reflection mirror for reflected DIC imaging.

2.3.4 Confocal Spectroscopy Module

A confocal spectroscopy system was built into the multi-modality multiscale spectro-microscopy imaging system to allow in situ acquisition of both spectroscopic and microscopic measurements. The coupling of the Raman spectroscopy and reflected DIC microscopy can be used to correlate the surface enhancement and inter-particle distance information. The main design challenge was to enable the coexistence of two very different sets of optics for reflected DIC microscopy and Raman spectroscopy meanwhile achieved the best image and spectra quality, respectively.

In this instrument, the inherent sensitivity of Raman/Photoluminescence spectroscopy on the chemical properties of the sample and the inherent sensitivity of Reflected DIC microscopy on the topographical geometrical profile of the sample were combined to provide an accurate, high throughput, non-destructive, label-free and in situ available analytical method under ambient conditions.

Most of the reflected DIC optics were shared with the built-in confocal spectroscopy module. (Figure 2.1A) The excitation laser was reflected by a flip mirror and a 45° dichroic mirror onto the back focal plane of the objective. Then the excitation laser was focused by the objective into a diffraction limited spot on the sample. The scattering or emission signal from the sample was collected by the objective and focused onto the slit of a spectrometer. (Figure 2.5) Therefore, Raman/PL spectra of the same area as in the optical image can be taken by using the Raman/PL spectroscopy module. The laser spot size used in Raman/PL spectroscopy module was about 0.5μm.

2.3.5 Post Treatment Sample Stages Module

The thermal stage (Figure 2.1B) was made of a thermoelectric (Peltier) cooling module from TE Technology, which was used for heating by reversing the electric current flow. The thermoelectric module was controlled by a temperature controller (TC-720, TE Technology).

The solvent annealing stage (Figure 2.1C) can be used to provide different solvent environment for samples during solvent annealing experiments.

2.4 Conclusions

A multi-modality spectro-microscopy imaging system capable of in situ optical characterization with sub-diffraction-limited spatial resolution and fast temporal resolution has been developed. The in situ imaging capability of this new system makes it a valuable characterization technique complementary to other conventional methods, such as electron microscopy and scanning probe microscopy. By integrating spectroscopy modules into the imaging system, both physical and chemical information of the same sample area can be correlated. The multi-modality spectro-microscopy imaging system is also a high throughput optical instrument system operating under ambient or controlled conditions using visible light sources. The system will stimulate new scientific explorations that are previously unattainable by providing scientists with a new capability in acquiring and correlating a broad range of information of their samples dynamically with sub-micron spatial resolution.

2.5 Figures

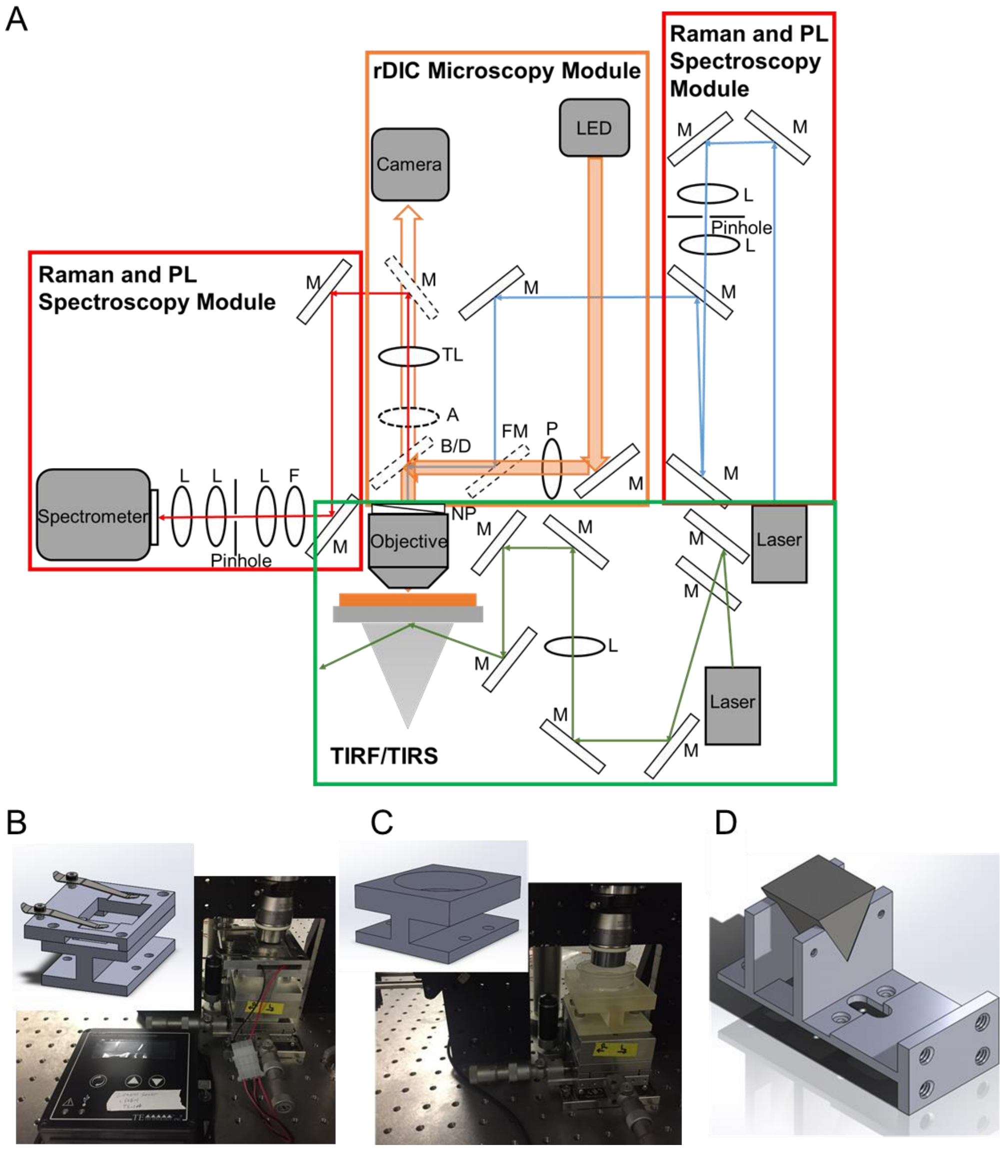

Figure 2.1 (A)Instrumentation scheme; Components with dashed outline are removeable among different modules; M:Mirror; L:Lens; F:Filter; B/D: Beamsplitter or Dichoric Mirror; P:Polarizer; A:Analyzer; FM: Flip Mirror; TL: Tube lens; NP: Nomarski prism. (B)Thermal annealing stage and its temperature controller. (C)Solvent annealing stage. (D)Prism-type TIRF/TIRS sample stage.

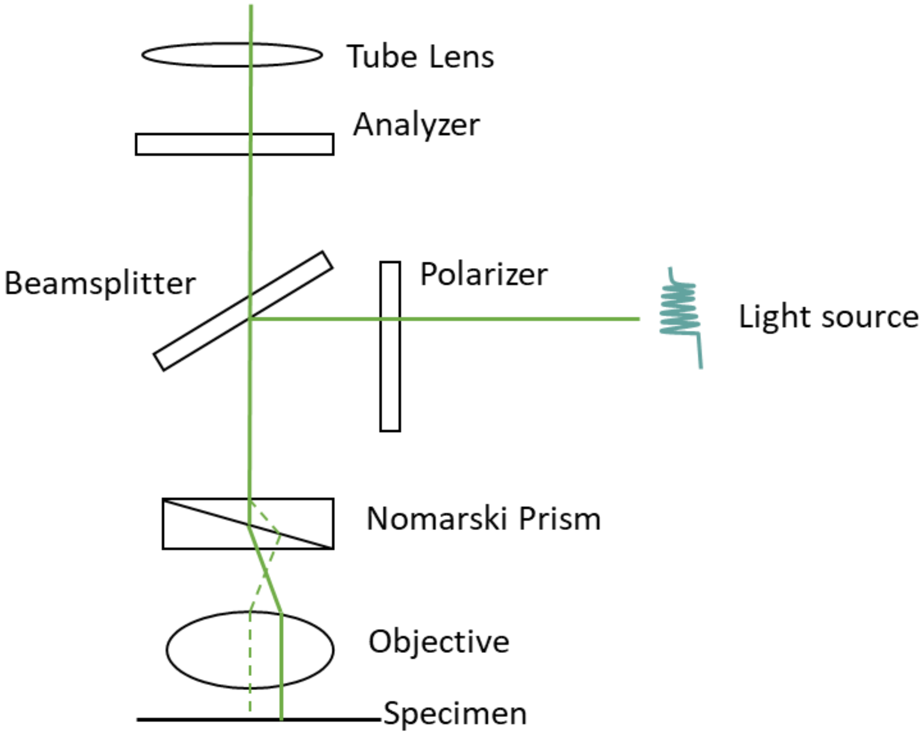

Figure 2.2. Schematic light path of reflected DIC microscope.

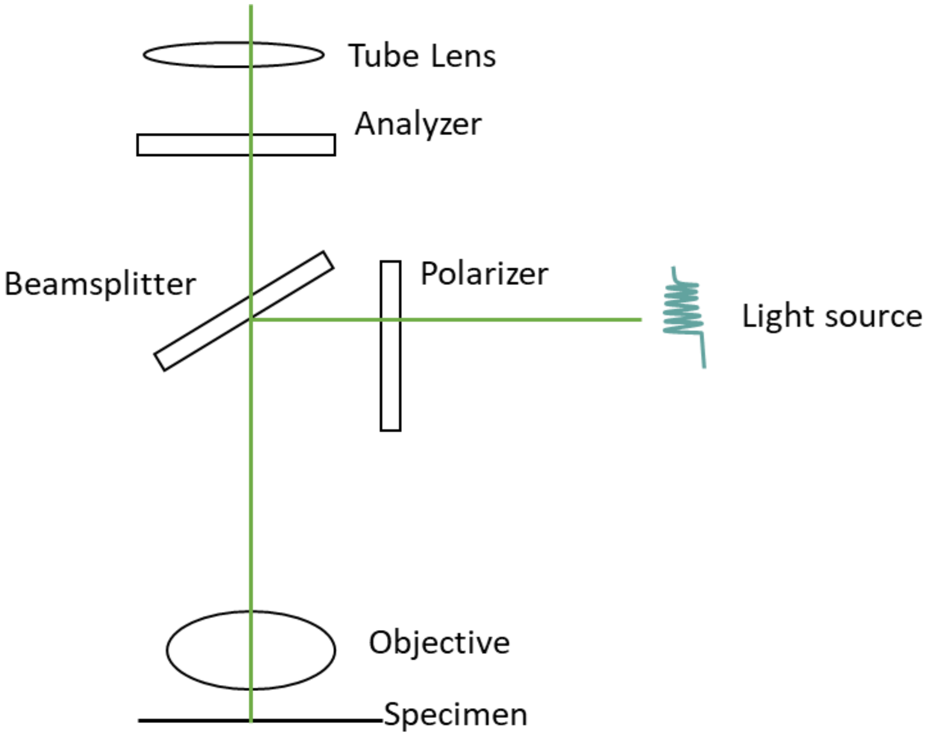

Figure 2.3. Schematic light path of reflected cross-polarized light microscope.

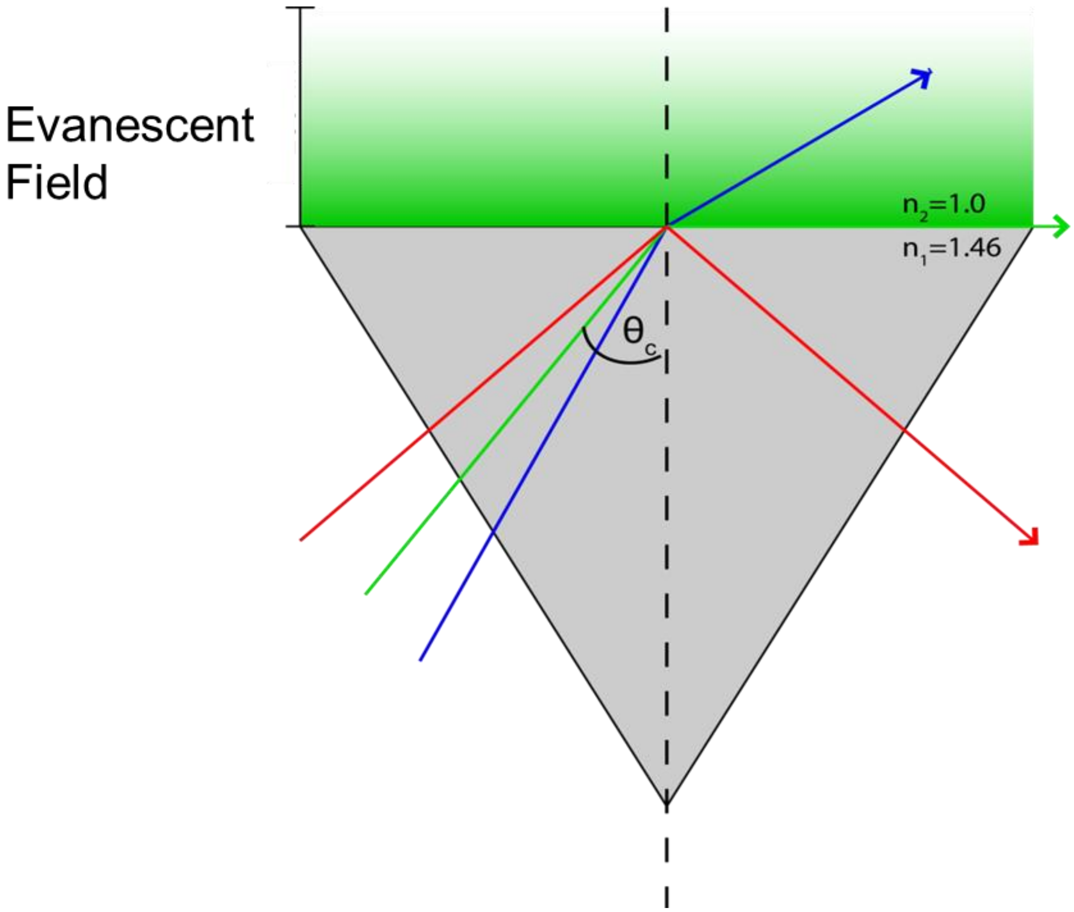

Figure 2.4. Schematic light path of prism-type TIRF/TIRS.

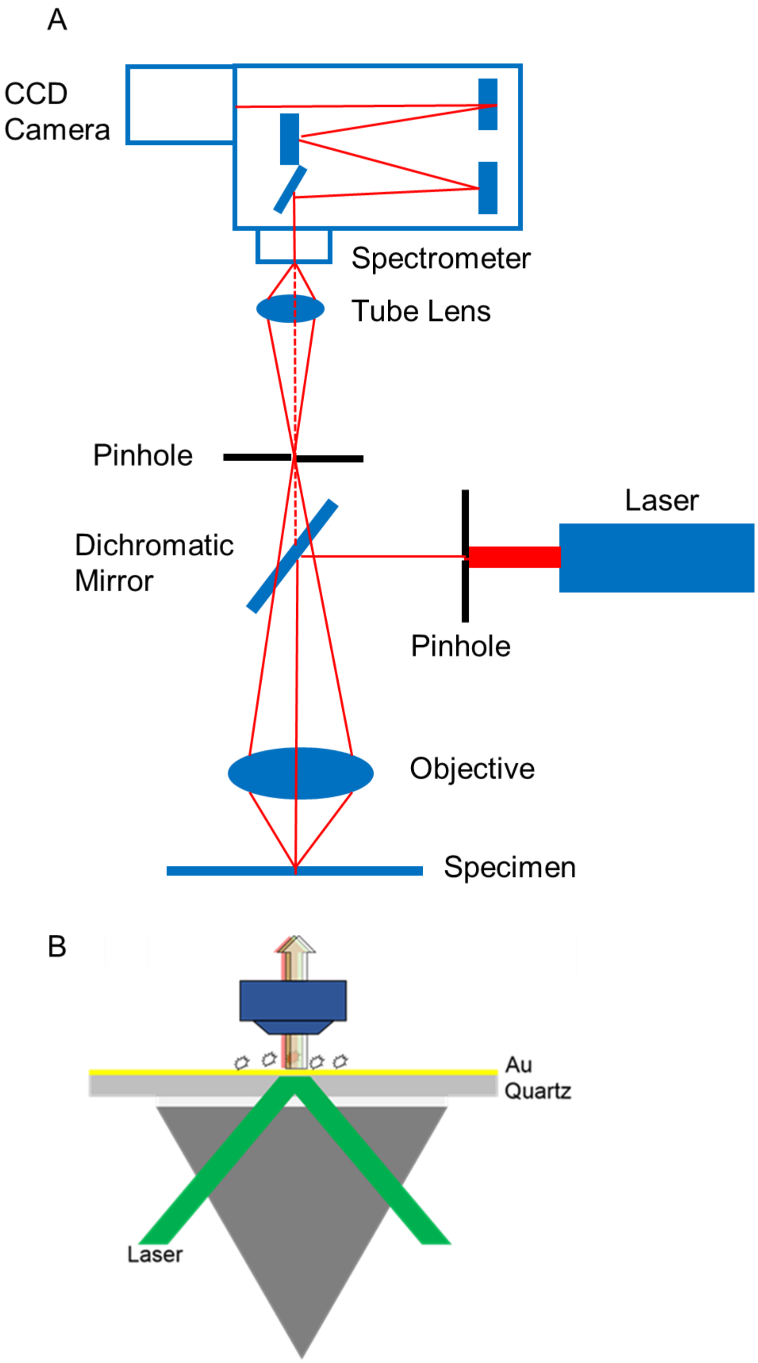

Figure 2.5. (A)Schematic light path of the confocal spectroscopy module. (B) Schematic light path of total internal reflection scattering light path.

3 IN SITU CHARACTERIZATION OF PHOTOACTIVE LAYERS IN BULK HETEROJUNCTION SOLAR CELL UNDER THERMAL STRESS BY THE MULTI-MODALITY MULTISCALE SPECTRO-MICROSCOPY IMAGING SYSTEM

3.1 Introduction

Structures of organic semiconducting materials in different length scales, ranging from the π-π stackings at the molecular level to charge transport pathways at the meso-, micro- and macroscopic scales, can profoundly affect the properties and features of the resulting architectures and their consequent performance in organic optoelectronic devices, including organic thin-film field-effect transistors (FETs), organic light-emitting diodes (LEDs), and organic photovoltaics cells (151-154). However, it is challenging to obtain information spanning such a wide length scale correlatively in situ using conventional characterization methods, (147; 154-156) which restrains our understanding of the inherent hierarchical structures of organic semiconductors and their structure-property relationship. Departing from conventional characterization methods of material science mostly focused on structures from one length scale, we apply an in situ multi-modality characterization system onto the study material structural information from the molecular level to the mesoscale.

Photoactive layers in bulk heterojunction (BHJ) solar cells as a standout example with imperative need of in situ characterization in mesoscale, are composed of polymer semiconductors as hole-conducting materials and acceptor molecules, e.g., fullerene derivatives, as electron-conducting material. They are intrinsically metastable and demonstrate a range of physical and chemical properties across different regions within a sample. Dramatically different optoelectronic properties may result from small changes occurred during sample preparation or post deposition processes (151). Nanoscale domains in these polymer films have been studied extensively by electron microscopy (EM) and atomic force microscopy (AFM), which benefits from their superior spatial resolution; (147; 154-156) however, the mesoscale pattern formation, which reflects the collective behavior of nanoscale domains, is rarely studied. It is reported that features generated in different length scales, from molecular level to micrometer scale will all affect optoelectronic properties of polymer active layers in BHJ solar cell and device performance (151; 154), which makes it necessary to characterize the order and arrangement of materials of the same sample area under in situ transformation at multiple length scales (157). Furthermore, techniques like EM, AFM and X-ray diffraction can be elaborate and time-consuming and affecting the working conditions when they are applied routinely on the characterization and test of active blend films that are being used in devices (158).

In material science area, grazing incidence X-ray scattering (GIXS) has been demonstrated as an useful tool in the characterization of the morphology of polymer-fullerene BHJ blends thin film for qualitative purpose. However, GIXS is not able to provide the morphology information with spatially properties (159-161). GIXS also has relatively long collection times ranging from 120s to 180 s depending on the scattering properties of the sample. In contrast, our multi-modality imaging system can provide spatial information in ms and can be a good complementary characterization technique to other bulk characterization techniques.

Differential scanning calorimetry (DSC) is another technique that is commonly used to characterize the thermal properties of photoactive layers used in BHJ solar cells and the melting points of the components and other first order phase transitions can be revealed by DSC (161). However, DSC measures the thermal properties of the bulk material, but the phase behavior may be significantly different for thin film samples of the same material.

Atomic force microscopy (AFM), transmission electron microscopy (TEM) and scanning electron microscopy (SEM) are also most commonly used characterization methods in material area with a high resolution to several nm, however, the observation field of view is small compared to the size of the photoactive layers used in real solar cells or organic field transistors. Long-time scanning and special sample preparation are needed for those techniques, which makes in situ characterization difficult. The wide-field optical microscopy in the multi-modality spectro-microscopy imaging system has a much larger field of view and therefore can provide quick screening, high throughput characterization in situ. On the other hand, for BHJ blend, for example, poly(3-hexylthiophene) (P3HT)/ [6,6]-phenyl C61 butyric acid methyl ester (PCBM), both components are carbon materials and electron density are similar, which makes it difficult to differentiate different chemical domains by using TEM and SEM, which are characterization techniques relying on the electron density of samples.

Absorption is also a widely used technique to characterize the polymeric thin films. For conjugated polymers, absorption spectra of polymer films with higher molecular order (or high crystallinity) have a shoulder peak comparing to polymer films with lower molecular order (or low crystallinity). For example, in regioregular P3HT films, there is a distinct shoulder peak on the long-wavelength side of the absorption maximum peak resulting from the closer interchain packing. However, in the blend thin film of 1:1 P3HT: PCBM, the spectra overlap severely between unaggregated P3HT transitions and PCBM, which makes accurate characterization of the blend thin film sample of P3HT and PCBM difficult. In the meanwhile, the different lineshapes (Franck-Condon factors) of aggregated and unaggregated components also contributes to the inherent difficulty of characterizing the relative contributions of regioregular and regiorandom components to the overall absorption lineshape (162; 163). Fortunately, more reliable characterization for regioregular and regiorandom components in conjugated polymeric thin films can be obtained from Raman spectroscopy, which also provides the basis for spatially mapping structural feature of the conjugated polymeric thin films on the submicrometer size scale.

Post deposition treatments, such as thermal annealing, are commonly used to improve the power conversion efficiency (PCE) of the photovoltaic devices. Many research groups reported that P3HT/PCBM optoelectronic performance is greatly enhanced after 10-30 mins thermal annealing after deposition (164). However, in many cases, it is not fully clear how to characterize the microstructure changes in situ during a transformation and how to control the microstructures to increase the PCE (165). The lack of understanding results in the limits of the optimization of electron-donating and electron–accepting materials in solar cells to trial and error (166). Therefore, it is critically important to develop techniques to quickly characterize microstructures in situ both spatially and spectrally.

The spectroscopic properties of conjugated polymers are related to the conformation and aggregation of the polymer chains (167-169). For example, P3HT has coil-like conformation in dilute THF solution (169), which results from shorter conjugation length caused by distortion and the C-C bond bending between adjacent thiophene rings (170). However, in the film samples, the conjugated polymers have a planar conformation resulting from the efficient π-π stacking between adjacent polymer chains (171). Therefore, polymer chains become more extended and rigid, have limited flexibility and rotations, and thus have an increased conjugation length in film samples (170). The optoelectronic properties of the blend thin films of conjugated polymer blends and PCBM are closely related to the polymer chain morphology and polymer chain interactions (170). Different chain conformations and packing or aggregation types lead to complex heterogeneous materials and performance, for example as shown in Figure 3.1, the π-π stacking is the second fast charge transport direction in the edge-on packing motif of conjugated polymers (170; 172; 173). Because of the high complexity and heterogeneity of conjugated polymers, it is difficult to obtain a detailed understanding of optoelectronic processes occurring in BHJ polymeric blend films from one type of spectroscopic technique and one length scale.

In this chapter, the multi-modality spectro-microscopic imaging system is applied on in situ characterization of photoactive layers in bulk heterojunction (BHJ) solar cells under thermal stress from multiscale. With the multi-modality spectro-microscopic imaging system, knowledge, and associated strategies for controlling the equilibrium microstructure of BHJ organic solar cell have been developed. Utilizing the home-built thermal annealing microscope stage, the multi-modality spectro-microscopic imaging system has been employed for an in situ multiscale correlative study of the thermotropic evolution of a photoactive layer of 1:1 P3HT: PCBM. The multiscale thermotropic evolution is characterized by three phase transition stages with their critical temperatures identified. At last, the impact of different temperature dropping processes on the photoactive layers are also studied using the spectro-microscopic imaging system.

3.2 Sample Preparation and Experimental Measurements

3.2.1 Film Preparation

Regioregular P3HT (RR-P3HT) was purchased from Rieke Metals. The molecular weight (Mw) was 50-70 kg/mol on average, and regioregularity was 91%-94%. Regiorandom P3HT (RRa-P3HT) and PCBM were purchased from Sigma Aldrich. All materials were used as received. To prepare the blend thin films, 12.5 mg RR-P3HT and 12.5 mg PCBM were dissolved in 1 ml chlorobenzene. The solution was stirred for 8 hours to fully dissolve before spin-coated on Si substrates (silicon wafers) at 1000 rpm for 60 s. Silicon wafers were cleaned for 30 min in piranha solution and then rinsed by DI water before spin coating. In thermal annealing studies, the blend thin films were annealed under nitrogen protection.

3.2.2 Temperature Control

During the thermotropic evolution, temperature increased at a rate of 10 °C/min from room temperature (~20 °C) to 100 °C. Each temperature was maintained for 1 min while measurements were taken under the protection of nitrogen.

During the programmed temperature dropping process, temperature decreased at a rate of 5 °C/min from 100 °C to 20 °C.

3.2.3 Cross-polarized Light Microscopy Images Measurement

Cross-polarized light microscopy images were taken with an ET605/70 filter (Chroma, Bellows Falls, VT) inserted in the incident light path of the cross-polarized light microscope. Dhyana 400BSI sCMOS camera (Tucsen Photonics, Fuzhou, China) was used as detector and a Zeiss EC Epiplan-Apochromat 100X objective (N.A. 0.95) was used to collected light signal. The camera’s exposure time was set to 110 ms in all imaging experiments.

3.2.4 Raman Spectroscopy Measurement

Raman spectra were obtained under the excitation wavelength of 488 nm. The laser power was ~0.13 µw before the beamsplitter and acquisition time was 2000 ms. Spectral resolution was ~1 cm^{-1}. Raman spectra were taken at 10 different regions at each temperature and the average spectrum was used to calculate the crystallinity.

3.2.5 Photoluminescence Measurement

Photoluminescence (PL) spectra were obtained under the excitation wavelength of 488 nm. The laser power was ~0.13 µw before the beamsplitter and acquisition time was 2000 ms. Spectral resolution was ~5 cm^{-1}. PL spectra were taken at 10 different regions at each temperature and the average PL spectrum was used to calculate the $I_{PL}^{0-0}/I_{PL}^{0-1}$.

3.3 Data Analysis

3.3.1 Cross-polarized Light Microscopy Images Analysis

Charge transport in solution-processed polymeric blend photoactive layers in BHJ solar cells is sensitive to grain boundaries, molecular alignment and orientation, (174-176) with much higher mobilities in semicrystalline polymer domains than amorphous polymers (177). It has been reported that different relative grain orientations lead to different charge transport barrier (175). The mesoscale orientational domains can affect essential optoelectronic properties, such as charge transport (178; 179) and absorption of unpolarized light (180).

Analysis of domain orientation and alignment can be achieved through the study of optical anisotropy, (181) while other characterization methods may struggle in generating contrast from the compositionally similar sample domains. It has been reported that the strong π-π interactions perpendicular to the conjugated backbone lead to the efficient packing and crystallization of many conjugated polymer. Resulting from the rigidity and planar conformation of the conjugated backbone of P3HT, efficient packing and crystallization occur in the blend films (172). Cross-polarized light microscopy images of the photoactive layers can uncover the orientation of the domains with respect to the electric field vector of the incident light beam. Similar results reported previously by transmission polarized X-ray microscopy (182). The image intensity is related to the angle between the electric field vector of the incident light beam and the anisotropic structures of the samples by the following equation (Figure 3.2):

$$I \approx sin^2(2x) \ldots\ldots\ldots\ldots\ldots\ldots\ldots\ldots\ldots\ldots\ldots\ldots\ldots\ldots\ldots\ldots..(1)$$

where I is the intensity of the cross-polarized light microscopy image and x is the angle between the polarization direction of the incident light and the domain's dominant orientational angle. The contrast in cross-polarized light microscopy images (Figure 3.3 A) results from different in-plane domain orientations relative to the polarization direction of the incident light. In comparison, unpolarized bright field images (Figure 3.3 B) cannot reveal the heterogeneity of domain's dominant orientations, suggesting the polarization-averaged images are remarkably homogeneous despite the large-scale orientational heterogeneity. Therefore, if the images from all polarization directions of incident light are added together, which means taking polarized light microscope images with incident lightbeams with all electric field orientations, then the resulting image after summation would be independent of the orientation of each domain. That explains why under bright field microscopy, no domain orientation features appear.

As shown in Figure 3.3 C, the image intensity distribution in cross-polarized images can be deconvoluted into three intensity peaks corresponding to the two dominant orientational domains (Peak 1, 3) and domain boundaries between them (Peak 2) in Figure 3.3 A. For same sample under unpolarized bright field image, only a single peak was obtained (Figure 3.3 D). The percentage of peak overlap (OP) which can be calculated using the following equation.

$$OP_{i,j} = \frac{1}{2}\left(1 - \frac{I_j - I_i}{0.5(W_i + W_j)}\right) = \frac{1}{2}(1 - 1.18 \times \frac{I_j - I_i}{W_{0.5hi} + W_{0.5hj}}) \ldots\ldots\ldots\ldots\ldots\ldots\ldots\ldots\ldots\ldots(2)$$

$OP_{i,j}$: Overlap percentage of peak i and peak j.

I_i: Peak i position in the image intensity distribution.

I_j: Peak j position in the image intensity distribution.

W_i: The peak width of peak i.

W_j: The peak width of peak j.

$W_{0.5hi}$: Full width half maximum (FWHM) of Peak i.

$W_{0.5hj}$: Full width half maximum (FWHM) of Peak j.

3.3.2 Raman Spectra Analysis

3.3.2.1 Raman Spectra of Regioregular P3HT and Regiorandom P3HT

Raman spectroscopy has been considered to be a powerful spectroscopy characterization technique for structural analysis (46; 183). On the other hand, Raman measurements are noninvasive under ambient conditions and no special sample preparations are required, (48; 49) hence, widely used to monitor the conformational changes of molecules in situ. In previous studies, symmetric in plane C=C stretching Raman mode of P3HT was used to distinguish different phases of P3HT in its blend with PCBM (184-186). It has been reported that the C=C peak position is sensitive to the degree of molecular order of P3HT (186) resulting from its sensitivity to π-delocalization of P3HT. The peak position is ~1449 cm^{-1} for regioregular P3HT (RR-P3HT) and ~1470 cm^{-1} for regiorandom P3HT (RRa-P3HT) under 488 nm excitation (Figure 3.4). RR-P3HT has a lower wavenumber than that of RRa-P3HT film resulting from that RR-P3HT backbone contains longer conjugated segments than that of RRa-P3HT (186). In Raman measurements, 488 nm was chosen as the excitation wavelength because at 488 nm, RR-P3HT and RRa-P3HT had comparable absorption features, hence, C=C stretch modes of RR-P3HT and RRa-P3HT regions had similar Raman intensity (186).

3.3.2.2 Raman Spectra of P3HT in the Photoactive Layer under Thermal Stress

The relative crystallinity of P3HT in the nonannealed and annealed RR-P3HT:PCBM blend film can be quantify by deconvolute the symmetric C=C stretch Raman mode of blend films into symmetric C=C stretch of RR-P3HT films and RRa-P3HT films, where the relative contributions of the two peaks are fitting parameters. The relative crystallinity can be quantify by the following equation (186):

$$Crystallinity_{RR-P3HT}(\%) = \frac{P_{R(RR-P3HT)}}{P_{R(RR-P3HT)}+P_{R(RRa-P3HT)}\times\left(\frac{\sigma_{RRa-P3HT}}{\sigma_{RR-P3HT}}\right)} \times 100 \text{..........(3)}$$

$P_{R(RR\text{-}P3HT)}$ is the Raman peak intensity or integrated area of the C=C stretch mode in RR-P3HT. $P_{R(RRa\text{-}P3HT)}$ is the Raman peak intensity or integrated area of the C=C stretch mode in RRa-P3HT. $\sigma_{RRa\text{-}P3HT}/\sigma_{RR\text{-}P3HT}$ is the relative Raman scattering cross-section of C=C mode in RRa-P3HT to RR-P3HT films, which is ~1.69 under 488 nm excitation wavelength (186).

As shown in Figure 3.5, the symmetric C=C stretch Raman mode of both as-cast and annealed P3HT: PCBM blend films are fitted well with a sum of RRa-P3HT and RR-P3HT spectra. Using this method, the change of relative crystallinity of P3HT in 1:1 P3HT: PCBM photoactive layers comparing to pristine regioregular P3HT thin films under thermal stress is quantitively characterized.

3.3.3 Photoluminescence Spectra Analysis

Different aggregates of polymeric semiconductors can exhibit different electronic interactions (187). Michael Kasha introduced the earliest models to study the photoluminescence (PL) spectra of molecular aggregates (188) and the models were developed and applied on polymeric semiconductors by Spano (187), based on which the different π-π aggregate types: H-favored aggregates and J-favored aggregates (189-191) resulting from different exciton delocalization along the stacking axis in a π-stack can be analyzed from the PL spectral lineshape (188).

The PL spectra of polymeric semiconductors can be deconvoluted into three emission energy: 0-0, 0-1 and 0-2, according to the weakly coupled H-aggregate model (Figure 3.6) (187). The 0-0 emission peak is substantially attenuated for H-favored aggregates and enhanced for J-favored aggregates in PL spectra of polymeric semiconductors (187; 189; 191). The electronic interactions among chromophores (chromophores can be one or group of repeat units in polymer) lead to distortions of the vibronic progression in PL spectra and therefore result in the changes of relative peak intensities (158; 187). This interaction-induced changes in the relative peak intensity show the exciton bandwidth, the nature of disorder, and the exciton coherence length within a π-stack (189-192). Therefore, the peak ratio of 0-0 to 0-1 emission peaks ($I_{PL}^{0-0}/I_{PL}^{0-1}$) were used in the experiments of this chapter to monitor the change of aggregate type of P3HT under thermal stress and after cooling down.

As shown in Figure3.7, the PL spectra of both as-cast and annealed P3HT: PCBM blend films were fitted well with a sum of 0-0, 0-1 and 0-2 emission spectra. Using this method, the change of $I_{PL}^{0-0}/I_{PL}^{0-1}$of P3HT in 1:1 P3HT: PCBM photoactive layers under thermal stress was quantitively characterized.

3.3.4 T_{cc}^{min}, T_{cc}^{max} and T_{cc} Calculation

T_{cc}^{min} and T_{cc}^{max} are defined as the beginning and ending temperatures of the cold crystallization process. T_{cc}^{min} corresponds to the temperature at which the crystallinity equals the crystallinity of the as-cast blend thin film plus the 5% the crystallinity difference between the as-cast film and the annealed film: (193)

$$Crystallinity_{cc}^{min} = Crystallinity_{as-cast} + (Crystallinity_{annealed} - Crystallinity_{as-cast}) \times 0.05 \text{..........(4)}$$

T_{cc}^{max} corresponds to the temperature at which the crystallinity equals the crystallinity of the as-cast blend thin film plus the 95% the crystallinity difference between the as-cast film and the annealed film: (193)

$$Crystallinity_{cc}^{min} = Crystallinity_{as-cast} + (Crystallinity_{annealed} - Crystallinity_{as-cast}) \times 0.95 \text{......(5)}$$

To determine the T_{cc}^{min} and T_{cc}^{max}, we first fitted the crystallinity-temperature correlation (Figure 3.8) with a sigmoid function (6):

$$Crystallinity = A_2 + \frac{(A_1 - A_2)}{1+\left(\frac{T}{T_0}\right)^p} \text{.......................................(6)}$$

T is temperature; A_1, A_2, p and T_0 are fitting parameters. Then, $Crystallinity_{cc}^{min}$ and $Crystallinity_{cc}^{max}$ were calculated using equations (4) and (5), followed with calculating T_{cc}^{min} and T_{cc}^{max} by solving equation (6).

T_{cc} was calculated as the peak position of the first derivative curve of the sigmoid function in (6) (Figure 3.8).

3.4 Results and Discussion

3.4.1 Thermotropic Realignment of Mesoscale Orientational Ordered Domains Characterized by Cross-polarized Light Microscopy Module under Thermal Stress

In this section, cross-polarized light microscope integrated with the home-built post treatment stage (the thermal annealing stage) which were able to provide thermal stress when measurements were taking place, was used to *in situ* characterize the thermotropic domain realignment of 1:1 P3HT: PCBM blend thin films in mesoscale and microscale. Characterization of the mesoscale and microscale orientational domains in the thin films is essential for understanding the optoelectronic properties, such as charge transport (178; 179) and absorption of unpolarized light (180).

Firstly, cross-polarized light microscopy was used to characterize the mesoscale and microscale features in the as-cast blend thin film of 1:1 P3HT: PCBM (as discussed in Data Analysis 3.3.1). The microscopy images captured under cross-polarized light microscope display domains of different contrasts (Figure 3.9 A), indicating that these mesoscale domains were anisotropic with dominant orientations (Data Analysis 3.3.1). Figure 3.9 A shows that the interface between micro size domains are not sharp and there are transition domains ~200 nm wide, whose domain orientation lies between the two large micro domains. Similar results were reported before by using X-ray microscope (182). During fast film deposition processes, for example, spin-coating, the films were dried under nonequilibrium conditions (172) and mesoscale to microscale orientational domains were generated. Other polycrystalline films processed by solution deposition, for example poly(9,9’-dioctylfluorene-co-benzothiadiazole) (F8BF) were reported as films composed of well-ordered micro size domains (182).

It has been reported that the ~200 nm domain boundaries are closely related to charge recombination in the film (182; 194). Because the mobility of charge carriers in the domains in which the polymer packed in the same orientation is much larger than that between domains in which direction of polymer packing is not aligned, the charge density in the domain boundaries is high and can result in charge recombination (182). The blue and red contrast regions gave rise to a bimodal distribution of pixel intensity (Figure 3.9 B), in which peak 1 represented blue domains, peak 3 represented red domains and peak 2 represented domain boundaries (195). (As discussed in Data Analysis 3.3.1) These experimental results suggest that the highly microcrystalline and anisotropic lamellar microstructure of P3HT on molecular level lead to anisotropic orientational ordered mesoscale and microscale domains in as-cast blend thin films.

Secondly, the dynamic changes of mesoscale domains were characterized by the cross-polarized light microscopy module as temperature increased from 20°C to 100°C. Thermotropic alignment of the mesoscale orientational domains occurred as shown by the images and image intensity distributions (Figure 3.10 and Figure 3.11). There was no change in image patterns and image intensity distributions from 20°C to 40°C. As temperature increased, realignment of domains occurred from 40°C until 70°C, starting from domain boundaries. Then the realigned blend thin film split into mesoscale domains with different dominant orientations again from 70°C to 100°C. As shown in Figure 3.11, in thermal annealing experiments, the intensity peak of domain boundaries began to increase after the sample was heated to the glass transition temperature (T_g) of ~30 °C (196). The blend thin film with highest orientational order was achieved at 70°C.

Moreover, the overlap percentages (OP) of peaks representing different orientational ordered domains and boundaries between domains in image intensity distribution of the blend thin film were also calculated to characterize the dynamic process of the realignment of mesoscale orientational ordered domains. (Figure 3.12) As shown in Figure 3.12**,** the largest percentage of peak overlap between peak 2, 3 and peak 1, 2 happened ~ 50 °C and ~ 70 °C, respectively. When increasing the temperature even higher (> 80 °C), the domain boundary reappeared as shown in Figure 3.11. Moreover, there were two stages of the merging process observed when temperatures raise from 20 °C to 100 °C. Firstly, from 40 to 50°C, domain boundaries (Peak 2 in Figure 3.11) fully merged with one of the domains (Peak 3 in Figure 3.11). Further increasing temperature (60 to 70 °C), the remained two domains started to merge with each other and primarily a single domain (Peak 1 in Figure 3.11) was generated. The changes of the overlap percentages (OP) of peaks with temperature coincided with the thermotropic alignment process of the mesoscale orientational domains.

3.4.2 Thermotropic Evolution of Relative Crystallinity (Molecular Order) of Photoactive Layers Characterized by Confocal Raman Spectroscopy Module under Thermal Stress

On the molecular level, confocal Raman spectroscopy module was used to *in situ* characterize the thermotropic evolution of crystallinity (molecular order or π-π stacking of molecules) in the 1:1 P3HT:PCBM photoactive blend thin films relative to a pristine regioregular P3HT film. Figure 3.13 shows the evolution of Raman spectra of 1:1 P3HT: PCBM blend thin film from 20°C to 100°C. The relative crystallinity of P3HT in the thin films has significant impact on optoelectronic properties such as, absorption wavelength and charge carrier mobility (186).

The C=C Raman peaks from P3HT in a blend thin film (Figure 3.14) can be deconvoluted into regioregular (RR, ordered) and regiorandom (RRa, disordered) peaks (Figure 3.4). The relative crystallinity of the P3HT blending with PCBM is quantified as the fraction of the ordered P3HT phase, i.e., the ratio of the RR peak to RRa peak (186). Details of Raman spectra analysis are provided in Data Analysis 3.3.2.

Overall, Figure 3.14 shows that the Raman peak of regiorandom (RRa) P3HT significantly decreases and that of regioregular (RR) P3HT significantly increases under the thermal stress from 20°C to 100°C, indicating an increase of crystallinity of P3HT in the blend thin film.

Figure 3.15 shows the changes of crystallinity calculated from the C=C Raman peaks with temperature from 20°C to 100°C. (Details are discussed in Data Analysis 3.3.2) The crystallinity began to increase slightly when temperature reached 30°C, which is the glass transition temperature(196) of the blend thin film and at which the polymer chains began to gain flexibility resulting from the high temperature. The crystallinity kept increasing between 30°C and 84°C indicating the commencement and completion of the cold crystallization process with cold crystallization temperature at 49°C which was the peak position of the first derivative curve of the crystallinity changing curve (Figure 3.8). From 84°C to 100°C, the increase of the peak ratio slowed down and became stable.

The crystallinity-temperature correlation (Figure 3.15) was fitted with a sigmoid function (Data Analysis 3.3.2). T_{cc} was then identified to be 49 °C from the first derivative curve of the sigmoid fitting function (Figure 3.8). Moreover, two other critical temperatures (T_{cc}^{min} and T_{cc}^{max}) that corresponded to the start and end of the cold crystallization process (193) were calculated (Data Analysis S3.4) to be 30 and 84 °C, respectively.

3.4.3 Thermotropic Transformation of Aggregate Type Characterized by Confocal Photoluminescence Spectroscopy Module under Thermal Stress

In this section, confocal PL spectroscopy is utilized to distinguish the two types of aggregates, that is, H-favored and J-favored (As discussed in Data Analysis 3.3.3), (187; 189-191) formed by emissive P3HT semiconductors. The type of aggregate depends on the relative alignment of the transition dipoles of adjacent molecules in stackings (197-199). On the molecular level, studies showed that J-favored aggregates offer higher exciton mobilities, larger exciton diffusion length (197; 198) and an order of magnitude higher in power conversion efficiency than H-favored aggregates (199).

Figure 3.16 shows the evolution of PL spectra from 20°C to 100°C. The PL spectra can be deconvoluted into 0-0, 0-1 and 0-2 emission peaks (Figure 3.17) (As discussed in Data Analysis 3.3.3). The 0-0 emission peak is substantially attenuated for H-favored aggregates, while enhanced for J-favored aggregates (187; 189; 191; 199). Therefore, the ratio of 0-0 to 0-1 emission peaks ($I_{PL}^{0-0}/I_{PL}^{0-1}$) can be used to identify different types of aggregate in the blend thin film (187). Details of PL spectra analysis are provided in Data Analysis 3.3.3.

As shown in Figure 3.17, the increasing rate of the $I_{PL}^{0-0}/I_{PL}^{0-1}$ was smaller from 20°C to 80°C than that from 80°C to 100°C. In Figure 3.18, the change of the peak ratio of 0-0 to 0-1 emission peaks ($I_{PL}^{0-0}/I_{PL}^{0-1}$) with increasing temperature was fitted with two piecewise linear functions, and the transformation temperature ($T_{H\text{-}J}$) from H- to J-favored aggregates (200) was identified to be ~ 77 °C from the intersection of the two linear functions. There are two stages of the $I_{PL}^{0-0}/I_{PL}^{0-1}$-temperature curve during the thermotropic evolution from 20°C to 100°C. The first stage was from 20°C to 77°C, where the peak ratio of 0-0 to 0-1 emission peaks ($I_{PL}^{0-0}/I_{PL}^{0-1}$) were attenuated and increased slowly with temperature indicating the aggregates generated during the cold crystallization process (as discussed in 3.4.2) were H-favored aggregates. The second stage was from 77°C to 100°C, where the peak ratio of 0-0 to 0-1 emission peaks ($I_{PL}^{0-0}/I_{PL}^{0-1}$) were enhanced indicating the transformation of H-favored aggregates to J-favored aggregates occured.

3.4.4 Multiscale Evolution of the Photoactive Layers in Bulk Heterojunction Solar Cells

The *in situ* correlative study using these three technique modules (cross-polarized light microscopy module, confocal Raman spectroscopy module and confocal photoluminescence spectroscopy module) offered a more complete understanding of the thermotropic evolution of 1:1 P3HT: PCBM blend thin films from multiscale. Three phase transition processes (glass transition process, cold crystallization process and H- to J-favored aggregate type transformation process) and their corresponding transition temperatures were identified when the temperature was raised from 20°C to 100°C.

As shown in Figure 3.10 and 3.11, transformations started after the sample was heated to above the glass transition temperature (T_g) of ~30 °C (196), when amorphous P3HT on molecular level began to obtain flexibility. The thermotropic realignment and merging of the mesoscale orientational domains was first observed at the domain boundaries (Figure 3.10 and Figure 3.11), where a higher amorphous polymer composition existed. The thermotropic realignment of orientational ordered domains described by the merging of overlap percentage of peaks in intensity distributions (Figure 3.12) agrees with the evolution process shown in Figure 3.10 and Figure 3.11. This is firstly followed by the cold crystallization process with commencement temperature (T_{cc}^{min}) at 30 °C, completion temperature (T_{cc}^{max}) at 84 °C and cold crystallization temperature (T_{cc}) at 49 °C. (Figure 3.15) (As discussed in 3.3.2) During the process of cold crystallization, enhanced flexibility of polymer chains at high temperature on molecular level leaded to a further merging of orientational domains and the most uniformly aligned blend thin film was achieved at

70°C (Figure 3.10). However, the blend thin film spilt into domains of various dominant orientations again at 80 °C (Figure 3.10). On the other hand, the attenuated $I_{PL}^{0-0}/I_{PL}^{0-1}$ indicated that H-favored aggregates were generated during the cold crystallization process on molecular level. Furthermore, the transformation from H- to J-favored aggregates ($T_{H\text{-}J}$) happened at ~ 77 °C (Figure 3.18) (Details in 3.4.3), resulting from the longitudinal stacking slip at high temperature. The temperatures (from 20°C to 100°C) were not high enough to melt the aggregates, and J-favored aggregates became dominant until 100°C. Finally, the melting process would happen at ~150 °C (201); however, it is beyond the technical limit of our spectro-microscopy system. Based on these results, the entire thermotropic evolution is depicted in Figure 3.19.

These in situ multiscale measurements unravel the thermotropic evolution process and provide direct experimental evidence for the optimization of the photoactive layers in BHJ solar cells. There are two optimization factors at the mesoscale and molecular level, respectively. On the mesoscale, blend thin films with high orientational order are favored because domain boundaries affect the charge carrier transportation adversely (202) and more uniform orientation results in higher charge mobility (195). Therefore, based on the characterization from mesoscale, thermal annealing temperature above ~70 °C is necessary (Figure 3.10). On the molecular level, studies showed that J-favored aggregates offer higher exciton mobilities, larger exciton diffusion length (197; 198) and an order of magnitude higher in power conversion efficiency (PCE) than H-favored aggregates (199). Hence, J-favored aggregates are preferred in photoactive layers in BHJ solar cells and thermal annealing temperature above the transition temperature $T_{H\text{-}J}$ (~77 °C) but lower than the cold crystallization of PCBM (~130 °C) (201) is necessary (Figure 3.18).

3.4.5 Effect of Programmable Temperature Dropping and Uncontrolled Temperature Dropping Processes on the Photoactive Layers in Bulk Heterojunction Solar Cells

After heating the 1:1 P3HT: PCBM blend thin film sample to 100 °C, we cooled the sample down to the room temperature while taking similar measurements using the spectromicroscopy system. The results are shown in Figure 3.20. Two temperature dropping methods were applied: programmed or uncontrolled temperature dropping, namely PTD and UTD, respectively. Mesoscale structures were restored and the orientational order in each domain was enhanced after programmed temperature dropping (Figure 3.20 top and Figure 3.21 a-d). In contrast, after uncontrolled temperature dropping, the patterns of the mesoscale orientational domains were lost, and a blend thin film with high orientational order was obtained (Figure 3.20 bottom, Figure 3.21 e-h). For the molecule-level structural information, there was no significant difference in the Raman spectra (Figure 3.20 B) or crystallinity (Figure 3.20 D, red) of the annealed blend thin film processed by two temperature dropping procedures. However, the photoluminescence spectra (Figure 3.20 C) were different. The $I_{PL}^{0-0}/I_{PL}^{0-1}$ (Figure 3.20 D, blue) of the blend thin film processed by uncontrolled temperature dropping was significantly higher than that processed by programmed temperature dropping (Student’s t-test p<0.005), which implies different types of polymeric aggregates obtained by the two temperature dropping procedures. As shown in Figure 3.18, there are two stages of the $I_{PL}^{0-0}/I_{PL}^{0-1}$-temperature curve during the thermotropic evolution. When temperature dropped quickly (uncontrolledly), the J-favored aggregates were maintained; however, during the programmed temperature dropping, the polymeric aggregates changed gradually and were able to transform from J-favored back to H-favored. Combining information of mesoscale and molecular level, the results explain why the fast temperature dropping process is preferred as post-treatment for photoactive layers.

3.5 Conclusion

In summary, the *in situ* multiscale spectromicroscopy system successfully characterized the photoactive layers of BHJ solar cell in a wide range of length scales (from molecular level to mesoscale) under thermal stress. The correlative evolution of mesoscale structures and molecular conformations was revealed experimentally. The optimized thermal annealing temperature window and preferred temperature dropping operation in thermal annealing were therefore identified based on the three phase transition stages with their critical transition temperatures during the thermotropic evolution. The molecular packing can be effectively tuned by temperature and post-treatment operation. Through this study, we demonstrate the essential capability of in situ characterization at multiple length scales in monitoring the morphology evolution, phase development and idendifying critical changes of complex functional materials under external stimuli. The 1:1 P3HT:PCBM blend active layer is not a special case but rather an example for many polymeric semiconductors widely applied in optoelectronic devices and the spectromicroscopy imaging system provides a platform for all of them having more or less rigid chains and prone to self-assemble to mesoscale structures to be *in situ* characterized under certain environment. Benefit from the home-built platform, the system is configurable and ready to integrate other modules in future, for example, electrochemical characterization modules, to corelate morphology and chemical changes with optoelectrical properties.

3.6 Figures

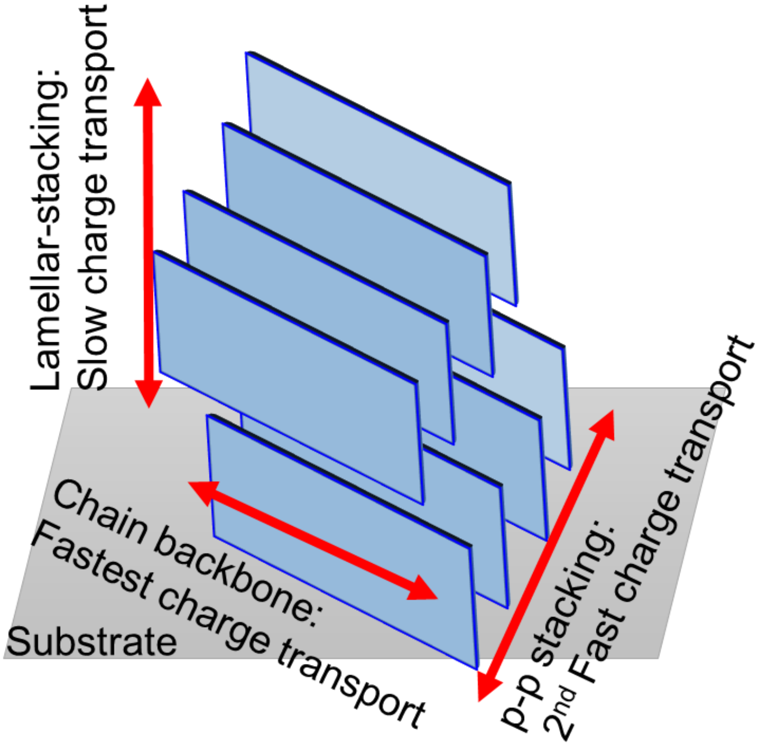

Figure 3.1. Schematic illustration of charge transport in conjugated polymers.

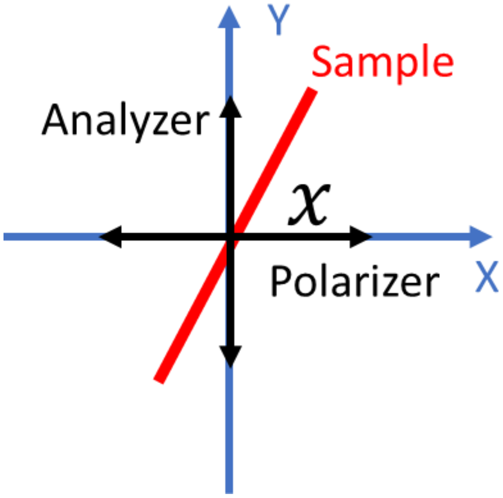

Figure 3.2. Schematic setup of cross-polarized light microscope and the sample.

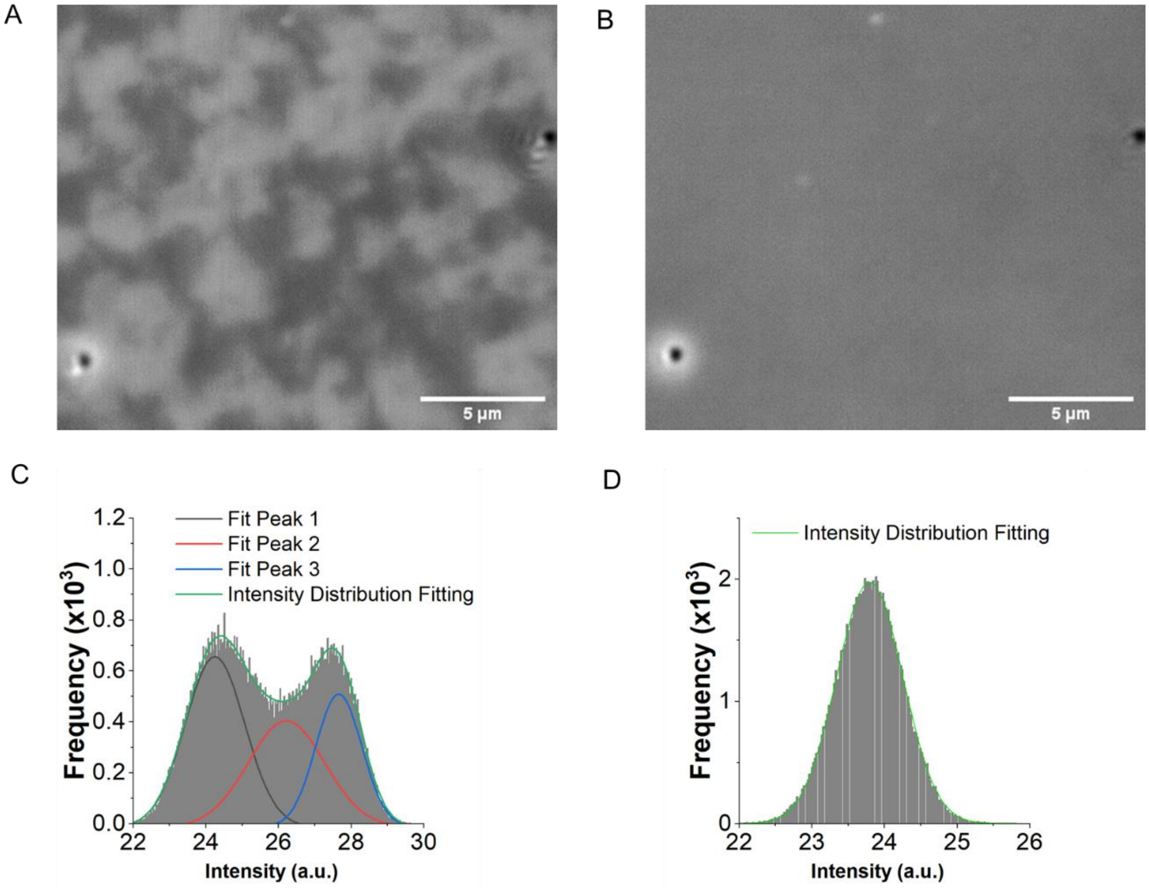

Figure 3.3. Optical microscopy images of a 1:1 P3HT: PCBM blend thin film and their corresponding image intensity distributions. (A) The crossed-polarized light microscopy image. (B) The bright field microscopy image. (C) Image intensity distribution of the crossed-polarized light microscopy image in (A). (D) Image intensity distribution of the bright field microscopy image of (B).

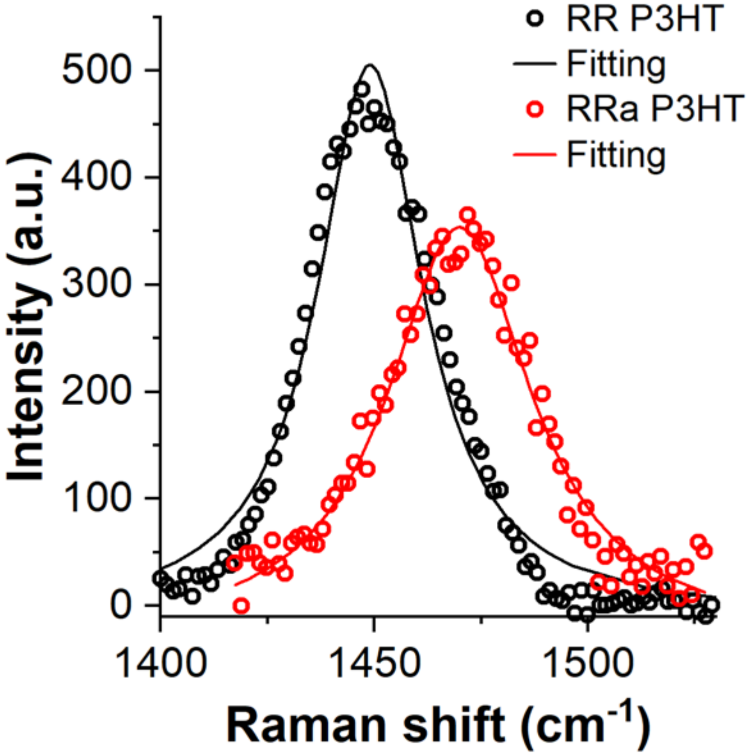

Figure 3.4. Raman spectra of regio-regular (RR) P3HT and regio-random (RRa) P3HT.

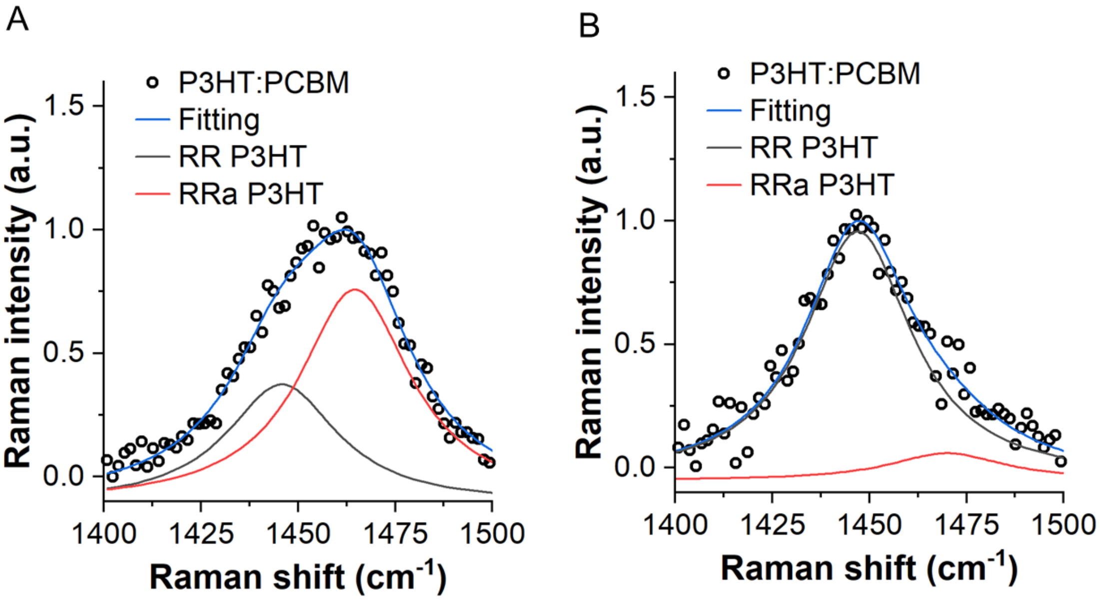

Figure 3.5. Raman spectrum of the (A) as-cast and (B) annealed P3HT: PCBM blend thin film. The Raman spectra are obtained by averaging the spectra obtained at 10 different regions in the sample area.

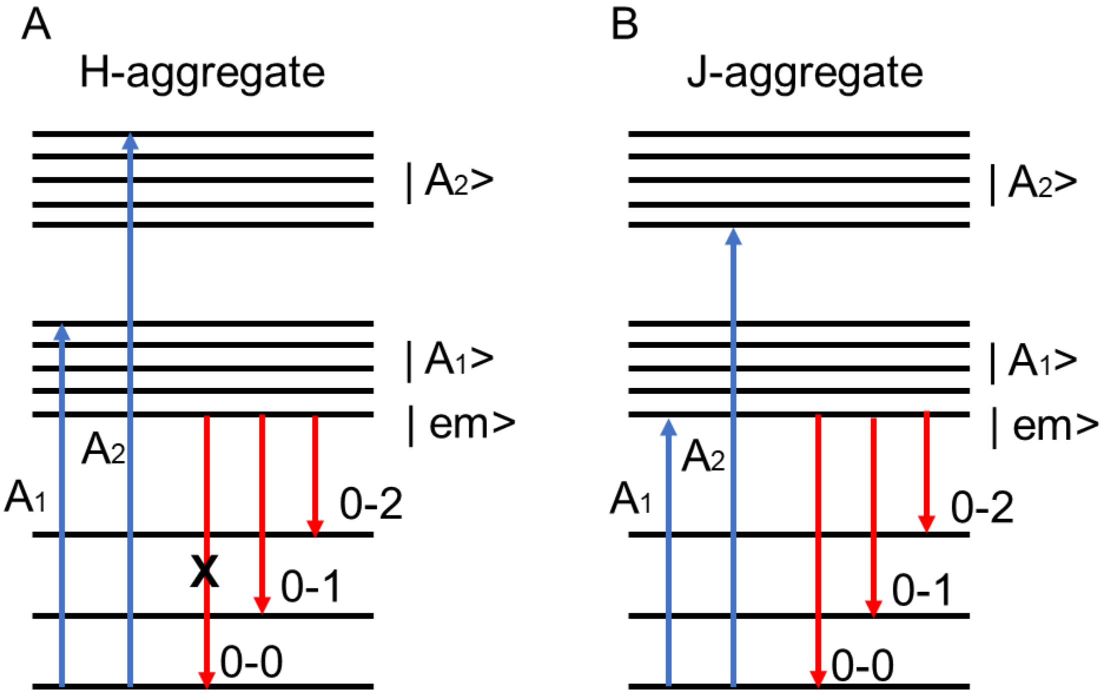

Figure 3.6. Approximate Jablonski diagram of ideal (A) H-aggregates and (B) J-aggregates corresponding to the weak exciton coupling regimes.

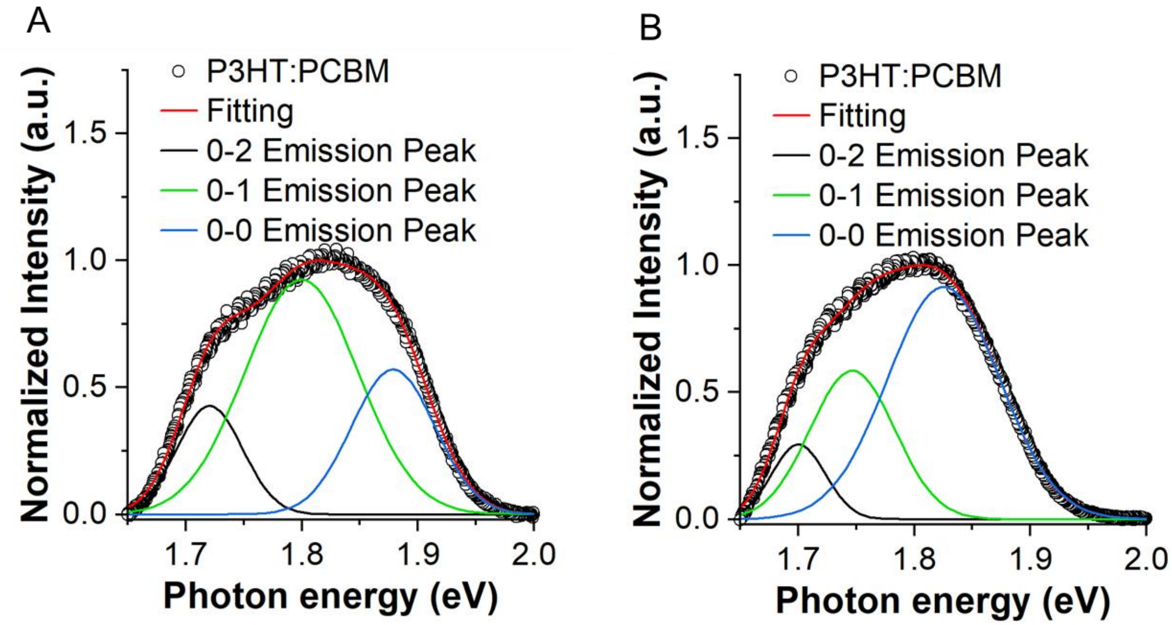

Figure 3.7. Photoluminescence (PL) spectrum of the (A) as-cast and (B) annealed P3HT: PCBM blend thin film. The photoluminescence spectra are obtained by averaging the spectra obtained at 10 different regions in the sample area.

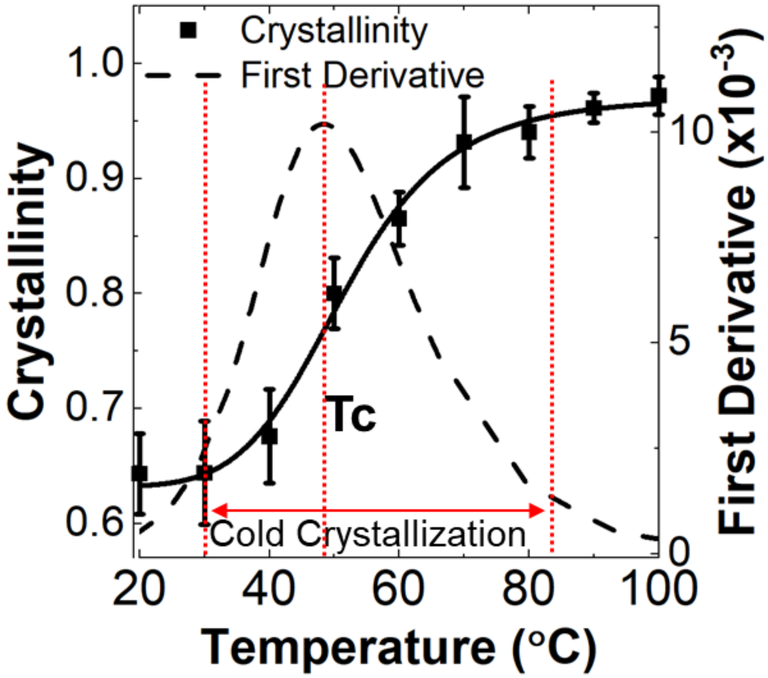

Figure 3.8. The evolution of crystallinity under thermal stress and the first derivative curve of the crystallinity fitting curve. Tc is the cold crystallization temperature, which is identified by the peak position of the first derivative curve. The solid line is the sigmoid fitting line of the change of crystallinity with temperature.

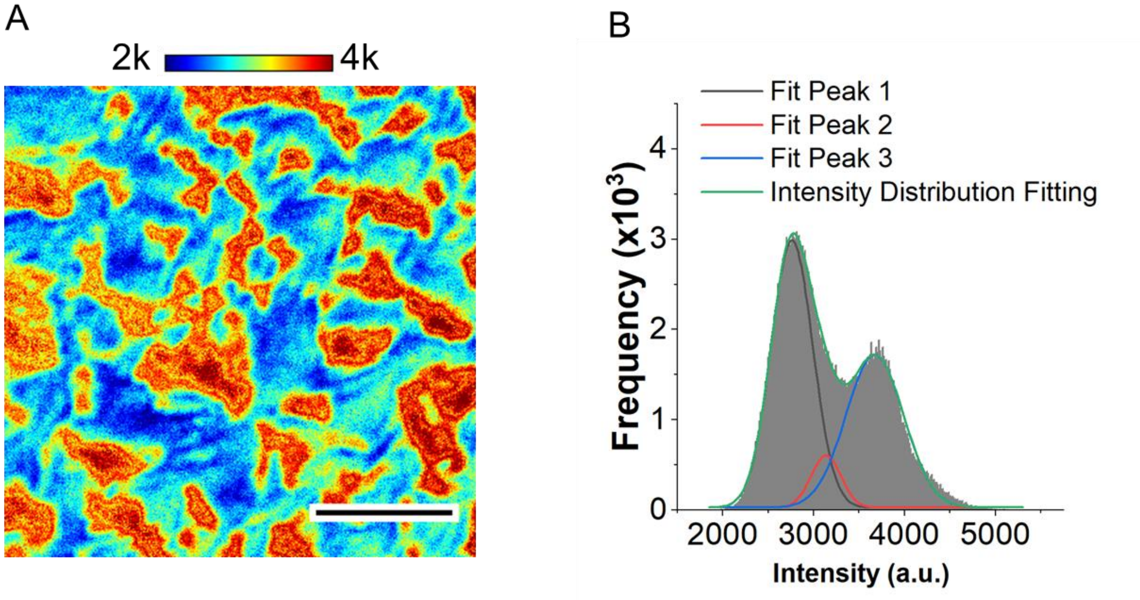

Figure 3.9. (A)The cross-polarized light microscopy image of P3HT: PCBM blend thin film on Si substrate. (B) Image intensity distribution of (A). The scale bar is 5 µm.

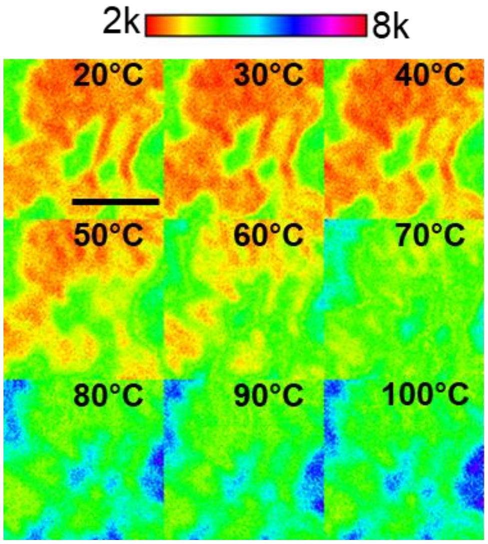

Figure 3.10. The evolution of P3HT: PCBM blend thin film under the cross-polarized light microscopy. The scale bar is 2.5 µm.

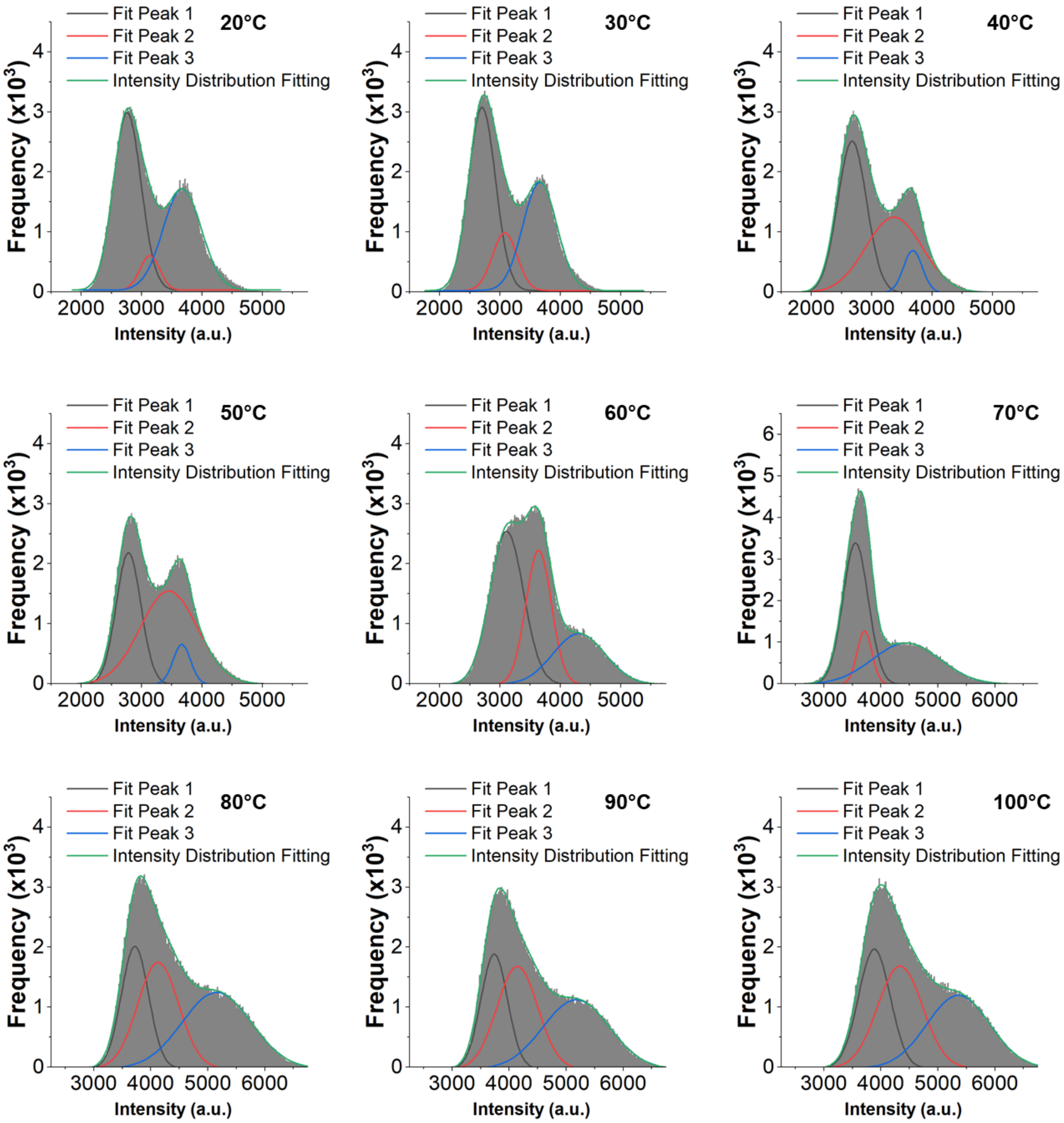

Figure 3.11. Thermotropic evolution of image intensity distributions of 1:1 P3HT: PCBM photoactive layer from 20°C to 100 °C.

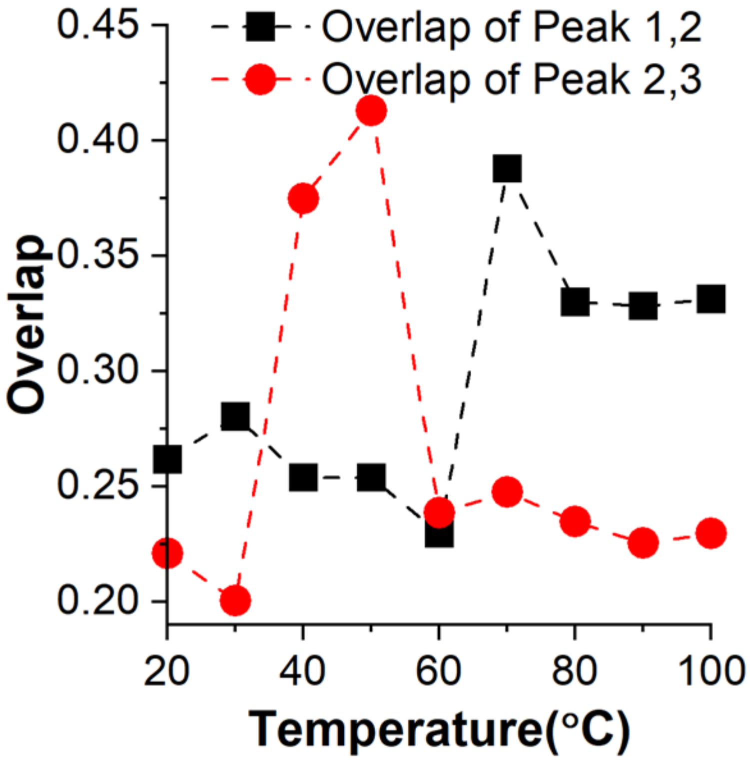

Figure 3.12. The change of overlap percentage of peak 1, peak 2 and peak 2, peak 3 in Figure 3.11 with temperature. The dash line is a guide to show the potential trend.

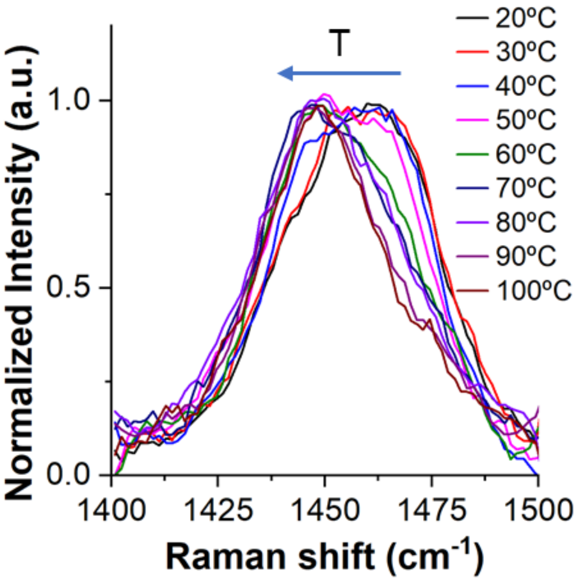

Figure 3.13. The evolution of Raman spectra of P3HT: PCBM blend thin film.

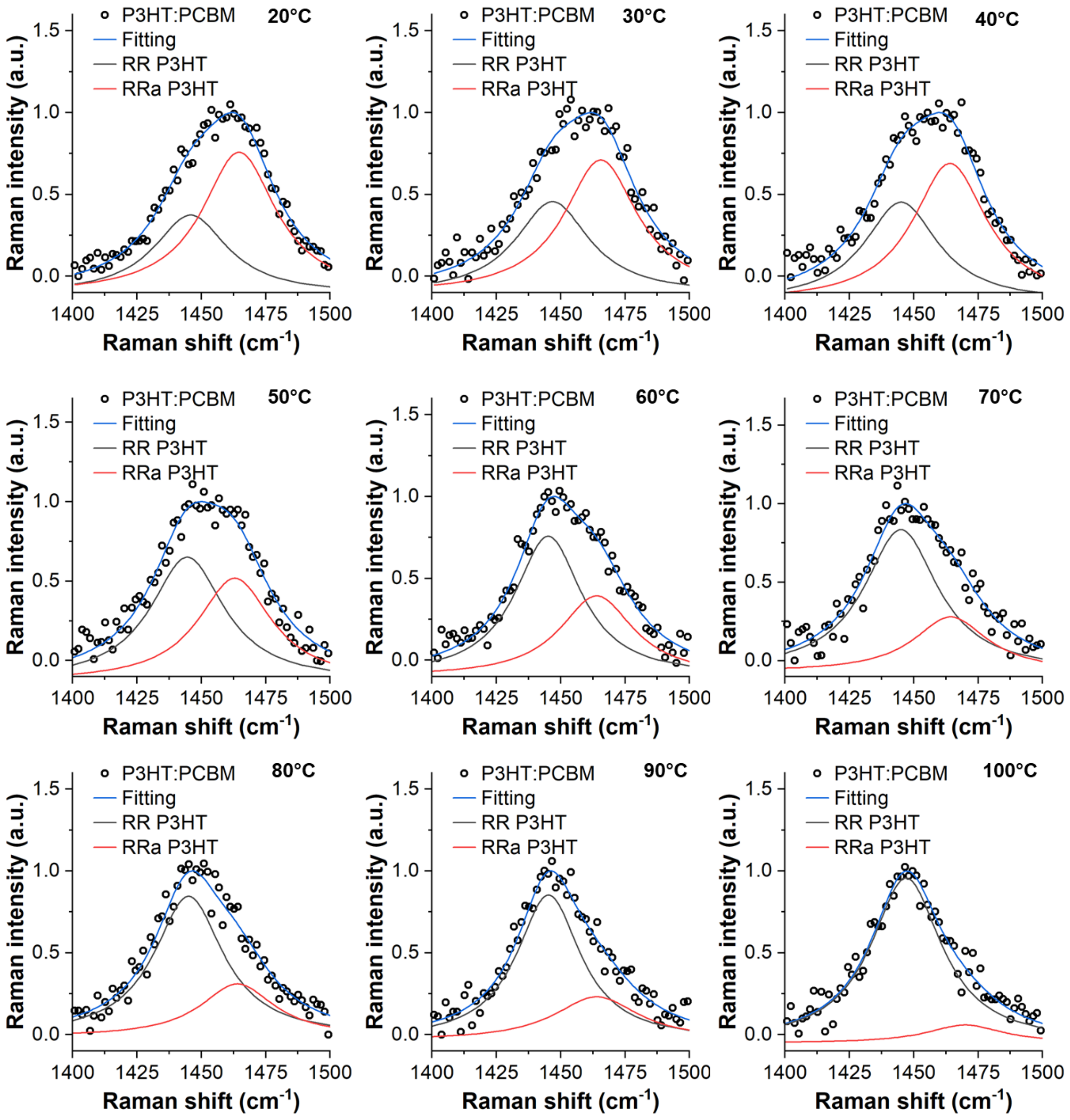

Figure 3.14. Raman spectra of 1:1 P3HT: PCBM blend thin film from 20°C to 100 °C. The Raman spectra are obtained by averaging the spectra obtained at 10 different regions in the sample area.

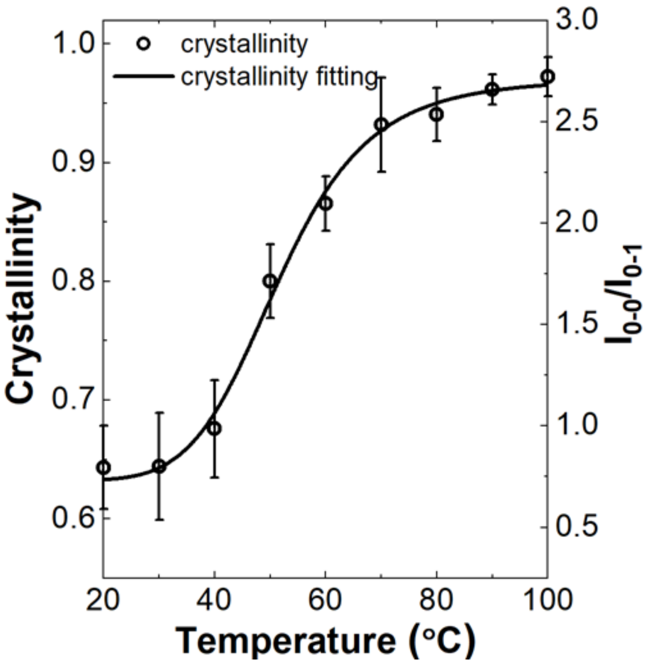

Figure 3.15. The evolution of crystallinity calculated from Raman spectra. The solid line is the sigmoid fitting line of the change of crystallinity with temperature. The error bars show the standard deviations of 10 measurements.

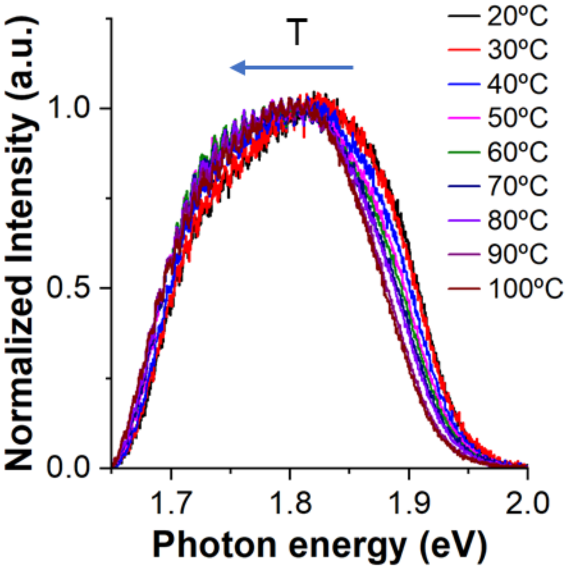

Figure 3.16. The evolution of Photoluminescence (PL) spectra of the P3HT: PCBM blend thin film.

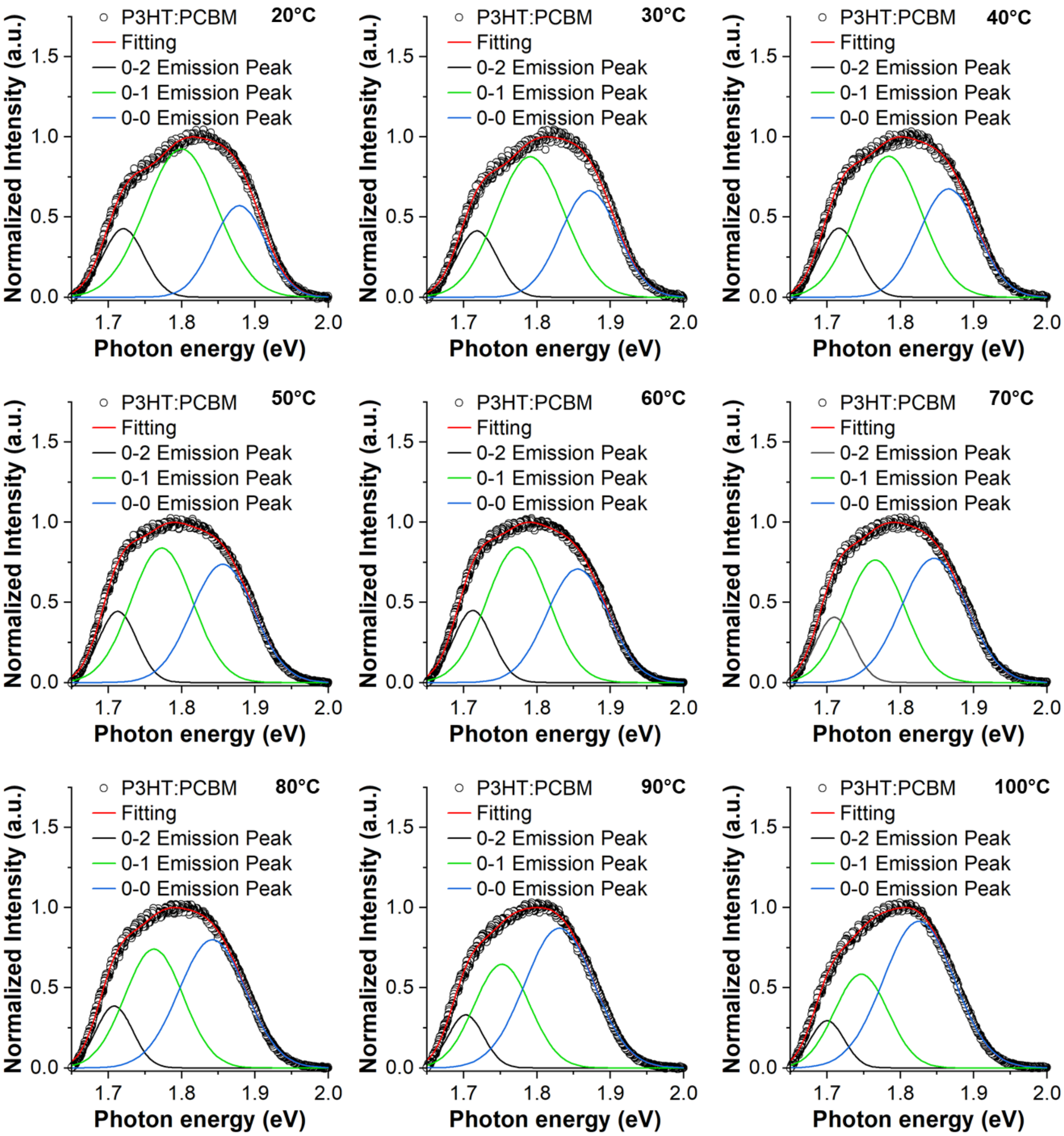

Figure 3.17. Photoluminescence (PL) spectra of 1:1 P3HT: PCBM blend thin film from 20°C to 100 °C. The PL spectra are obtained by averaging the spectra obtained at 10 different regions in the sample area.

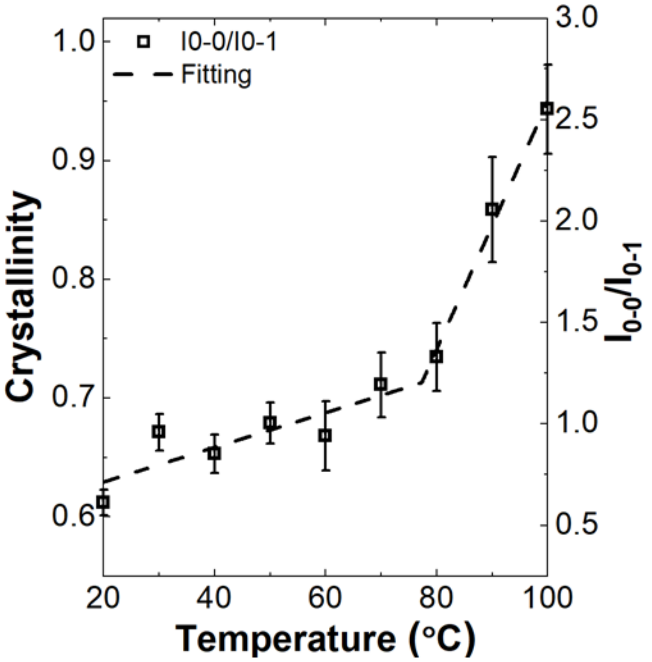

Figure 3.18. The evolution of I_{0-0}/I_{0-1} calculated from PL spectra. The dash line is the two piecewise linear fitting of the change of I_{0-0}/I_{0-1} with temperature. The error bars show the standard deviations of 10 measurements.

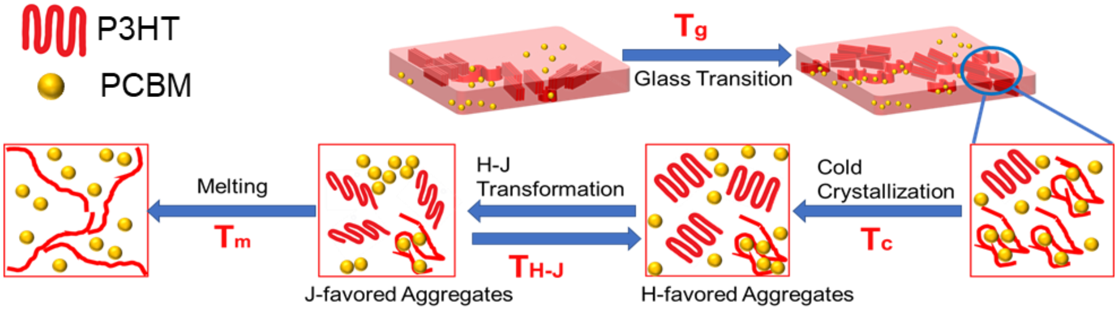

Figure 3.19. Proposed mechanism of the thermal evolution process.

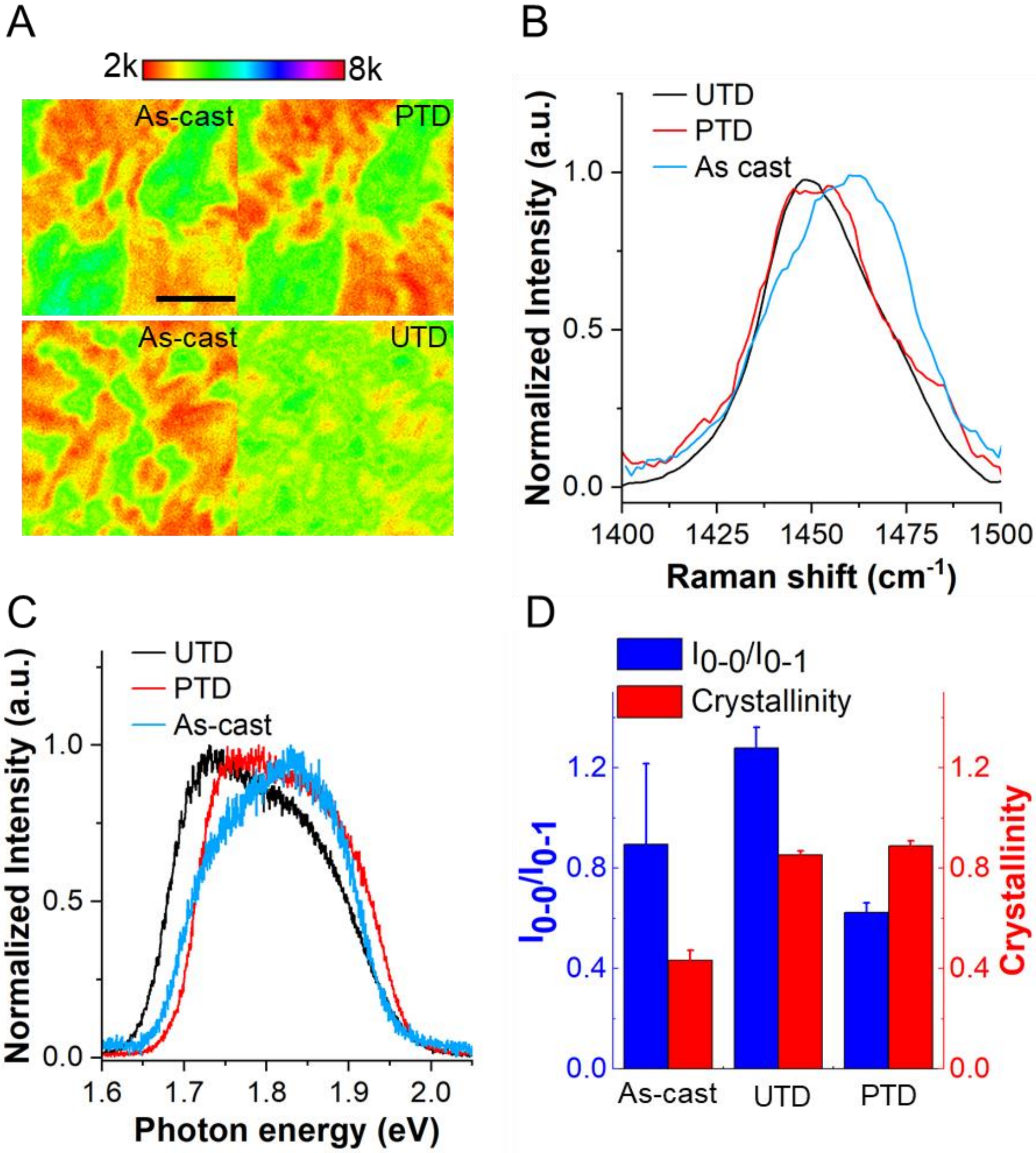

Figure 3.20. Comparison of 1:1 P3HT: PCBM blend thin film processed by programmed and uncontrolled temperature dropping. (a)The top two images are the P3HT: PCBM blend thin films as-cast and its corresponding film after programmed temperature dropping (PTD), respectively. The bottom two images are the P3HT: PCBM blend thin films as cast and its corresponding film after uncontrolled temperature dropping (UTD), respectively. (b)Typical Raman spectra of as-cast, PTD and UTD P3HT: PCBM blend thin film. (c)Typical PL spectra of as-cast, PTD and UTD P3HT: PCBM blend thin films. (d)The I_{0-0}/I_{0-1} and crystallinity of as-cast, PTD and UTD P3HT: PCBM blend thin films. The error bars show the standard deviations of 10 measurements.

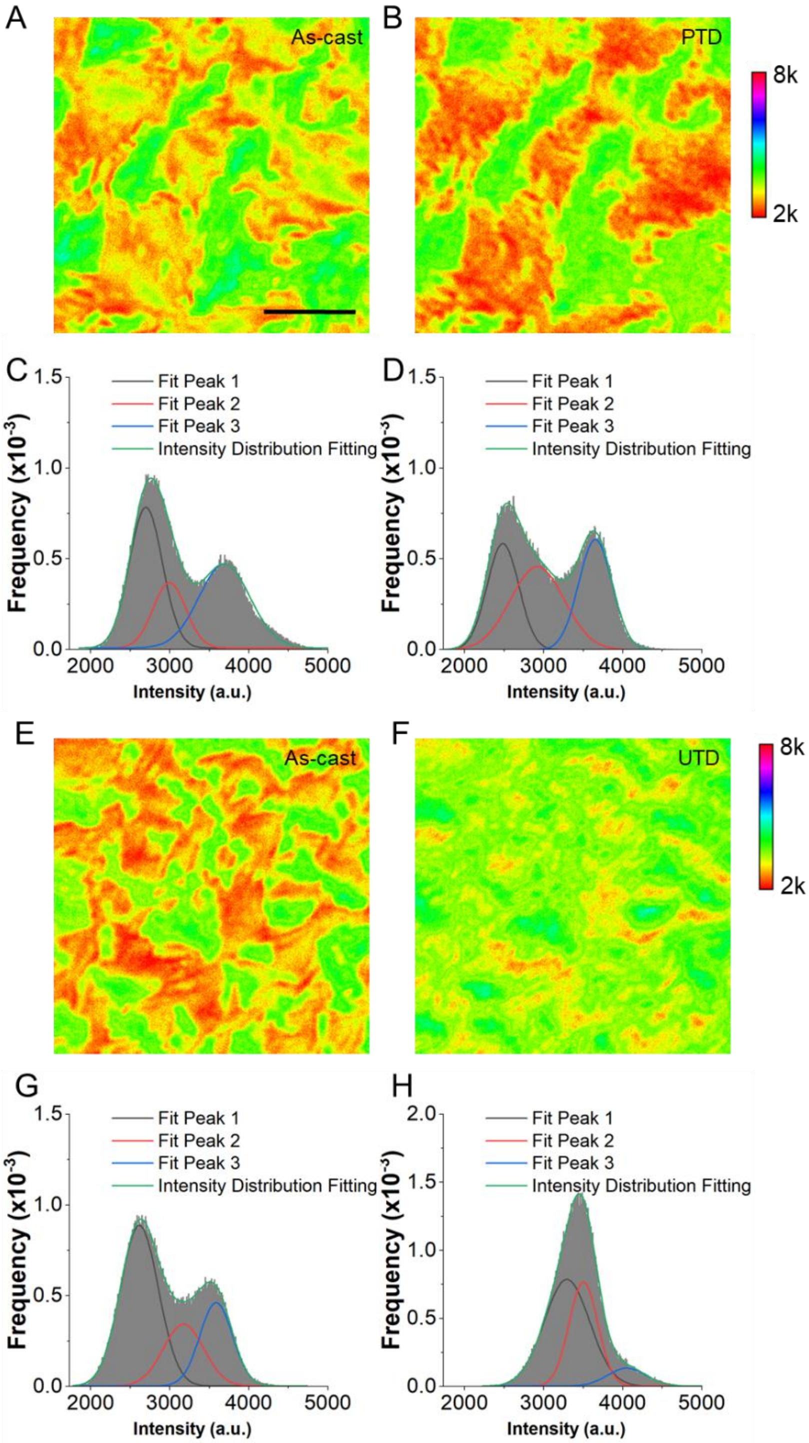

Figure 3.21. Cross-polarized light microscopy images of 1:1 P3HT: PCBM blend thin film (A) As-cast. (B) After programmed temperature drop (PTD). (C) Image intensity distribution of (A). (D) Image intensity distribution of (B). Cross-polarized light microscopy images of 1:1 P3HT: PCBM blend thin film (E) As-cast. (F) After uncontrolled temperature drop (UTD). (G) Image intensity profile of (E). (H) Image intensity profile of (F). The scale bar is 5 µm.

4 OTHER APPLICATIONS OF THE MLTI-MODALITY SPECTRO-MICROSCOPY IMAGING SYSTEM

4.1 Introduction

In many cases, the visualization and characterization of nanostructures is typically performed by a series of invasive or destructive techniques such as scanning electron microscopy (SEM), transmission electron microscopy (TEM), and atomic force microscopy (AFM) (203). While these techniques provide high-resolution images, little information about the optical characteristics can be gathered directly. In addition, surface characterization techniques do not have the ability to follow dynamic processes in real time as compared to optical microscopy techniques such as DIC, total internal reflection scattering (TIRS) microscopy (204; 205) and dark-field microscopy (206; 207), which have been applied to the studies of both the optical characterization of nanoparticles/ nanostructures and the investigation into real-time dynamics (2; 4; 11; 13).

Many substrates used in material sciences, for example, silicon wafer used in solar cells and gold coated glass slides used in surface enhanced Raman scattering (SERS) measurements are reflective. On the other hand, the formation of metallic nanoparticles and nanostructures is fundamentally interesting due to their applications in electronics (208-210), optoelectronics and plasmonic (211-217), chemical sensing and biosensors (218-223), and medical diagnostics and therapies (224-226). The fabrication of many of these materials is done through lithographic means typically taking place on reflective surfaces such as silicon wafers. The wide application of these particles and structures depends upon their optical, electronic, and catalytic properties that can be finely tuned over a broad range by controlling their size, shape, and composition (227-229). Many interesting particles and structures have been developed such as particle multi-mers (230), pyramids (206), bowties (231), nanoholes (232; 233), and many others. In 1979 Lessor *et. al.* developed the reflected Nomarski DIC (RDIC) configuration and applied it towards surface topography studies (148). Differential interference contrast (DIC) microscopy, which is an interferometric detection technique, is able to provide images of sample surface features with enhanced contrast. Traditionally, RDIC has been used to both qualitatively and quantitatively report surface roughness while studying polishing techniques, but it has also found much use in visualizing details and defects in semiconductor chips made on silica wafers (234). In the meanwhile, the confocal spectroscopy can provide chemical information for samples on reflective surfaces. Herein, the RDIC module and confocal spectroscopy module of the spectro-microscopic imaging system are applied to characterize material and cell samples on silicon wafer substrates and gold coated glass slides.

4.2 Sample Preparation and Experimental Measurement

4.2.1 Isotropic Nanospheres and Anisotropic Nanorods

The solution of gold (80 nm, 60 nm and 40 nm), polystyrene (PS) (240 nm, 200 nm, 150 nm and 100 nm) nanospheres or gold nanorod (40 x 118 nm (Nanopartz, Loveland, CO)) was drop cast on a clean silicon wafer and covered by a 25 mm^2 Corning coverslip, sealed with enamel.

Zeiss 100X Plan Apo/1.40 oil immersion objective was used to collected signals for isotropic nanospheres and anisotropic nanorods samples. NIH ImageJ was used to analyze the collected images and videos.

4.2.2 Graphene

Monolayer graphene made by chemical vapor deposition was bought from Graphenea, Inc. Cambridge, MA. Image exposure time was set to 100 ms. A 532 nm filter bought from Semrock, Rochester, New York was used in the incident light path of RDIC microscope. Zeiss 100X EC Epiplan-Apochromat air objective was used to collected signals.

4.2.3 Bulk Heterojunction Solar Cell Photoactive Layers

Sample preparation of the photoactive layers are described in 3.2.1.

4.2.4 Cells

A549 human lung cancer cells (ATCC, CCL-185) were used in the cell imaging section. Zeiss 100X Plan Apo/1.40 oil immersion objective was used to collected signals. Cells were cultured on glass coverslip. Two pieces of double-sided tape were used between the coverslip and glass slide to construct a chamber. Phosphate-buffered saline (PBS) was added to the chamber. NIH ImageJ was used to analyze the collected images and videos.

4.3 Results and Discussion

4.3.1 Characterization of Nanomaterials

4.3.1.1 Isotropic Nanospheres

DIC microscopy is advantageous for live cellular characterizations since there is no need for fluorescent labels. Comparison among DIC, bright-field, and dark-field microscopy on their characterizations on a single cell has been reported by Tsunoda, *et al.* in 2008, showing the optical sectioning capability of DIC in minimization of interference from cell features located outside the focal plane (235). Without the need for staining, observations using DIC microscopy can last for several hours with minimal disturbance to the biological samples. Simultaneous observation of both nanoparticles and a cancer cell during the endocytosis process (236), and the recording of 40 nm gold nanospheres going through endocytosis (237) have been demonstrated by using DIC microscopy. Figure 4.1 A-D show the RDIC images of gold nanospheres of different sizes. Within the surface plasmon resonance (SPR) wavelengths, an isotropic gold nanoparticle has a consistent appearance no matter the orientation of the particles in relation to the transmission axis of the polarizer. As expected, the contrast of RDIC images decreases with the decreasing size of the gold nanoparticles (Figure 4.1 A-C) and RDIC image contrast can be enhanced by increasing the exposure time (Figure 4.1 D). Figure 4.1 E-H show the RDIC images of polystyrene (PS) nanospheres with different sizes.

4.3.1.2 Anisotropic Nanorods

Different from the isotropic nanosphere, the rotation of an anisotropic nanoparticle can change the RDIC image appearance among all-dark, half-bright and half-dark, and all-bright depending on its orientation. Anisotropic gold nanorods (AuNRs) display a distinct pattern under DIC microscopy that can be used for orientation determination (238; 239) and rotational studies (239-241). Depending on the orientation of the long axis of the particles, the intensity of the bright and dark patterns of the particle can vary from appearing entirely bright, to half dark and half bright, to entirely dark (Figure 4.2).

Figure 4.2 depicts the images of the 40 nm x 118 nm AuNRs under 700/13 nm illumination with 100 ms exposure time. The particles exhibit a range of patterns due to their random orientations upon the surface. Figure 4.3A shows the RDIC images of a single AuNR at different orientations in the plane of the substrate. Figure 4.3B shows the periodic changes of the bright/dark intensities of the AuNR with its in-plane orientation angle. The orientation of the gold nanorod, i.e., the angle ϕ between the projection of nanorod's long axis and the x-polarization direction as defined in Figure 4.3C, can be determined using the bright or dark intensities of its DIC images collected at 700 nm. As reported previously, there is a $\sin^2$ ($\cos^2$) relationship between the relative brightness $\Delta I/\Delta I_{max}$ (the relative darkness $\Delta I'/\Delta I'_{max}$) of the image of a nanorod and ϕ (242). The relative brightness and relative darkness are measures of effective projections of the nanorod onto the two polarization directions.

4.3.1.3 Graphene

Monolayer graphene has attracted a large amount of interest because of its novel optoelectronic properties (243; 244). It has been reported that the monolayer graphene can be identified by optical microscopy taking advantage of the light interference (245-247). Figure 4.4 A and B show the images of monolayer graphene made by chemical vapor deposition (CVD) under bright field microscope and RDIC microscope. The feature contrast in RDIC image is significantly enhanced at the direction perpendicular to the shear direction of RDIC microscopy comparing to that in bright field microscopy.

Raman spectroscopy is a powerful technique in the characterization of 2D materials such as graphene (248-254). Different parameters such as peak height, peak position, full width at half maximum (FWHM) of major peaks and peak ratios are used to identify different structural features of graphene such as layer numbers (255; 256), defects (257-259), stacking configurations (260-262) and interlayer coupling (263-266). The thickness of graphene can significantly affect its electrooptical (267), thermal (268) and mechanical properties (269).

G peak and 2D peak are the two most intense Raman peaks in graphene samples (249; 253; 254; 256). The G peak results from the doubly degenerate zone center E_{2g} mode (in-plane vibration of sp^2 carbon atoms) and 2D peak is due to the second order of zone-boundary phonons (249; 256). As the thickness of graphene sample increases, the peak intensity ratio of 2D and G peaks decreases (249; 253; 254). Figure 4.4 C shows the Raman spectra of two areas with different contrast in the RDIC image of the CVD monolayer graphene. The ratio of 2D peak to G peak in area 1, which shows darker contrast under RDIC is smaller than the ratio in area 2, which shows brighter contrast under RDIC.

4.3.1.4 Nanoarrays

Benefit from the rapid development of nanofabrication, the interaction between light and nanostructured materials has been widely studied these years (232; 233; 270-273). A rich interesting experimental phenomena have been reported from the study of the interaction between nanoarrays and light (274-281). It has been reported that the geometry, spatial distribution and surrounding medium of nanoarrays can significantly affect the frequency range and locations of coupled resonances for surface plasmon resonance (SPR) (281; 282).

Figure 4.5 shows nanoparticles created on silicon wafers through lithographic means. The gold nanoparticles are thermal deposited onto the substrate. Due to the boat structure of the template, the path difference that the light takes entering and reflecting off the substrate gives rise to the RDIC pattern. Figure 4.5 are SEM and RDIC images, respectively, of gold particle monomers, dimers, trimers and tetramers made within the template. The orientation of the RDIC image corresponds to that of the SEM. It can be seen that RDIC images of 0- and 90-degrees orientation gives high contrast for both column and rows for all samples. However, RDIC images of 45-degrees have high contrast at the direction that is perpendicular to the shear direction of the Nomarski prism and low contrast at the direction of shear direction.

4.3.1.5 Photoactive Layers in Bulk Heterojunction Solar Cells

The RDIC integrated with confocal spectroscopy was applied to characterize the photoactive layers (1:1 P3HT: PCBM) in BHJ solar cells deposited on silicon wafer. Figure 4.6 A and B show the comparison of the image of 1:1 P3HT: PCBM thin film under bright field microscope and RDIC microscope. Domains with different contrasts were revealed by RDIC microscopy and hidden by the bright field microscopy. Figure 4.6 C and D show the Raman and photoluminescence (PL) spectra of the sample in Figure 4.6 B. Data analysis of the Raman and PL spectra is provided in section 3.3.2. Figure 4.6 E shows a PCBM crystal embedded in P3HT matrix observed under RDIC microscope. By using the confocal Raman spectroscopy, a line scanning across the PCBM crystal was conducted and the crystallinity of the sample along the scanning line were calculated (Figure 4.6 F). Under RDIC, it shows that the PCBM crystal is surrounded by a circle of darkest region in the image area which is characterized by Raman as a highly crystallized P3HT region.

4.3.2 3D Scanning of Cell Samples

Nomarski type DIC microscopy has been proven to be powerful in the characterization of cellular features due to the nonintrusive nature of DIC microscopy (2; 13; 242; 283-285). Resulting from the large numerical aperture (N.A.) of the condenser and objective used in DIC microscopy, DIC microscopy can provide better axial resolution than both dark field microscopy and bright field microscopy (4; 235; 286) and give sharper images for cell samples without suffering signals from cell structures out of focus plane. Figure 4.7 shows the RDIC images of A549 cells cultured on a silicon wafer. Due to the optical sectioning capability of RDIC microscopy, 3D scanning of A549 cell samples was obtained (Figure 4.8).

4.4 Conclusions

It has been demonstrated that the RDIC integrated confocal spectroscopy can be applied to study materials and cell samples on reflective surfaces. Samples of nanoparticles, 2D material, polymeric blend thin films and cells were tested on the instrument. It is expected that RDIC integrated confocal spectroscopy will become a useful tool in characterizing nanofabrication on reflective surface as an alternative to more expensive methods such as SEM, TEM, and AFM. The system also allows for the observation of dynamic processes such as self-assembly or monitoring the stability of structures in changing conditions.

4.5 Figures

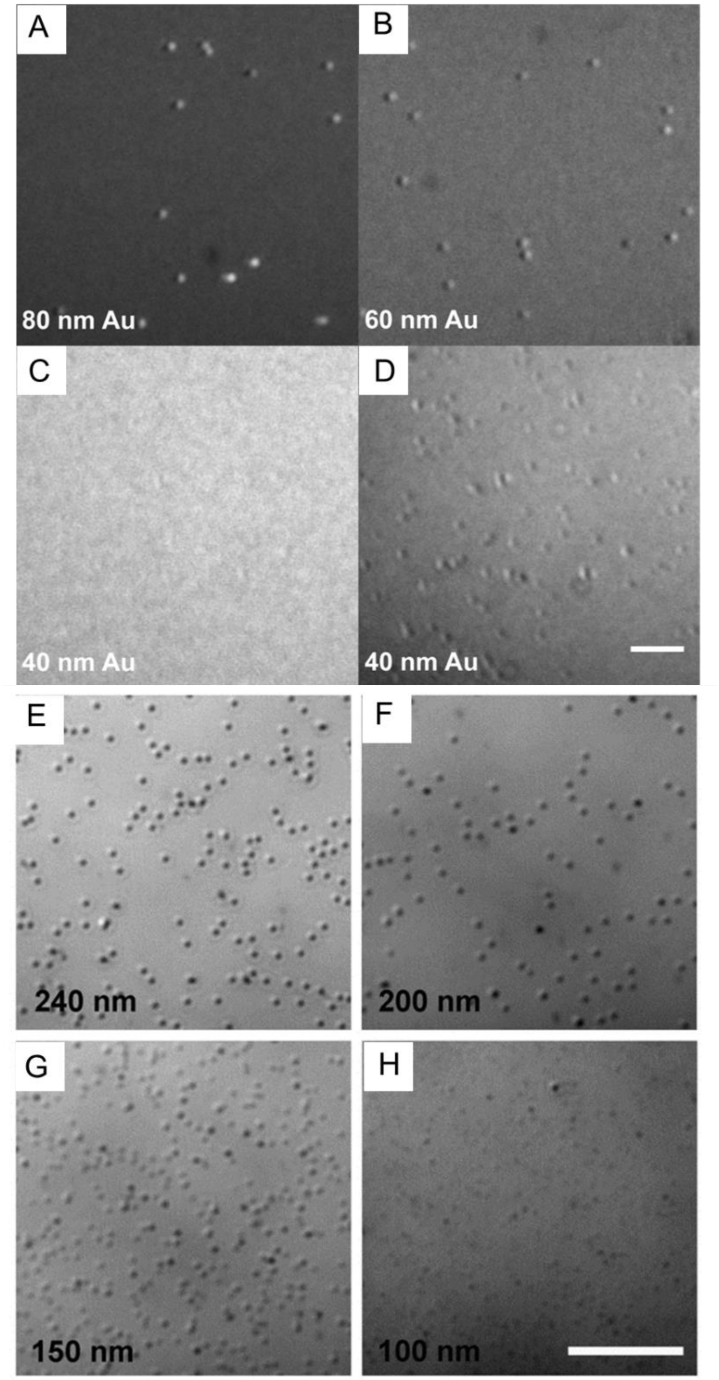

Figure 4.1. Examples of PS nanobeads and gold nanospheres imaged under RDIC. (A-C) correspond to 80 nm, 60 nm, and 40 nm gold nanospheres in diameter respectively. (D) is the same area as (C) with 20 images summed. (E-H) correspond to 240 nm, 200 nm, 150 nm, and 100 nm in diameter PS nanospheres respectively. All exposure times are 50 ms. Scale bar is 2 µm.

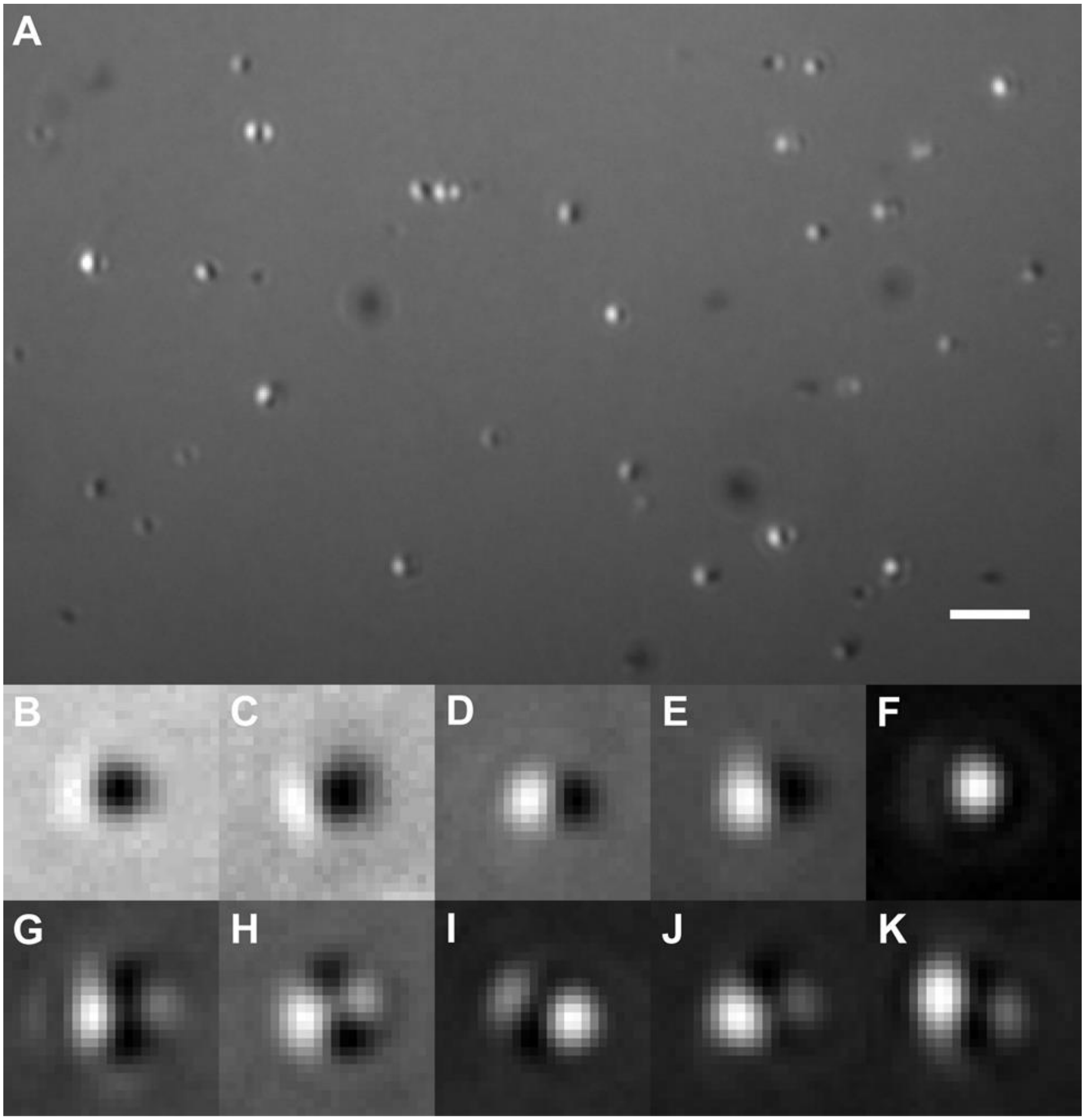

Figure 4.2. Gold nanorods (40x118 nm) imaged under RDIC. (A) Random assortment of AuNRs with different 3D orientations. (B-F) Examples of AuNRs with different in-plane orientations. Patterns range from nearly completely dark to nearly completely bright. (G-F) Examples of AuNRs with different 3D orientations. The positions of the dark and bright "lobes" are orientation dependent. All images are the sum of 20 frames exposed for 50 ms. Scale bar is 2 µm.

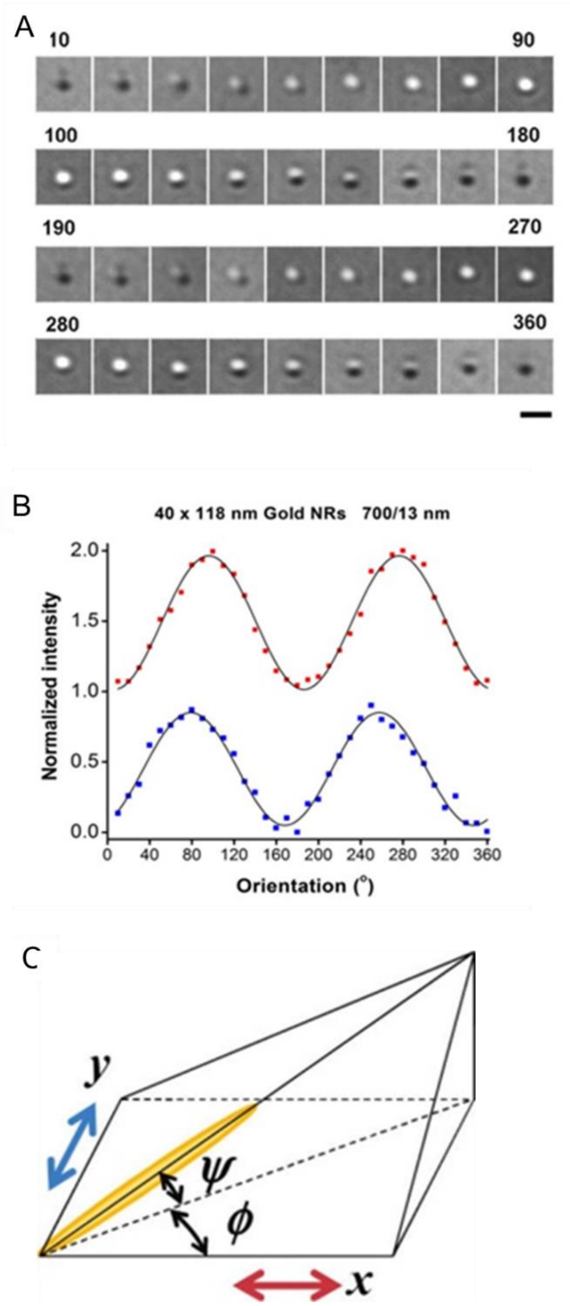

Figure 4.3. RDIC images of a gold nanorod (40x118 nm) imaged at different in-plane orientations. (A). The in-focus image patterns of the gold nanorod at different orientations relative to the optical axes. The sample slide is rotated from 10° to 360° in 10° per per step. The scale bar represents 1 μm. (B). The normalized bright part (red) and dark part intensities (blue)of the images on the top in each pair. Periodic changes of the bright/dark intensities of a gold nanorod when rotating under a DIC microscope and being illuminated at the 700 nm wavelengths. All intensities are relative to the background level. (C). Schematic illustration of a fixed dipole with polar angle ψ and azimuthal angle θ. One of the polarization direction (x-axis) may be referred to as the dark optical axis because a gold nanorod would generate a nearly all dark image when its long axis is aligned with this polarization direction; similarly, the other orthogonal polarization direction (y-axis) may be called the bright optical axis in accordance to the presentation of nearly all bright DIC image

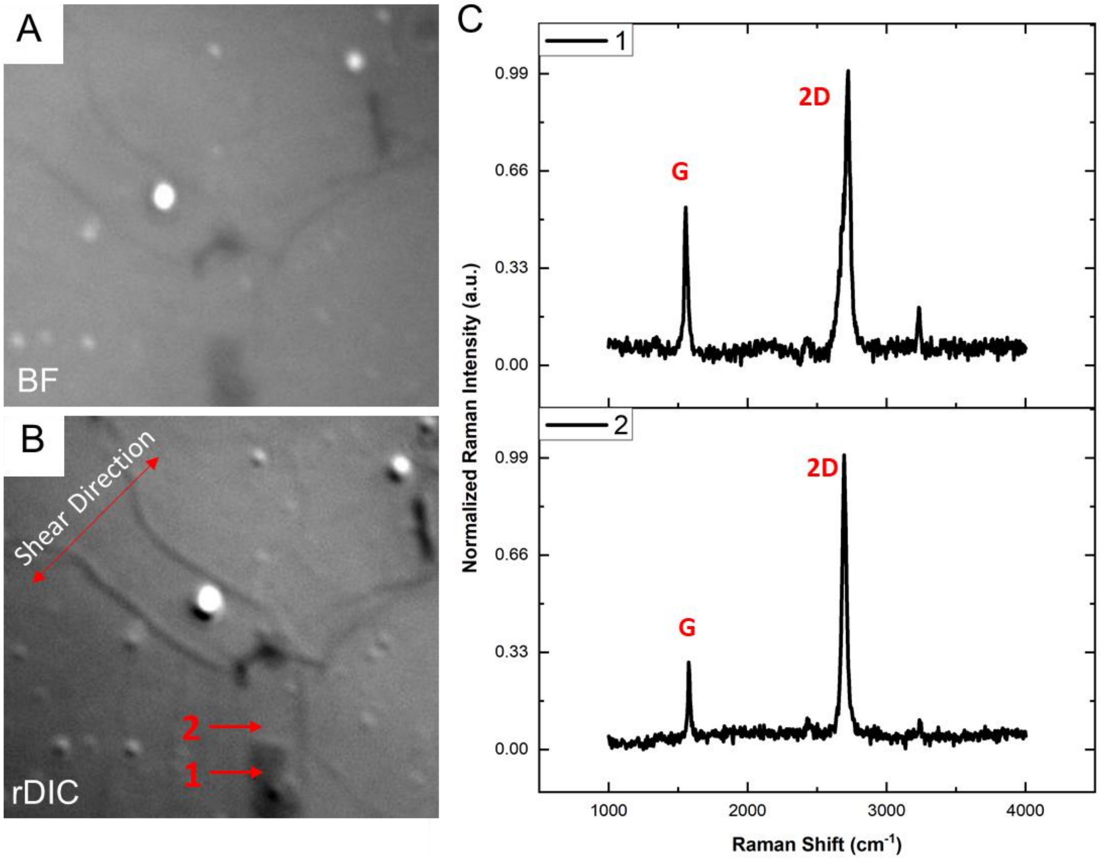

Figure 4.4. Characterization of monolayer graphene made by chemical vapor deposition. (A) Bright field microscopy image of the film on Si substrate. (B) RDIC microscopy image of the same sample area in (A) on Si substrate. The scale bar is 5 µm. (C) Raman spectra of the area 1 and 2 (pointed by the arrows) in the sample in (B).

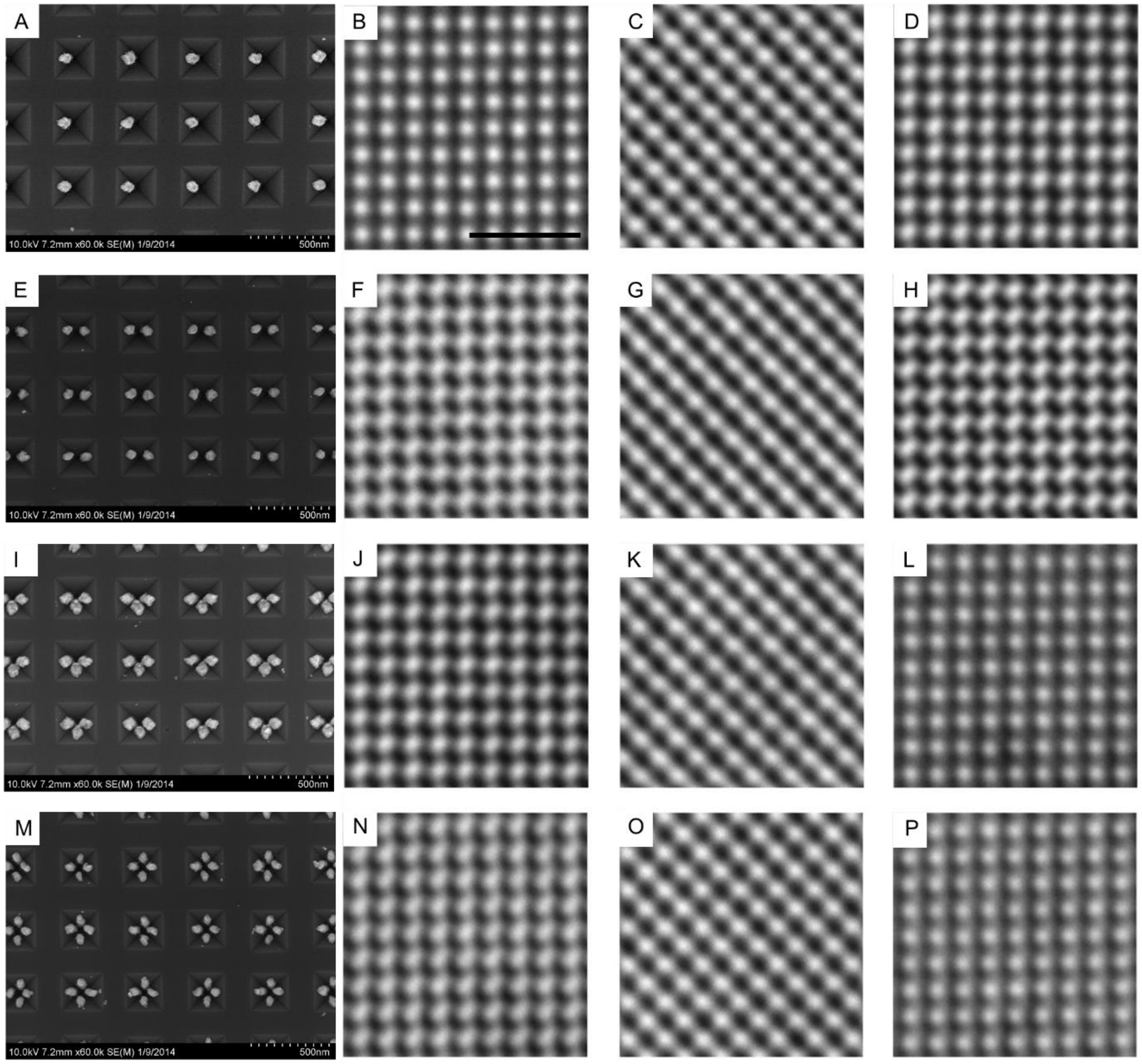

Figure 4.5. SEM and RDIC images of nanostructures fabricated in silica wafer templates at orientational angles of 0, 45 and 90 degrees. Monomers within the template (A) SEM. RDIC image with (B) 0 degrees orientation. (C) 45 degrees orientation. (D) 90 degrees orientation. Dimers within the template (E) SEM. RDIC image with (F) 0 degrees orientation. (G) 45 degrees orientation. (H) 90 degrees orientation. Trimers within the template (I) SEM. RDIC image with (J) 0 degrees orientation. (K) 45 degrees orientation. (L) 90 degrees orientation. Tetramers within the template (M) SEM. RDIC image with (N) 0 degrees orientation. (O) 45 degrees orientation. (P) 90 degrees orientation. RDIC images taken with 100 ms exposure. the scale bar of SEM images is 500 nm and RDIC images is 2 µm.

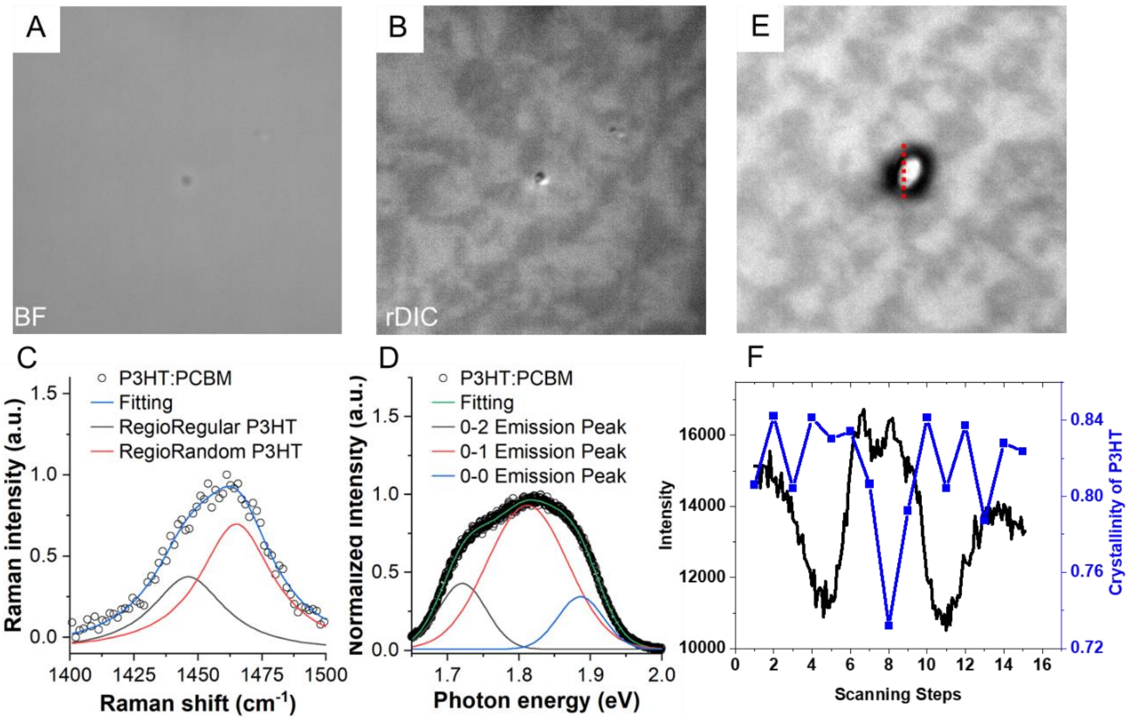

Figure 4.6. Characterization of 1:1 P3HT: PCBM blend thin film at room temperature. (A) Bright field microscopy image of the film on Si substrate. (B) RDIC microscopy image of the same film on Si substrate. The scale bar is 5 µm. (C) Raman and (D) PL spectra of the same sample in (B). (E) A PCBM crystal in P3HT matrix. (F) Image intensity and crystallinity of P3HT along the dotted red line. Each scanning step is 500 nm. The Raman and PL spectra are averaged from 10 measurements in the sample area.

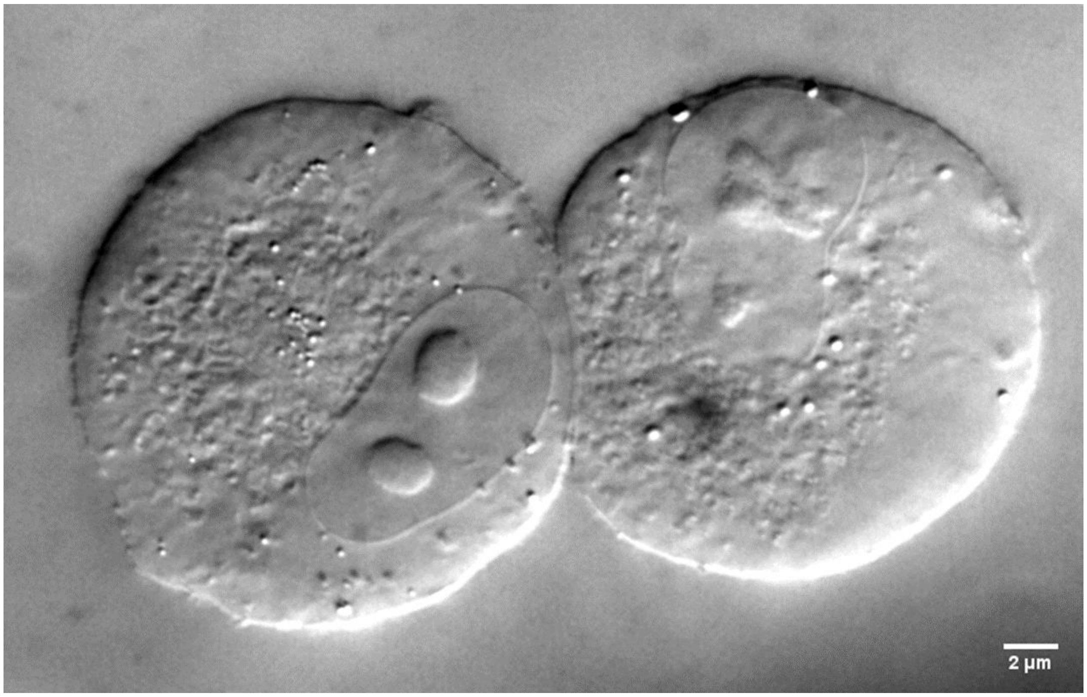

Figure 4.7. RDIC image of A549 cell samples on Si wafer.

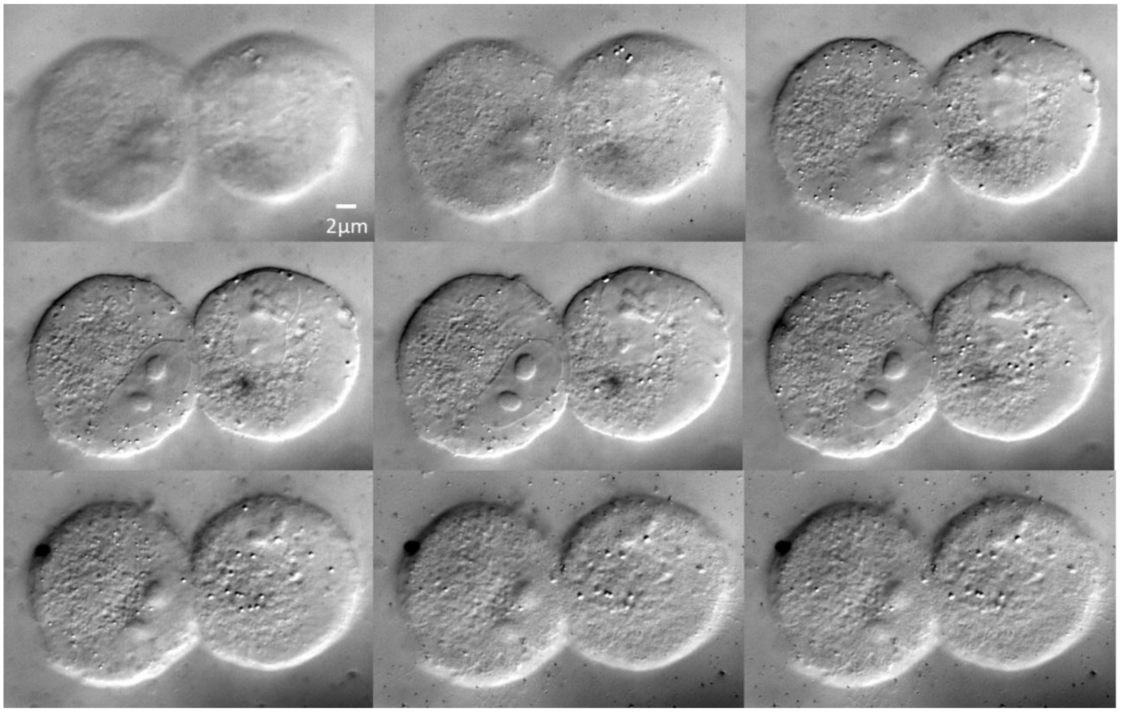

Figure 4.8. 3D scanning of A549 Cells on Si wafer.

5 LOCALIZATION ACCURACY OF GOLD NANOPARTICLES IN SINGLE PARTICLE ORIENTATION AND ROTATIONAL TRACKING

The paper is published on Optics Express, 2017, 25, 9860-9871

***FEI ZHAO,*[1] *KUANGCAI CHEN,*[1] *BIN DONG,* [1] *KAI YANG,*[2,] * *YAN GU,*[3,]* *AND NING FANG*[1,]**
1 Department of Chemistry, Georgia State University, Atlanta, Georgia, USA 30303
2 Center for Soft Condensed Matter Physics & Interdisciplinary Research, Soochow University, Suzhou, Jiangsu, China, 215006
3 The Bristol-Myers Squibb Company, Devens, Massachusetts, USA 01434
**yangkai@suda.edu.cn; yan.gu1@bms.com; nfang@gsu.edu*

5.1 Abstract

The Single Particle Orientation and Rotational Tracking (SPORT) technique, which utilizes anisotropic plasmonic gold nanorods and differential interference contrast (DIC) microscopy, has shown potential as an effective alternative to fluorescence-based techniques to decipher rotational motions on the cellular and molecular levels. However, localizing gold nanorods from their DIC images with high accuracy and precision is more challenging than the procedures applied in fluorescence or scattering microscopy techniques due to the asymmetric DIC point spread function with bright and dark parts superimposed over a grey background. In this paper, localization accuracy and inherited uncertainties from unique DIC image patterns are elucidated with the assistance of computer simulation. These discussions provide guidance for researchers to properly evaluate their data and avoid making claims beyond the technical limits. The understanding of the intrinsic localization errors and the principle of DIC microscopy leads us to propose a new localization strategy that utilizes the experimentally-measured shear distance of the DIC microscope to improve the localization accuracy.

5.2 Introduction

Fluorescence polarization microscopy (287-289) and defocused fluorescence imaging techniques (290-293) have been widely used to acquire the dipole orientation of fluorescent molecules or quantum dots. More recently, to overcome several critical limitations of fluorescence microscopy, such as photobleaching and photoblinking, anisotropic plasmonic nanoparticles have been chosen as rotational tracking probe in differential interference contrast (DIC) microscopy (242; 294), total internal reflection scattering (TIRS) microscopy (150; 205; 295), dark field polarization microscopy (207), defocused dark field microscopy (296), and planar illumination scattering microscopy (297). These techniques have enabled the studies of rotational motions in live cells. For example, the DIC microscopy-based single particle orientation and rotational tracking (SPORT) technique (242; 294; 298) resolved rotational motions of cargos at the pause during the axonal transport (299) and drug delivery carriers on live cell membranes (284).

Localization of single molecule or nanoparticle probes with high accuracy and precision is an essential requirement in single particle tracking experiments. The concept and principle of fluorescence imaging with one-nanometer accuracy (FIONA) (300), which allows the localization of single fluorescent molecules with nanometer precision via curve fitting of the approximately Gaussian shaped point spread functions (PSF), can be applied in rotational tracking. However, localizing anisotropic imaging probes is more challenging than localizing isotropic imaging probes because the 3D orientation of anisotropic probes may give rise to low signal intensities and/or asymmetric intensity distributions, which could result in significant localization errors (301-303). Efforts have also been devoted to the search of optimal PSFs as the fitting model for accurate localization of emitting dipoles. For example, a three-axis dipole PSF was found to best approximate the experimental PSF of a nanorod in Surface Enhanced Raman Scattering (SERS) microscopy (304).

A greater challenge in localization is met in the case of DIC microscopy, which has an asymmetric PSF with bright and dark parts superimposed over a grey background. This non-Gaussian PSF cannot be fitted with a simple mathematical function. Therefore, a correlation mapping algorithm has been implemented to localize isotropic particles in 2D (305) and 3D (306). However, the correlation mapping algorithm does not work properly when anisotropic plasmonic nanoparticles are imaged in SPORT experiments, because the model changes constantly as a nanorod rotates to different orientations. To overcome this challenge, we have developed a dual-channel imaging system to localize gold nanorods with high accuracy in the bright-field channel at the gold nanorod's transverse localized surface plasmon resonance (LSPR) wavelength and track the rotational motions in the DIC channel at the gold nanorod's longitudinal LSPR wavelength (307).

In the present study, we attempt to further address the challenges of superlocalization in DIC microscopy with the assistance of computer simulation. The intrinsic localization errors caused by the DIC imaging principle are quantified from both theoretical and experimental images of gold nanorods. Based on this quantitative understanding, a new localization strategy is proposed to improve the localization accuracy of gold nanorods in SPORT experiments.

5.3 Experimental Section

5.3.1 Sample Slide Preparation

The 25 nm × 73 nm gold nanorod and 80 nm gold nanosphere colloidal solutions were purchased from Nanopartz (Loveland, CO). To prepare the sample solutions, 0.1 mL of colloidal gold underwent centrifugation for 10 min at 5500 rpm, followed by removal of the liquid layer and resuspension in 0.1 mL of 18.2 MΩ Milli-Q water. The solution was diluted to a concentration of 1 × 1010 nanoparticles/mL 10 μL of the diluted solution was spin-casted onto a pre-cleaned microscope slide and covered by a glass coverslip. To prevent evaporation, the coverslip was sealed by clear nail polish. The sample slide was then placed on the microscope stage for imaging.

5.3.2 Instrumentation

An upright Nikon Eclipse 80i microscope and a Nikon Ti-E inverted microscope were used in the imaging experiments. These microscopes were equipped with a Nikon 1.40 numerical aperture (NA) oil-immersion condenser. Two objectives, a Nikon 100× 1.40 NA Plan Apo VC oil-immersion objective and a 100× 1.49 NA Apo TIRF oil-immersion objective, were used for comparison. A 540 nm or 700-nm band-pass filter (Semrock, Rochester, NY) with a bandwidth of 20 nm was inserted at the illumination side. A rotary stage was installed on the microscope for taking images of gold nanorods positioned in different orientations. At each angle, a vertical scan was done to help find the focal plane. Two scientific CMOS cameras were used to capture the DIC images: a Hamamatsu C11440-22CU, ORCA-Flash 4.0 V2 with a 2048 × 2048 pixel array and a pixel size of 6.5 μm × 6.5 μm and a Tucsen Dhyana 95 with a 2048 × 2048 pixel array and a pixel size of 11 μm × 11 μm. These cameras performed similarly in our experiments. Finally, the images were analyzed using MATLAB and NIH ImageJ (308).

5.3.3 Computer Simulation of DIC PSFs

The scattering PSFs of dipoles in different orientations were generated by a Python script modified from a published program (302). These PSFs were then used as inputs for the DIC PSF simulation program, which was written in MATLAB and is available upon request.

The core of the DIC PSF simulation is the principle of interferometry for DIC microscopy. For the Nomarski-type DIC microscope used in our experiments, the specimen is illuminated with a plane-polarized beam split into two orthogonally polarized and mutually coherent components by the first Nomarski prism. The two components are recombined into a single beam by the second Nomarski prism and interfere with each other after the analyzer to form an image. The DIC microscope converts the phase variations caused by the specimen to intensity variations. The image is formed from the two waves that are phase-shifted to different extents and laterally shifted by a shear 2Δx along the x-axis and 2Δy along the y-axis. The 2D DIC PSF is thus derived from the interference of the PSF of the two phase-shifted waves with a bias retardation 2Δθ (expressed in radians) and the lateral shear 2Δx and 2Δy (309):

$$h(x,y) = (1-R)\, exp\ (-j\Delta\theta)\, p(x+\Delta x, y+\Delta y)\ - Rexp\ (j\Delta\theta)\, p(x-\Delta x, y-\Delta y) \qquad (1)$$

where p(x, y) is the scattering amplitude PSF for transmitted-light optics under coherent illumination, and R is the amplitude ratio, defined as the amplitude of one wave field divided by the sum of the amplitudes of the two wave fields. Δx and Δy are equal in all commercial DIC microscopes, including the Nikon microscopes used in our experiments. Eq.1 was implemented in a MATLAB program, which was used to generate the simulated DIC images in this paper.

5.3.4 Shear Distance Measurement

The two intermediate images of 80-nm nanospheres were taken separately by setting the polarization direction of the second polarizer to +45° or -45° with respect to the polarization direction of the first polarizer. These polarizer settings block one of the two laterally separated beams. Then the two images were fitted with 2D Gaussian functions in MATLAB to obtain the centroid coordinates of each image. It should be noted that the intermediate images are essentially in the bright field mode; therefore, the typical scattering PSFs or Gaussian functions as a close approximation can be used to fit the images to find the centroid coordinates.

5.3.5 Gold Nanorod Localization-Weighing Algorithm

The DIC image pattern of a single gold nanorod consists of a bright part and a dark part over a grey background. As the first step of localization, a square is defined to cover the entire DIC image pattern. Within the square, the bright (or dark) part of the image can be identified by comparing the intensity of each pixel to the bright (or dark) intensity threshold, which is defined as the highest (or lowest) intensity value of the local background. Then the centroid coordinates of the bright part and the dark part of the DIC image are computed separately by weighing all of the pixels that have been identified as either bright or dark:

$$\begin{aligned} x &= \frac{\sum_i \sum_j \left(x_i \, | I_{i,j} - Threshold \,| \right)}{\sum_i \sum_j | I_{i,j} - Threshold \,|} \\ y &= \frac{\sum_i \sum_j \left(y_i \, | I_{i,j} - Threshold \,| \right)}{\sum_i \sum_j | I_{i,j} - Threshold \,|} \end{aligned} \tag{2}$$

Note that the pixels fall in the bright (or dark) part are used only in the calculation of the bright (or dark) centroid coordinates. Finally, the centroid coordinates of the simulated or experimental DIC images are obtained at the midpoint of the bright and dark centroids.

5.4 Results and Discussion

5.4.1 Localization Uncertainty for Inclined Gold Nanorods

As a simplified case within the framework of classical electrodynamics, anisotropic gold nanorods are deemed as ideal electric dipoles scattering radiation. The polar angle ψ and azimuthal angle θ of an inclined dipole (Fig. 5.1(a)) are defined based on the two polarization directions determined by the configuration of the polarizers and Nomarski prisms in the DIC microscope. Gold nanorods are imaged at their longitudinal LSPR wavelength and exhibit nearly all bright, nearly all dark, or half bright – half dark image patterns depending on their orientations. A set of samples DIC images of a gold nanorod with a fixed polar angle of 90° (lying flat on the surface) and varying azimuthal angles are shown in Fig. 5.1(b).

To understand how a dipole's orientation affects its localization in DIC microscopy, we first take into account the errors that already exist in the localization based on the scattering PSF from a dipole tilted relative to the horizontal plane. The errors in localization are associated with both the azimuthal and polar angles of the dipole. The simulated elliptical-shaped amplitude scattering PSFs of inclined dipoles with various polar and azimuthal angles (images not shown) were generated with a Python script modified from a published program (302), and they were used as inputs for the DIC simulation program (294; 309). The deviation of the coordinates of the brightest spot from the center coordinates of the dipole brings about the intrinsic localization errors (310). Lower signal intensities associated with smaller polar angles also lead to localization errors (311).

Conventional single particle localization methods rely on curve fitting of fluorescence or scattering images. 2D Gaussian functions are often used as an approximate model to fit the emission/scattering PSF. However, the DIC PSF cannot be fitted by Gaussian functions due to the shadowcast half-bright and half-dark images resulted from interference. Moreover, a lateral shear between the bright part and the dark part of a DIC image further complicates the localization. In our previous SPORT studies, localization was done by assuming a round-shaped DIC image and simply looking for the image center. The simplified method was adequate for the previous works where superlocalization was not necessary or the DIC image patterns were kept relatively constant within short time periods (242; 299).

It should be noted that the present study focuses on the cases with the polar angles ranging from 45° to 90°, which are more commonly observed in tracking nanorods on cell membranes or functionalized surfaces. Outside of this polar angle range, the nanorods are tilted to an even larger degree relative to the horizontal plane and give rise to the donut-shaped scattering PSFs (301), which complicates the DIC image patterns (312) and requires further development of computer simulation.

5.4.2 Lateral Shear of DIC Microscope

Quantitative characterization of the DIC image patterns, which is essential to improve the accuracy and precision in localizing gold nanorods in SPORT, requires the knowledge of DIC optical components. In principle, DIC microscope is one particular kind of shearing interference optical system (313). Illumination light is separated into two mutually orthogonally polarized plane light and laterally sheared by the birefringent (Nomarski or Wollaston) prisms because of the different refractive indices of the ordinary ray and extraordinary ray.

Lateral shear has significant effects on contrast, resolution, sensitivity, optical sectioning depth, and localization accuracy and precision (313). The shear distance is determined primarily by the geometry of the prisms, the wavelength of the incident light, and the focal distance of the optics (314; 315). Therefore, it is required to experimentally measure the shear distance for a given microscope configuration.

Several methods have been developed to measure the shear distance (307; 316-318). In the present work, the lateral shear distances of two commercial Nomarski prisms (Nikon standard/high-contrast prisms (Part # 100XI) and high-resolution prisms (Part # 100XI-R)) were measured by using the modified bright-field method described in our previous work (307). This procedure is illustrated in Fig. 5.2.

Table 1 lists the measured shear distances for various combinations of the type of Nomarski prism, microscope objective's numerical aperture (NA), and illumination wavelength (540 or 700 nm). At least 10 measurements were carried out for each configuration. As predicted by the theory, longer wavelength and larger NA correspond to shorter shear distance and smaller shear angle. For example, the measured shear distance with the standard Nomarski prisms at 700 nm is ~7.5% smaller than that at 540 nm.

5.4.3 Experimental and Simulated DIC Images

The simulated DIC images of gold nanospheres and nanorods with different shear distances are shown together with their corresponding experimental DIC images (Fig. 5.3). As expected, the images obtained with the high-resolution Nomarski prisms (100XI-R), which results in a smaller shear distance, are stretched to a less extent along the shear direction and the bright part and the dark part are positioned closer when compared to the images obtained using the standard Nomarski prisms (100XI).

Localization errors in DIC microscopy should be assessed based on the corresponding shear distance measured for a specific configuration. The discussion in this section will be focused on the results acquired with the following parameters: the high-resolution Nomarski prisms (100XI-R), 100x oil-immersion NA 1.40 objective, and illumination wavelength of 700 nm.

We first investigate the experimental and simulated DIC images of a gold nanorod with a fixed polar angle of 90° (flat on the surface) and varying azimuthal angles (Fig. 5.1). The cylindrical shape of a gold nanorod with a two-fold symmetry suggests a challenge in differentiating the supplementary azimuthal angles of θ and 180°-θ. Indeed, the experimental results published previously showed nearly identical bright and dark DIC image intensities and patterns at any pair of supplementary azimuthal angles. However, the simulated results presented here suggest the DIC image patterns at the supplementary azimuthal angles (except for 0° and 180°) are not identical. For example, the dark lobe in the simulated DIC image at 45° is nearly vertical, where the dark lobe in the simulated image at 135° is nearly horizontal (Fig. 5.1(d)). These differences stem from the oval-shaped scattering PSFs, which are used as the input for the DIC simulation program. These differences are also visible in the experimental DIC images (Fig. 5.1(b)), suggesting an additional element of uncertainty in localization. Furthermore, the experimental DIC intensity traces (Fig. 5.1(c)) show a broader valley at ~90° compared to the simulated traces (Fig. 5.1(e)). These differences can be attributed to the noise in the real images, the approximation of the theoretical equations used in simulation, the limit in imaging resolution, and the actual morphology of the gold nanorods that have not been taken into account in the theoretical simulations, for example, the rod's end-cap geometry affects the longitudinal surface plasmon band in real cases.

5.4.4 Improving Localization Accuracy with Measured Shear Distance

Based on the understanding of orientation-dependent DIC image patterns, we have developed an improved localization strategy, which takes the lateral shear between the bright part and dark part of the DIC images into considerations.

The initial step of the new strategy is to examine the DIC image patterns. When both the bright and dark parts of a DIC image have sufficiently high signal to noise ratio (S/N) (azimuthal angle θ near 45° or 135°), the weighing algorithm is applied to find the centroid coordinates of both the bright and dark parts and then take their midpoint as the centroid coordinates of the gold nanorod (see Experimental Section for details). On the other hand, when a DIC image is dominated by either a bright or dark part (azimuthal angle θ near 0°, 90° or 180°), the centroid coordinates of this dominant part can be easily found with the weighing algorithm; however, the S/N of the other half of the image becomes too low to warrant sufficient localization accuracy and precision. In such cases, we should discard the localization information from the weak part of the image and take the following more accurate measurement: shifting the centroid coordinates of the dominant part by half of the shear distance in both x and y. Specifically, for the DIC microscope used in our experiments, the final centroid coordinates are calculated as the weighed bright center (for a DIC image dominated by the bright part) minus half of the shear distance or the weighed dark center (for a DIC image dominated by the dark part) plus half of the shear distance.

The improved localization accuracy offered by the new localization strategy is demonstrated in Fig. 5.4(a) for gold nanorods lying flat on the surface (polar angle $\psi = 90°$). Even though both the bright and dark centroid positions determined by the weighing method are clearly influenced by the azimuthal angles, the new strategy provide rather consistent accuracy for the entire angle range (0-180°). The collective standard deviations of both the x and y centroid coordinates for all azimuthal angles are ~7 nm.

For inclined gold nanorods (polar angle $\psi < 90°$), as the polar angle gets smaller, the decreasing DIC image contrasts and increasing complexity in image patterns result in larger localization errors. The localization results gold nanorods with polar angles of 75°, 60°, and 45° (images not shown) are displayed in Fig. 5.5. At the polar angle of 45°, variations in the determined centroid coordinates (Fig. 5.5(c)) are much more significant than the other two polar angles because of the much larger uncertainties in the weighing algorithm to find the centroid coordinates of the bright and dark parts.

5.4.5 Localization Accuracy and Precision in Real DIC Images

The new localization strategy has also been tested experimentally by measuring the distance between two neighboring gold nanorods during a 360° in-plane rotation (Fig. 5.6). The DIC image patterns of these spin-casted gold nanorods suggest that they are nearly perfectly flat on the surface ($\psi \sim 90°$), and the angle between their long axes is estimated to be ~ 50° from their

DIC intensities. From the 72 measurements during the 360° rotation (in 5° steps), the standard deviation of the distance calculated between the two nanorods is 53.6 nm. Using particle 1 as the reference with the coordinates set at (0, 0), the positions of particle 2 are shown in Fig. 5.6(c). Rather consistent localization accuracy is demonstrated in nearly the entire 360°. The deviation of the distance of particle 2 relative to particle 1 from the average distance is the largest when the link between the two particles is oriented at around 25°, 95°, 200°, and 280°. A close examination of the DIC images (Fig. 5.6(a)) shows that at these angles the two particles display opposite image patterns: a dominantly bright image and a dominantly dark image. Because the largest localization errors are associated with these image patterns, the errors in the measured distances are also the largest.

5.5 Conclusions

In summary, we have studied the localization accuracy of gold nanorods in DIC microscopy imaging. The inherited localization errors from the asymmetric scattering PSF of a tilted dipole and the unique DIC patterns of gold nanorods with various polar angles and azimuthal angles have been discussed based on computer simulated DIC images. The localization accuracy in real examples of DIC microscopy imaging has also been demonstrated by measuring the distance between two neighboring gold nanorods at various orientations. These discussions provide guidance for researchers to properly evaluate their data and avoid making claims outside the technical limits. The dependence of localization accuracy on the instrument-specific lateral shear adds an additional layer of complexity to SPORT in DIC microscopy, compared to the fluorescence or dark field microscopy-based methods. A refined localization strategy has been proposed to use the experimentally measured shear distance to compensate for the localization errors.

Future efforts will be required to deal with even more complicated DIC images from highly inclined gold nanorods (polar angle $\psi < 45°$). Furthermore, sacrificed image contrast as a trade-off for faster temporal resolution can significantly impact the ability of the SPORT technique to resolve rapid rotational motions in complex environments. Just like in all fluorescence or scattering-based SPT experiments, the desires of higher sensitivity, faster imaging rate, better spatial and angular resolution, and robust automation will continue to drive the technical development and enable novel single-molecule/nanoparticle based studies.

Funding

The work was supported by the National Institution of Health (R01GM115763).

5.6 Figures

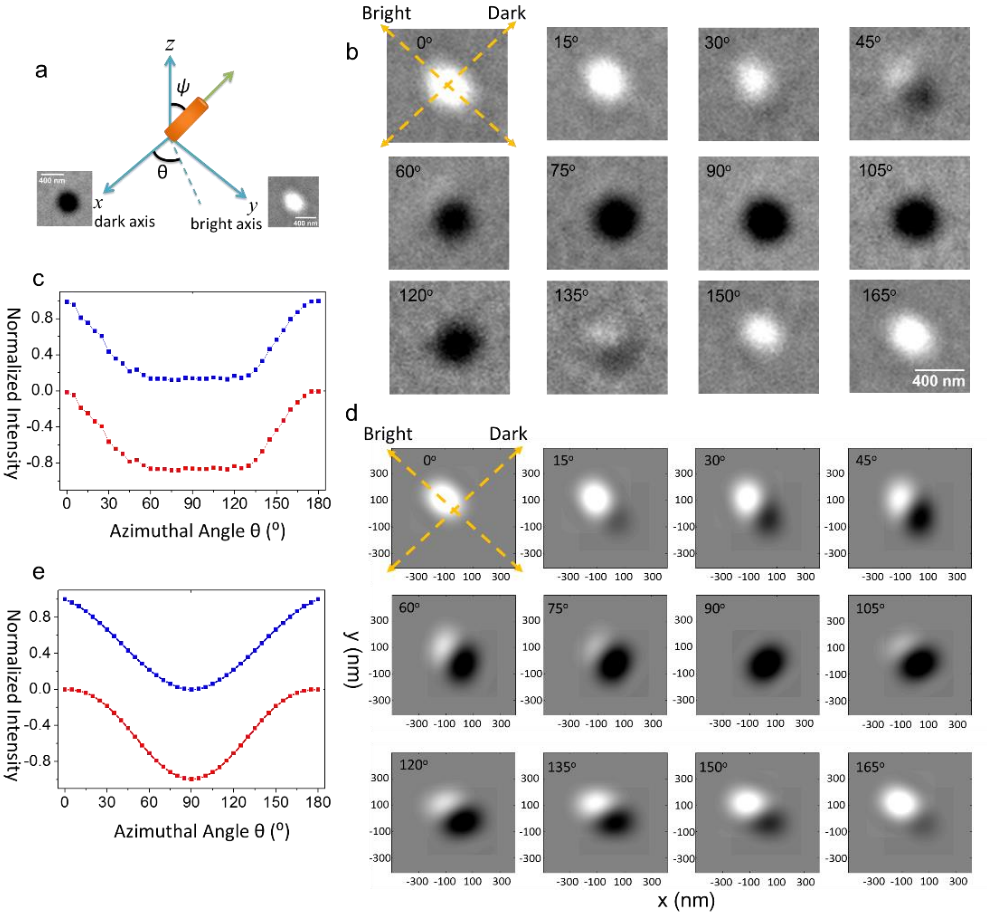

Figure 5.1 (a) Schematic illustration of a fixed dipole with polar angle ψ and azimuthal angle θ. One of the polarization direction (x-axis) may be referred to as the dark optical axis because a gold nanorod would generate a nearly all dark image when its long axis is aligned with this polarization direction; similarly, the other orthogonal polarization direction (y-axis) may be called the bright optical axis in accordance to the presentation of nearly all bright DIC image. These definitions of optical axes are used consistently in all the experimental and simulated images of gold nanorods in this study. (b) Experimental DIC images of a gold nanorod with the azimuthal angles from 0° to 180° in 15° steps. Note that 0° and 180° are equivalent due to the symmetry. (c) The corresponding bright-part intensity (blue) and dark-part intensity (red) traces for the experimental DIC images in b. (d) Computer simulated DIC images of a gold nanorod with a polar angle of 90° and azimuthal angles from 0° to 180° in 15° steps. (e) The corresponding bright-part intensity (blue) and dark-part intensity (red) traces for the simulated DIC images in d.

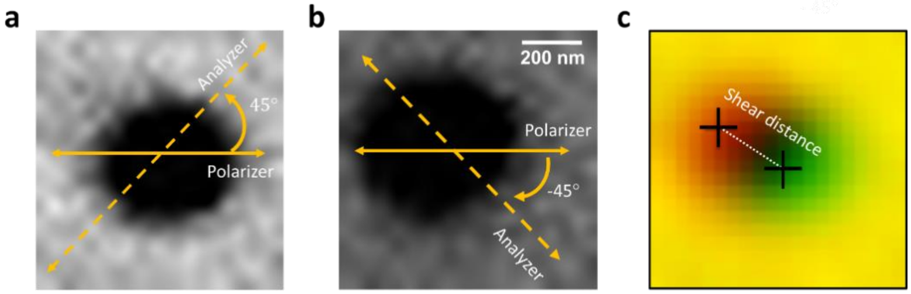

Figure 5.2 Two intermediate bright-field images of an 80-nm gold nanosphere obtained when the angle between the first and second polarizer is (a) 45° and (b) -45°. (c) The merged image. The two crosses are the centers of the two intermediate bright-field images (a) and (b) by fitting with 2D Gaussian functions. The distance between the two centers is the shear distance. The shear direction is from northwest to southeast, which is indicated by the relative positions of the two centers.

Table 1. Shear distances for different configurations.

DIC Prism Type	Shear Distance (nm)			
	Objective: Apo TIRF 100x Oil NA 1.49		Plan Apo VC 100x Oil NA 1.40	
	Wavelength: 540 nm	700 nm	540 nm	700 nm
Nikon 100XI	**246 ± 7**	**227 ± 16**	**290 ± 3**	**268 ± 20**
Nikon 100XI-R	**145 ± 18**	**134 ± 19**	**189 ± 3**	**175 ± 33**

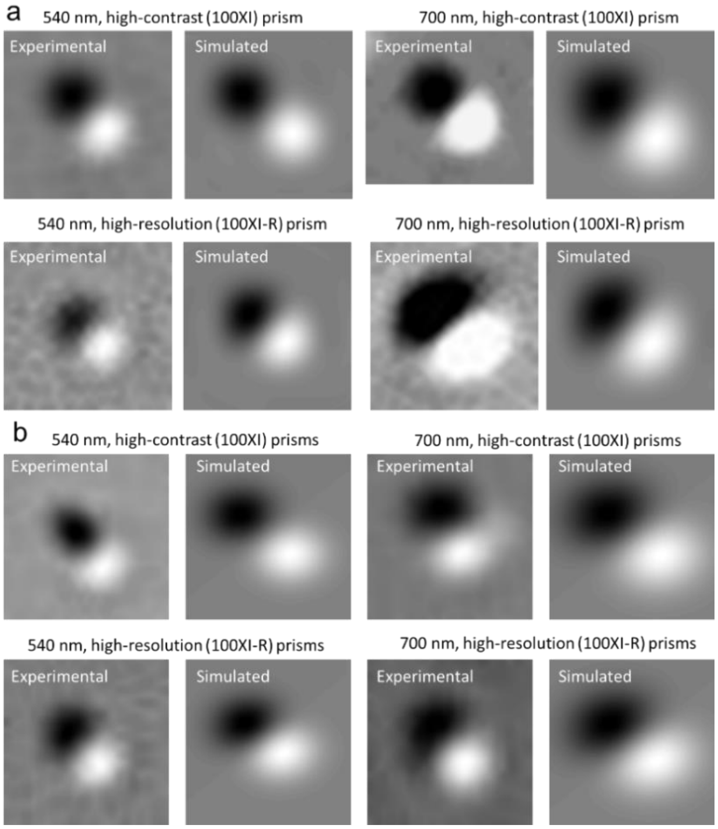

Figure 5.3 Experimental and simulated DIC images of (a) a 40 nm × 118 nm gold nanorod (90° polar angle and 45° azimuthal angle) and (b) an 80-nm gold nanosphere under 540 or 700 nm incident light with either Nikon standard/high-contrast (100XI) or high-resolution (100XI-R) prisms.

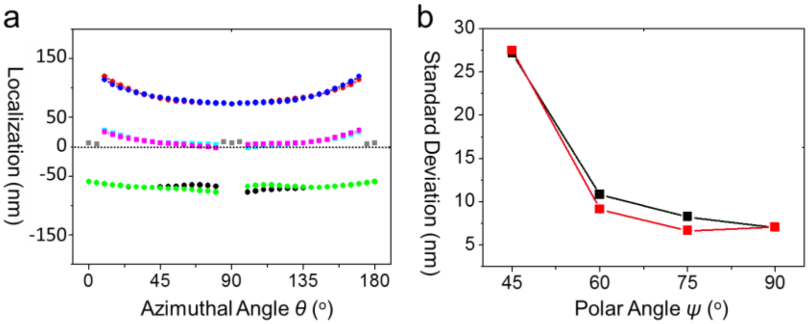

Figure 5.4 (a) Localization of the simulated gold nanorod images with a constant polar angle of 90˚ and various azimuthal angles. Red and blue: the x and y coordinates of the weighed centers of the bright part. Black and green: the x and y coordinates of the weighed centers of the dark part. Cyan and magenta: the x and y coordinates of the midpoint between the weighed centers of the bright part and dark part. Grey and yellow: the x and y centroid coordinates of the gold nanorod when either bright or dark part dominates. Yellow squares are hardly visible in the figure because they are closely overlapped with grey squares. (b) Standard deviations of the localized x (black) and y (red) coordinates of gold nanorods at four polar angles: 45˚, 60˚, 75˚and 90˚. Each data point is calculated from the simulated images with various azimuthal angles from 0-180˚, in 5˚ step size. The localization is determined from the weighed centers of the bright part and the dark part of the images.

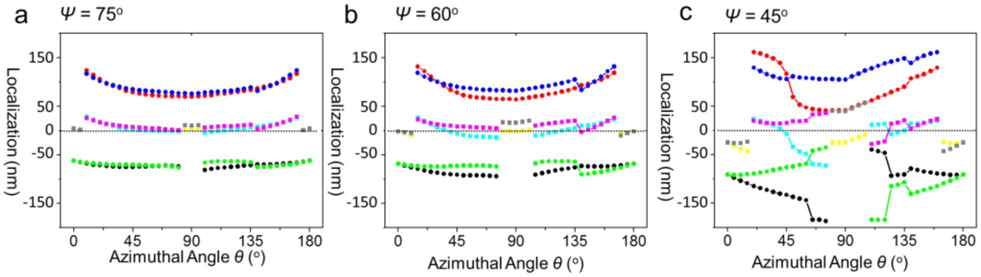

Figure 5.5 Localization of the simulated gold nanorod images with constant polar angles at 75° (a), 60° (b) and 45° (c) and with various azimuthal angles. Red and blue: the x and y coordinates of the weighed center of the bright part. Black and green: the x and y coordinates of the weighed center of the dark part. Cyan and magenta: the x and y coordinates of the midpoint between the weighed centers of the bright part and dark part. Grey and yellow: the x and y centroid coordinates of the gold nanorod when either the bright or dark part dominates; they are calculated as the weighed bright center minus half of the shear distance or the weighed dark center plus half of the shear distance.

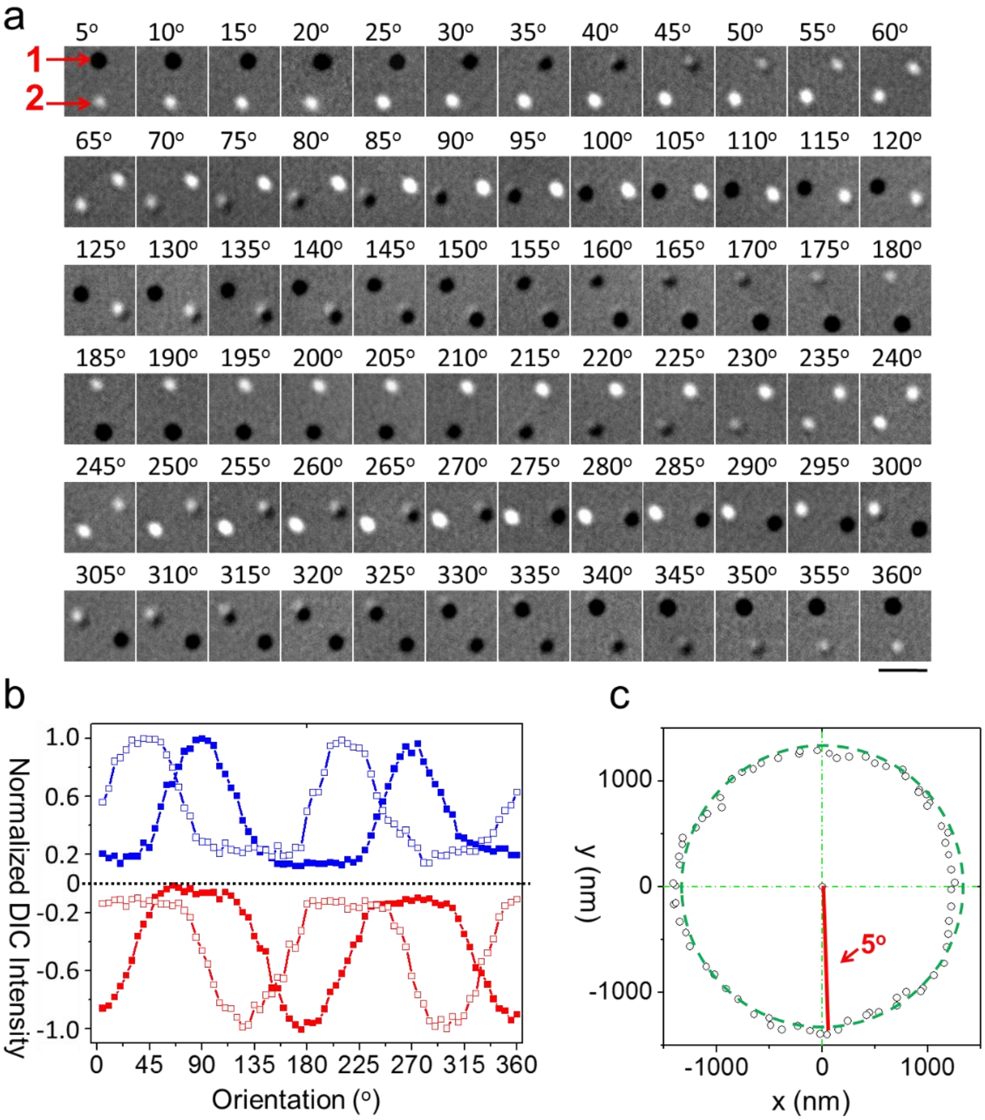

Figure 5.6 (a). The DIC images of two neighboring gold nanorods (labeled with 1 and 2) during 360° in-plane rotation. The scale bar represents 2 µm. (b) The bright (blue) and dark (red) DIC intensity traces of particle 1 (solid square) and 2 (hollow square) during the 360° in-plane rotation. (c) Localization of particle 2 relative to the position of particle 1. The radius of the green circle indicates the average distance between these two particles.

6 OVERALL CONCLUSIONS

Optical microscopy imaging has been playing an increasingly important role in the investigations of nano- and bio-materials and fundamental chemical processes. Spectroscopic measurements as companion tools can add valuable chemical and/or structural information as a new dimension of information to samples' optical microscopy images.

In this dissertation, a multi-modality spectro-microscopic system that combines far-field interferometry based optical microscopy imaging techniques (differential interference contrast microscopy and cross-polarized light microscopy), total internal reflection microscopy (total internal reflection fluorescence and scattering microscopy) and confocal spectroscopy (Raman spectroscopy and photoluminescence spectroscopy) is developed and provides multiscale in situ optical characterization with sub-diffraction-limited spatial resolution and millisecond temporal resolution. Home-built post treatment stages (thermal annealing stage and solvent annealing stage) are integrated into the system to realize in situ measurements for different material and biological samples.

Departing from conventional characterization methods in materials science mostly focused on structures on one length scale, the in situ multi-modality spectro-microscopy system aims to uncover the structural information from the molecular level to the mesoscale. Applications on photoactive layers of bulk heterojunction solar cell, two-dimensional materials, gold nanoparticles fabricated gold nanoparticle array and cells samples of the system are shown in this dissertation.

Resulting from the working principle of interference, DIC images of nanoparticles show bright and dark patterns, which precludes the 2D Gaussian fitting methods in the study of localization of nanoparticles. The last project (chapter 5) studies localization accuracy of gold nanoparticles in single particle orientation and rotational tracking under DIC microscope. This study provides guidance for researchers to properly evaluate their data and avoid making claims beyond the technical limits. The understanding of the intrinsic localization errors and the principle of DIC microscopy leads us to propose a new localization strategy that utilizes the experimentally-measured shear distance of the DIC microscope to improve the localization accuracy.

REFERENCES

1. Wayne RO. 2008. *Light and Video Microscopy*. Acadimic Press
2. Sun W, Wang G, Fang N, Yeung ES. 2009. Wavelength-Dependent Differential Interference Contrast Microscopy: Selectively Imaging Nanoparticle Probes in Live Cells. *Anal. Chem.* 81:9203-8
3. Luo Y, Sun W, Gu Y, Wang G, Fang N. 2010. Wavelength-Dependent Differential Interference Contrast Microscopy: Multiplexing Detection Using Nonfluorescent Nanoparticles. *Anal. Chem.* 82:6675-9
4. Wang G, Stender AS, Sun W, Fang N. 2010. Optical imaging of non-fluorescent nanoparticle probes in live cells. *Analyst* 135:215-21
5. Shimizu H, Mawatari K, Kitamori T. 2009. Development of a Differential Interference Contrast Thermal Lens Microscope for Sensitive Individual Nanoparticle Detection in Liquid. *Anal. Chem.* 81:9802-6
6. Luo Y, Sun W, Gu Y, Wang G, Fang N. 2010. Wavelength-Dependent Differential Interference Contrast Microscopy: Multiplexing Detection Using Nonfluorescent Nanoparticles. *Anal. Chem.* 82:6675–9
7. Asher SA, Munro CH. 1997. UV lasers revolutionize Raman spectroscopy. *Laser Focus World* 33:99
8. Wang G, Sun W, Luo Y, Fang N. 2010. Resolving rotational motions of nano-objects in engineered environments and live cells with gold nanorods and differential interference contrast microscopy. *J Am Chem Soc* 132:16417-22
9. Gu Y, Sun W, Wang G, Fang N. 2011. Single particle orientation and rotation tracking discloses distinctive rotational dynamics of drug delivery vectors on live cell membranes. *J Am Chem Soc* 133:5720-3
10. Gu Y, Sun W, Wang G, Jeftinija K, Jeftinija S, Fang N. 2012. Rotational dynamics of cargos at pauses during axonal transport. *Nat Commun* 3:1030
11. Chen K, Gu Y, Sun W, Bin D, Wang G, et al. 2017. Characteristic rotational behaviors of rod-shaped cargo revealed by automated five-dimensional single particle tracking. *Nat. Commun.* 8:887
12. Tsunoda M. 2008. Journal of microscopy. *J. Microsc.-Oxf.* 232:207-11
13. Sun W, Fang N, Trewyn BG, Tsunoda M, Slowing II, et al. 2008. Endocytosis of a single mesoporous silica nanoparticle into a human lung cancer cell observed by differential interference contrast microscopy. *Anal. Bioanal. Chem.* 391:2119
14. Zhao F, Chen K, Dong B, Yang K, Gu Y, Fang N. 2017. Localization accuracy of gold nanoparticles in single particle orientation and rotational tracking. *Opt. Express* 25:9860-71
15. Tani T, Shribak M, Oldenbourg R. 2016. Living cells and dynamic molecules observed with the polarized light microscope: the legacy of Shinya Inoue. *The Biological Bulletin* 231:85+
16. Murphy DB. Fundamentals of light microscopy and electronic imaging / Douglas B. Murphy.:xii, 368 pages :
17. Massoumian F, Juškaitis R, Neil MAA, Wilson T. 2003. Quantitative polarized light microscopy. *J. Microsc-Oxford* 209:13-22
18. Shribak M. 2015. Polychromatic polarization microscope: bringing colors to a colorless world. *Scientific Reports* 5:17340

19. Mehta SB, McQuilken M, La Riviere PJ, Occhipinti P, Verma A, et al. 2016. Dissection of molecular assembly dynamics by tracking orientation and position of single molecules in live cells. *Proc. Natl. Acad. Sci. USA* 113:E6352
20. Xu XH, Yeung ES. 1997. Direct measurement of single-molecule diffusion and photodecomposition in free solution. *Science* 275:1106-9
21. Xu XHN, Yeung ES. 1998. Long-range electrostatic trapping of single-protein molecules at a liquid-solid interface. *Science* 281:1650-3
22. He Y, Li HW, Yeung ES. 2005. Motion of single DNA molecules at a liquid-solid interface as revealed by variable-angle evanescent-field microscopy. *J. Phys. Chem. B* 109:8820-32
23. Kang SH, Shortreed MR, Yeung ES. 2001. Real-Time Dynamics of Single-DNA Molecules Undergoing Adsorption and Desorption at Liquid-Solid Interfaces. *Anal. Chem.* 73:1091-9
24. Kang SH, Yeung ES. 2002. Dynamics of single-protein molecules at a liquid/solid interface: Implications in capillary electrophoresis and chromatography. *Anal. Chem.* 74:6334-9
25. Kozuka J, Yokota H, Arai Y, Ishii Y, Yanagida T. 2006. Dynamic polymorphism of single actin molecules in the actin filament. *Nat. Chem. Biol.* 2:83-6
26. Forkey JN, Quinlan ME, Goldman YE. 2005. Measurement of Single Macromolecule Orientation by Total Internal Reflection Fluorescence Polarization Microscopy. *Biophys. J.* 89:1261-71
27. Osborne MA. 2005. Real-Time Dipole Orientational Imaging as a Probe of Ligand−Protein Interactions. *J. Phys. Chem. B* 109:18153-61
28. Bowser DN, Khakh BS. 2007. Two forms of single-vesicle astrocyte exocytosis imaged with total internal reflection fluorescence microscopy. *Proc. Natl. Acad. Sci. USA* 104:4212
29. Fix M, Melia TJ, Jaiswal JK, Rappoport JZ, You D, et al. 2004. Imaging single membrane fusion events mediated by SNARE proteins. *Proc. Natl. Acad. Sci. USA* 101:7311
30. Jaiswal JK, Simon SM. 2007. Imaging single events at the cell membrane. *Nat. Chem. Biol.* 3:92-8
31. Axelrod D. 2008. Chapter 7 Total Internal Reflection Fluorescence Microscopy. In *Methods in Cell Biology*, 89:169-221: Academic Press. Number of 169-221 pp.
32. Tang Y, Zeng X, Liang J. 2010. Surface Plasmon Resonance: An Introduction to a Surface Spectroscopy Technique. *Journal of chemical education* 87:742-6
33. Johansen K, Arwin H, Lundström I, Liedberg B. 2000. Imaging surface plasmon resonance sensor based on multiple wavelengths: Sensitivity considerations. *Review of Scientific Instruments* 71:3530-8
34. Golosovsky M, Lirtsman V, Yashunsky V, Davidov D, Aroeti B. 2009. Midinfrared surface-plasmon resonance: A novel biophysical tool for studying living cells. *Journal of Applied Physics* 105:102036
35. Liu A, Peng J, Li G. 2014. Characterizing penetration depths of multi-wavelength surface plasmon resonance sensor using silica beads. *Applied Physics Letters* 104:211103
36. Omann GM, Axelrod D. 1996. Membrane-proximal calcium transients in stimulated neutrophils detected by total internal reflection fluorescence. *Biophysical Journal* 71:2885-91

37. Merrifield CJ, Feldman ME, Wan L, Almers W. 2002. Imaging actin and dynamin recruitment during invagination of single clathrin-coated pits. *Nat. Cell Biol.* 4:691-8
38. !!! INVALID CITATION !!! (95-98).
39. Loerke D, Stuhmer W, Oheim M. 2002. Quantifying axial secretory-granule motion with variable-angle evanescent-field excitation. *J. Neurosci. Methods* 119:65-73
40. Olveczky BP, Periasamy N, Verkman AS. 1997. Mapping fluorophore distributions in three dimensions by quantitative multiple angle-total internal reflection fluorescence microscopy. *Biophys. J.* 73:2836-47
41. Rohrbach A. 2000. Observing secretory granules with a multiangle evanescent wave microscope. *Biophys. J.* 78:2641-54
42. Gell C, Berndt M, Enderlein J, Diez S. 2009. TIRF microscopy evanescent field calibration using tilted fluorescent microtubules. *Journal of Microscopy-Oxford* 234:38-46
43. Garrigues S, de la Guardia M. 2013. Chapter 5 - Vibrational Spectroscopy. In *Comprehensive Analytical Chemistry*, ed. M de la Guardia, A Gonzálvez, 60:101-22: Elsevier. Number of 101-22 pp.
44. Nakamoto K. 2001. Infrared and Raman Spectra of Inorganic and Coordination Compounds. *Handbook of Vibrational Spectroscopy*
45. Lu DY, Chen J, Deng SZ, Xu NS, Zhang WH. 2011. The most powerful tool for the structural analysis of tungsten suboxide nanowires: Raman spectroscopy. *Journal of Materials Research* 23:402-8
46. Beyssac O, Goffé B, Petitet J-P, Froigneux E, Moreau M, Rouzaud J-N. 2003. On the characterization of disordered and heterogeneous carbonaceous materials by Raman spectroscopy. *Spectrochim. Acta Mol. Biomol. Spectrosc.* 59:2267-76
47. Kneipp K, Kneipp H, Itzkan I, Dasari RR, Feld MS. 1999. Ultrasensitive Chemical Analysis by Raman Spectroscopy. *Chemical Reviews* 99:2957-76
48. Lin P-C, Lin S, Wang PC, Sridhar R. 2014. Techniques for physicochemical characterization of nanomaterials. *Biotechnol. Adv.* 32:711-26
49. Popović ZV, Dohčević-Mitrović Z, Šćepanović M, Grujić-Brojčin M, Aškrabić S. 2011. Raman scattering on nanomaterials and nanostructures. *Annalen der Physik* 523:62-74
50. Puppels GJ, de Mul FFM, Otto C, Greve J, Robert-Nicoud M, et al. 1990. Studying single living cells and chromosomes by confocal Raman microspectroscopy. *Nature* 347:301
51. Hanlon EB, Manoharan R, Koo TW, Shafer KE, Motz JT, et al. 2000. Prospects for in vivo Raman spectroscopy. *Physics in Medicine & Biology* 45:R1
52. Empedocles SA, Norris DJ, Bawendi MG. 1996. Photoluminescence Spectroscopy of Single CdSe Nanocrystallite Quantum Dots. *Phys. Rev. Lett.* 77:3873-6
53. Gilliland GD. 1997. Photoluminescence spectroscopy of crystalline semiconductors. *Materials Science and Engineering: R: Reports* 18:99-399
54. Tan PH, Rozhin AG, Hasan T, Hu P, Scardaci V, et al. 2007. Photoluminescence Spectroscopy of Carbon Nanotube Bundles: Evidence for Exciton Energy Transfer. *Phys. Rev. Lett.* 99:137402
55. Kaftelen H, Ocakoglu K, Thomann R, Tu S, Weber S, Erdem E. 2012. EPR and photoluminescence spectroscopy studies on the defect structure of ZnO nanocrystals. *Phys. Rev. B* 86:014113

56. Ostapenko S, Tarasov I, Kalejs JP, Haessler C, Reisner EU. 2000. Defect monitoring using scanning photoluminescence spectroscopy in multicrystalline silicon wafers. *Semiconductor Science and Technology* 15:840-8
57. Valenta J, Juhasz R, Linnros J. 2002. Photoluminescence spectroscopy of single silicon quantum dots. *Appl. Phys. Lett.* 80:1070-2
58. !!! INVALID CITATION !!! (113-116).
59. Toparli C, Sarfraz A, Erbe A. 2015. A new look at oxide formation at the copper/electrolyte interface by in situ spectroscopies. *Phys. Chem. Chem. Phys.* 17:31670-9
60. Toparli C, Sarfraz A, Wieck AD, Rohwerder M, Erbe A. 2017. In situ and operando observation of surface oxides during oxygen evolution reaction on copper. *Electrochimica Acta* 236:104-15
61. Iqbal D, Sarfraz A, Stratmann M, Erbe A. 2015. Solvent-starved conditions in confinement cause chemical oscillations excited by passage of a cathodic delamination front. *Chem. Commun.* 51:16041-4
62. Sarfraz A, Posner R, Bashir A, Topalov A, Mayrhofer KJJ, et al. 2016. Effect of Polarisation Mimicking Cathodic Electrodeposition Coating on Industrially Relevant Metal Substrates with ZrO2-Based Conversion Coatings. *ChemElectroChem* 3:1415-21
63. Zhang D, Li C, Zhang C, Slipchenko MN, Eakins G, Cheng J-X. 2016. Depth-resolved mid-infrared photothermal imaging of living cells and organisms with submicrometer spatial resolution. *Science Advances* 2:e1600521
64. Li C, Zhang D, Slipchenko MN, Cheng J-X. 2017. Mid-Infrared Photothermal Imaging of Active Pharmaceutical Ingredients at Submicrometer Spatial Resolution. *Anal. Chem.* 89:4863-7
65. Bai Y, Zhang D, Li C, Liu C, Cheng J-X. 2017. Bond-Selective Imaging of Cells by Mid-Infrared Photothermal Microscopy in High Wavenumber Region. *J. Phys. Chem. B* 121:10249-55
66. Rocha-Mendoza I, Licea-Rodriguez J, Marro M, Olarte OE, Plata-Sanchez M, Loza-Alvarez P. 2015. Rapid spontaneous Raman light sheet microscopy using cw-lasers and tunable filters. *Biomedical Optics Express* 6:3449-61
67. Rey I, Lassègues JC, Baudry P, Majastre H. 1998. Study of a lithium battery by confocal Raman microspectrometry. *Electrochimica Acta* 43:1539-44
68. Kong K, Rowlands CJ, Varma S, Perkins W, Leach IH, et al. 2013. Diagnosis of tumors during tissue-conserving surgery with integrated autofluorescence and Raman scattering microscopy. *Proceedings of the National Academy of Sciences* 110:15189
69. Yang Y-C, Chang W-T, Huang S-K, Liau I. 2014. Characterization of the Pharmaceutical Effect of Drugs on Atherosclerotic Lesions in Vivo Using Integrated Fluorescence Imaging and Raman Spectral Measurements. *Anal. Chem.* 86:3863-8
70. Gong Z, Pan Y-L, Videen G, Wang C. 2018. Optical trapping-Raman spectroscopy (OT-RS) with embedded microscopy imaging for concurrent characterization and monitoring of physical and chemical properties of single particles. *Analytica Chimica Acta* 1020:86-94
71. Li W, Wojcik M, Xu K. 2019. Optical Microscopy Unveils Rapid, Reversible Electrochemical Oxidation and Reduction of Graphene. *Nano Letters* 19:983-9

72. Chen X, Shen Z, He Y, Guan T, He Q, et al. 2019. Dual-wavelength digital holographic phase and fluorescence microscopy combining with Raman spectroscopy for micro-quartz pieces-based dual-channel encoded suspension array. *Opt. Express* 27:1894-910
73. Li X, Zhang D, Bai Y, Wang W, Liang J, Cheng J-X. 2019. Fingerprinting a Living Cell by Raman Integrated Mid-Infrared Photothermal Microscopy. *Anal. Chem.* 91:10750-6
74. Jhan J-W, Chang W-T, Chen H-C, Lee Y-T, Wu M-F, et al. 2008. Integrated multiple multi-photon imaging and Raman spectroscopy for characterizing structure-constituent correlation of tissues. *Opt. Express* 16:16431-41
75. Novák P, Panitz JC, Joho F, Lanz M, Imhof R, Coluccia M. 2000. Advanced in situ methods for the characterization of practical electrodes in lithium-ion batteries. *Journal of Power Sources* 90:52-8
76. Bunaciu AA, Aboul-Enein HY, Fleschin Ş. 2015. Vibrational Spectroscopy in Clinical Analysis. *Applied Spectroscopy Reviews* 50:176-91
77. Dumas P, Sockalingum GD, Sulé-Suso J. 2007. Adding synchrotron radiation to infrared microspectroscopy: what's new in biomedical applications? *Trends in Biotechnology* 25:40-4
78. Carr GL, Reffner JA, Williams GP. 1995. Performance of an infrared microspectrometer at the NSLS. *Rev. Sci. Instrum.* 66:1490-2
79. Holman H-YN, Bechtel HA, Hao Z, Martin MC. 2010. Synchrotron IR Spectromicroscopy: Chemistry of Living Cells. *Analytical Chemistry* 82:8757-65
80. Williams GP. 1996. IR spectroscopy at surfaces with synchrotron radiation. *Surface Science* 368:1-8
81. Dazzi A, Prater CB. 2017. AFM-IR: Technology and Applications in Nanoscale Infrared Spectroscopy and Chemical Imaging. *Chem. Rev.* 117:5146-73
82. Huth F, Govyadinov A, Amarie S, Nuansing W, Keilmann F, Hillenbrand R. 2012. Nano-FTIR Absorption Spectroscopy of Molecular Fingerprints at 20 nm Spatial Resolution. *Nano Lett.* 12:3973-8
83. Li Z, Aleshire K, Kuno M, Hartland GV. 2017. Super-Resolution Far-Field Infrared Imaging by Photothermal Heterodyne Imaging. *J. Phys. Chem. B* 121:8838-46
84. Whelan DR, Bell TDM. 2015. Correlative Synchrotron Fourier Transform Infrared Spectroscopy and Single Molecule Super Resolution Microscopy for the Detection of Composition and Ultrastructure Alterations in Single Cells. *ACS Chemical Biology* 10:2874-83
85. Berera R, van Grondelle R, Kennis JTM. 2009. Ultrafast transient absorption spectroscopy: principles and application to photosynthetic systems. *Photosynthesis Research* 101:105-18
86. Kim Y-H, So PTC. 2017. Three-dimensional wide-field pump-probe structured illumination microscopy. *Opt. Express* 25:7369-91
87. Nechay BA, Siegner U, Achermann M, Bielefeldt H, Keller U. 1999. Femtosecond pump-probe near-field optical microscopy. *Rev. Sci. Instrum.* 70:2758-64
88. Shen Y, Lin T-C, Dai J, Markowicz P, Prasad PN. 2003. Near-Field Optical Imaging of Transient Absorption Dynamics in Organic Nanocrystals. *J. Phys. Chem. B* 107:13551-3
89. Wang P, Slipchenko MN, Mitchell J, Yang C, Potma EO, et al. 2013. Far-field imaging of non-fluorescent species with subdiffraction resolution. *Nat. Photonics* 7:449-53
90. Penwell SB, Ginsberg LDS, Noriega R, Ginsberg NS. 2017. Resolving ultrafast exciton migration in organic solids at the nanoscale. *Nat. Mater.* 16:1136-41

91. Liu N, Kumbham M, Pita I, Guo Y, Bianchini P, et al. 2016. Far-Field Subdiffraction Imaging of Semiconductors Using Nonlinear Transient Absorption Differential Microscopy. *ACS Photonics* 3:478-85
92. Miyazaki J, Kawasumi K, Kobayashi T. 2014. Resolution improvement in laser diode-based pump–probe microscopy with an annular pupil filter. *Opt. Lett.* 39:4219-22
93. Kobayashi T, Kawasumi K, Miyazaki J, Nakata K. 2018. Resolution enhancement of pump–probe microscope with an inverse-annular filter. *Optical Review* 25:271-94
94. He J, Wang N, Kobayashi T. 2016. Numerical study of super-resolved optical microscopy with partly staggered beams. *Journal of Optics* 18:125303
95. Massaro ES, Hill AH, Grumstrup EM. 2016. Super-Resolution Structured Pump–Probe Microscopy. *ACS Photonics* 3:501-6
96. Massaro ES, Hill AH, Kennedy CL, Grumstrup EM. 2016. Imaging theory of structured pump-probe microscopy. *Opt. Express* 24:20868-80
97. Yuan L, Chung T-F, Kuc A, Wan Y, Xu Y, et al. 2018. Photocarrier generation from interlayer charge-transfer transitions in WS<sub>2</sub>-graphene heterostructures. *Science Advances* 4:e1700324
98. Zhu Y, Cheng J-X. 2020. Transient absorption microscopy: Technological innovations and applications in materials science and life science. *J. Chem. Phys.* 152:020901
99. Grancini G, Biasiucci M, Mastria R, Scotognella F, Tassone F, et al. 2012. Dynamic Microscopy Study of Ultrafast Charge Transfer in a Hybrid P3HT/Hyperbranched CdSe Nanoparticle Blend for Photovoltaics. *J. Phys. Chem. Lett.* 3:517-23
100. Grancini G, Polli D, Fazzi D, Cabanillas-Gonzalez J, Cerullo G, Lanzani G. 2011. Transient Absorption Imaging of P3HT:PCBM Photovoltaic Blend: Evidence For Interfacial Charge Transfer State. *J. Phys. Chem. Lett.* 2:1099-105
101. Polli D, Grancini G, Clark J, Celebrano M, Virgili T, et al. 2010. Nanoscale Imaging of the Interface Dynamics in Polymer Blends by Femtosecond Pump-Probe Confocal Microscopy. *Adv. Mater.* 22:3048-51
102. Snaider JM, Guo Z, Wang T, Yang M, Yuan L, et al. 2018. Ultrafast Imaging of Carrier Transport across Grain Boundaries in Hybrid Perovskite Thin Films. *ACS Energy Letters* 3:1402-8
103. Wong CTO, Lo SS, Huang L. 2012. Ultrafast Spatial Imaging of Charge Dynamics in Heterogeneous Polymer Blends. *J. Phys. Chem. Lett.* 3:879-84
104. Shi H, Yan R, Bertolazzi S, Brivio J, Gao B, et al. 2013. Exciton Dynamics in Suspended Monolayer and Few-Layer MoS2 2D Crystals. *ACS Nano* 7:1072-80
105. Cui Q, Ceballos F, Kumar N, Zhao H. 2014. Transient Absorption Microscopy of Monolayer and Bulk WSe2. *ACS Nano* 8:2970-6
106. Miao X, Zhang G, Wang F, Yan H, Ji M. 2018. Layer-Dependent Ultrafast Carrier and Coherent Phonon Dynamics in Black Phosphorus. *Nano Lett.* 18:3053-9
107. Lo SS, Major TA, Petchsang N, Huang L, Kuno MK, Hartland GV. 2012. Charge Carrier Trapping and Acoustic Phonon Modes in Single CdTe Nanowires. *ACS Nano* 6:5274-82
108. Grumstrup EM, Gabriel MM, Cating EM, Pinion CW, Christesen JD, et al. 2014. Ultrafast Carrier Dynamics in Individual Silicon Nanowires: Characterization of Diameter-Dependent Carrier Lifetime and Surface Recombination with Pump–Probe Microscopy. *J. Phys. Chem. C* 118:8634-40

109. Grumstrup EM, Gabriel MM, Pinion CW, Parker JK, Cahoon JF, Papanikolas JM. 2014. Reversible Strain-Induced Electron–Hole Recombination in Silicon Nanowires Observed with Femtosecond Pump–Probe Microscopy. *Nano Lett.* 14:6287-92
110. Cating EEM, Pinion CW, Van Goethem EM, Gabriel MM, Cahoon JF, Papanikolas JM. 2016. Imaging Spatial Variations in the Dissipation and Transport of Thermal Energy within Individual Silicon Nanowires Using Ultrafast Microscopy. *Nano Lett.* 16:434-9
111. Cating EEM, Pinion CW, Christesen JD, Christie CA, Grumstrup EM, et al. 2017. Probing Intrawire, Interwire, and Diameter-Dependent Variations in Silicon Nanowire Surface Trap Density with Pump–Probe Microscopy. *Nano Lett.* 17:5956-61
112. Huang L, Hartland GV, Chu L-Q, Luxmi, Feenstra RM, et al. 2010. Ultrafast Transient Absorption Microscopy Studies of Carrier Dynamics in Epitaxial Graphene. *Nano Lett.* 10:1308-13
113. Murphy S, Huang L. 2013. Transient absorption microscopy studies of energy relaxation in graphene oxide thin film. *J. Phys. Condens. Matter* 25:144203
114. Gao B, Hartland GV, Huang L. 2012. Transient Absorption Spectroscopy and Imaging of Individual Chirality-Assigned Single-Walled Carbon Nanotubes. *ACS Nano* 6:5083-90
115. Chong S, Min W, Xie XS. 2010. Ground-State Depletion Microscopy: Detection Sensitivity of Single-Molecule Optical Absorption at Room Temperature. *J. Phys. Chem. Lett.* 1:3316-22
116. Schumacher T, Kratzer K, Molnar D, Hentschel M, Giessen H, Lippitz M. 2011. Nanoantenna-enhanced ultrafast nonlinear spectroscopy of a single gold nanoparticle. *Nat. Commun.* 2:333
117. Liu J, Irudayaraj JMK. 2016. Non-fluorescent quantification of single mRNA with transient absorption microscopy. *Nanoscale* 8:19242-8
118. Huang K-C, McCall J, Wang P, Liao C-S, Eakins G, et al. 2018. High-Speed Spectroscopic Transient Absorption Imaging of Defects in Graphene. *Nano Lett.* 18:1489-97
119. Bossi M, Fölling J, Belov VN, Boyarskiy VP, Medda R, et al. 2008. Multicolor Far-Field Fluorescence Nanoscopy through Isolated Detection of Distinct Molecular Species. *Nano Lett.* 8:2463-8
120. Testa I, Wurm CA, Medda R, Rothermel E, von Middendorf C, et al. 2010. Multicolor fluorescence nanoscopy in fixed and living cells by exciting conventional fluorophores with a single wavelength. *Biophysical journal* 99:2686-94
121. Gunewardene Mudalige S, Subach Fedor V, Gould Travis J, Penoncello Gregory P, Gudheti Manasa V, et al. 2011. Superresolution Imaging of Multiple Fluorescent Proteins with Highly Overlapping Emission Spectra in Living Cells. *Biophys. J.* 101:1522-8
122. Zhang Z, Kenny SJ, Hauser M, Li W, Xu K. 2015. Ultrahigh-throughput single-molecule spectroscopy and spectrally resolved super-resolution microscopy. *Nat. Methods* 12:935-8
123. Mlodzianoski MJ, Curthoys NM, Gunewardene MS, Carter S, Hess ST. 2016. Super-Resolution Imaging of Molecular Emission Spectra and Single Molecule Spectral Fluctuations. *PloS one* 11:e0147506-e
124. Comtet J, Glushkov E, Navikas V, Feng J, Babenko V, et al. 2019. Wide-Field Spectral Super-Resolution Mapping of Optically Active Defects in Hexagonal Boron Nitride. *Nano Lett.* 19:2516-23

125. Moon S, Yan R, Kenny SJ, Shyu Y, Xiang L, et al. 2017. Spectrally Resolved, Functional Super-Resolution Microscopy Reveals Nanoscale Compositional Heterogeneity in Live-Cell Membranes. *J. Am. Chem. Soc.* 139:10944-7
126. Dong B, Almassalha L, Urban BE, Nguyen T-Q, Khuon S, et al. 2016. Super-resolution spectroscopic microscopy via photon localization. *Nat. Commun.* 7:12290
127. Bongiovanni MN, Godet J, Horrocks MH, Tosatto L, Carr AR, et al. 2016. Multi-dimensional super-resolution imaging enables surface hydrophobicity mapping. *Nat. Commun.* 7:13544
128. Kim D, Zhang Z, Xu K. 2017. Spectrally Resolved Super-Resolution Microscopy Unveils Multipath Reaction Pathways of Single Spiropyran Molecules. *Journal of the American Chemical Society* 139:9447-50
129. Ma W, Yang C, Gong X, Lee K, Heeger AJ. 2005. Thermally Stable, Efficient Polymer Solar Cells with Nanoscale Control of the Interpenetrating Network Morphology. *Advanced Functional Materials* 15:1617-22
130. Xu Z, Chen L-M, Yang G, Huang C-H, Hou J, et al. 2009. Vertical Phase Separation in Poly(3-hexylthiophene): Fullerene Derivative Blends and its Advantage for Inverted Structure Solar Cells. *Advanced Functional Materials* 19:1227-34
131. Dang MT, Hirsch L, Wantz G. 2011. P3HT:PCBM, Best Seller in Polymer Photovoltaic Research. *Advanced Materials* 23:3597-602
132. Zhao J, Swinnen A, Van Assche G, Manca J, Vanderzande D, Mele BV. 2009. Phase Diagram of P3HT/PCBM Blends and Its Implication for the Stability of Morphology. *The Journal of Physical Chemistry B* 113:1587-91
133. Wang H, Wang H-Y, Gao B-R, Wang L, Yang Z-Y, et al. 2011. Exciton diffusion and charge transfer dynamics in nano phase-separated P3HT/PCBM blend films. *Nanoscale* 3:2280-5
134. Karagiannidis PG, Georgiou D, Pitsalidis C, Laskarakis A, Logothetidis S. 2011. Evolution of vertical phase separation in P3HT:PCBM thin films induced by thermal annealing. *Materials Chemistry and Physics* 129:1207-13
135. Baek W-H, Yoon T-S, Lee HH, Kim Y-S. 2010. Composition-dependent phase separation of P3HT:PCBM composites for high performance organic solar cells. *Organic Electronics* 11:933-7
136. Feng SS. Nanoparticles of biodegradable polymers for new-concept chemotherapy.
137. Kim T-H, Kim M, Park H-S, Shin US, Gong M-S, Kim H-W. 2012. Size-dependent cellular toxicity of silver nanoparticles. *Journal of Biomedical Materials Research Part A* 100A:1033-43
138. Sosenkova LS, Egorova EM. 2011. The effect of particle size on the toxic action of silver nanoparticles. *Journal of Physics: Conference Series* 291:012027
139. Champion JA, Katare YK, Mitragotri S. 2007. Particle shape: A new design parameter for micro- and nanoscale drug delivery carriers. *Journal of Controlled Release* 121:3-9
140. Etheridge ML, Campbell SA, Erdman AG, Haynes CL, Wolf SM, McCullough J. 2013. The big picture on nanomedicine: the state of investigational and approved nanomedicine products. *Nanomedicine: Nanotechnology, Biology and Medicine* 9:1-14
141. Briscoe CJ, Hage DS. 2009. Factors affecting the stability of drugs and drug metabolites in biological matrices. *Bioanalysis* 1:205-20

142. French RA, Jacobson AR, Kim B, Isley SL, Penn RL, Baveye PC. 2009. Influence of ionic strength, pH, and cation valence on aggregation kinetics of titanium dioxide nanoparticles. *Environmental science & technology* 43:1354-9
143. Wojcik M, Li Y, Li W, Xu K. 2017. Spatially Resolved in Situ Reaction Dynamics of Graphene via Optical Microscopy. *Journal of the American Chemical Society* 139:5836-41
144. Crabtree G, Sarrao J, Alivisatos P, Barletta W, Bates F, et al. 2012. From Quanta to the Continuum: Opportunities for Mesoscale Science, United States
145. Liu S, Zhang J, Dong R, Gordiichuk P, Zhang T, et al. 2016. Two-Dimensional Mesoscale-Ordered Conducting Polymers. *Angew. Chem. Int. Ed.* 55:12516-21
146. Ioannidou K, Krakowiak KJ, Bauchy M, Hoover CG, Masoero E, et al. 2016. Mesoscale texture of cement hydrates. *Proc. Natl. Acad. Sci. USA* 113:2029
147. Panova O, Ophus C, Takacs CJ, Bustillo KC, Balhorn L, et al. 2019. Diffraction imaging of nanocrystalline structures in organic semiconductor molecular thin films. *Nat. Mater.*
148. Lessor DL, Hartman JS, Gordon RL. 1979. QUANTITATIVE SURFACE-TOPOGRAPHY DETERMINATION BY NOMARSKI REFLECTION MICROSCOPY .1. THEORY. *Journal of the Optical Society of America* 69:357-66
149. Fang Y. 2015. Total Internal Reflection Fluorescence Quantification of Receptor Pharmacology. *Biosensors* 5:223-40
150. Ha JW, Marchuk K, Fang N. 2012. Focused orientation and position imaging (FOPI) of single anisotropic plasmonic nanoparticles by total internal reflection scattering microscopy. *Nano Lett.* 12:4282-8
151. Treat ND, Westacott P, Stingelin N. 2015. The Power of Materials Science Tools for Gaining Insights into Organic Semiconductors. *Annu. Rev. Mater. Res.* 45:459-90
152. Takacs CJ, Treat ND, Krämer S, Chen Z, Facchetti A, et al. 2013. Remarkable Order of a High-Performance Polymer. *Nano Lett.* 13:2522-7
153. Wang H, Xu Y, Yu X, Xing R, Liu J, Han Y. 2013. Structure and Morphology Control in Thin Films of Conjugated Polymers for an Improved Charge Transport. *Polymers* 5
154. Treat ND, Chabinyc ML. 2014. Phase Separation in Bulk Heterojunctions of Semiconducting Polymers and Fullerenes for Photovoltaics. *Annu. Rev. Phys. Chem.* 65:59-81
155. Salleo A, Chen TW, Völkel AR, Wu Y, Liu P, et al. 2004. Intrinsic hole mobility and trapping in a regioregular poly(thiophene). *Phys. Rev. B* 70:115311
156. Herzing AA, Richter LJ, Anderson IM. 2010. 3D Nanoscale Characterization of Thin-Film Organic Photovoltaic Device Structures via Spectroscopic Contrast in the TEM 1. *J. Phys. Chem. C* 114:17501-8
157. Noriega R, Rivnay J, Vandewal K, Koch FPV, Stingelin N, et al. 2013. A general relationship between disorder, aggregation and charge transport in conjugated polymers. *Nat. Mater.* 12:1038
158. Panzer F, Sommer M, Bässler H, Thelakkat M, Köhler A. 2015. Spectroscopic Signature of Two Distinct H-Aggregate Species in Poly(3-hexylthiophene). *Macromolecules* 48:1543-53
159. Sanyal M, Schmidt-Hansberg B, Klein MFG, Munuera C, Vorobiev A, et al. 2011. Effect of Photovoltaic Polymer/Fullerene Blend Composition Ratio on Microstructure Evolution during Film Solidification Investigated in Real Time by X-ray Diffraction. *Macromolecules* 44:3795-800

160. Miller NC, Gysel R, Miller CE, Verploegen E, Beiley Z, et al. 2011. The phase behavior of a polymer-fullerene bulk heterojunction system that contains bimolecular crystals. *Journal of Polymer Science Part B: Polymer Physics* 49:499-503
161. Verploegen E, Mondal R, Bettinger CJ, Sok S, Toney MF, Bao Z. 2010. Effects of Thermal Annealing Upon the Morphology of Polymer–Fullerene Blends. *Adv. Funct. Mater.* 20:3519-29
162. Gao J, Thomas AK, Johnson R, Guo H, Grey JK. 2014. Spatially Resolving Ordered and Disordered Conformers and Photocurrent Generation in Intercalated Conjugated Polymer/Fullerene Blend Solar Cells. *Chemistry of materials : a publication of the American Chemical Society* 26:4395-404
163. Zuehlsdorff TJ, Isborn CM. 2018. Combining the ensemble and Franck-Condon approaches for calculating spectral shapes of molecules in solution. *J. Chem. Phys.* 148:024110
164. Li Z, Wong HC, Huang Z, Zhong H, Tan CH, et al. 2013. Performance enhancement of fullerene-based solar cells by light processing. *Nat. Commun.* 4:2227
165. Treat ND, Varotto A, Takacs CJ, Batara N, Al-Hashimi M, et al. 2012. Polymer-Fullerene Miscibility: A Metric for Screening New Materials for High-Performance Organic Solar Cells. *J. Am. Chem. Soc.* 134:15869-79
166. Zhang J, Shuan Tan H, Guo X, Facchetti A, Yan H. 2018. *Material Insights and Challenges for Non-fullerene Organic Solar Cells Based on Small Molecular Acceptors*.
167. Schwartz BJ. 2003. Conjugated Polymers as Molecular Materials: How Chain Conformation and Film Morphology Influence Energy Transfer and Interchain Interactions. *Annu. Rev. Phys. Chem.* 54:141-72
168. Clark J, Silva C, Friend RH, Spano FC. 2007. Role of Intermolecular Coupling in the Photophysics of Disordered Organic Semiconductors: Aggregate Emission in Regioregular Polythiophene. *Phys. Rev. Lett.* 98:206406
169. Heffner GW, Pearson DS. 1991. Molecular characterization of poly(3-hexylthiophene). *Macromolecules* 24:6295-9
170. Hu Z, Tenery D, Bonner MS, Gesquiere AJ. 2010. Correlation between spectroscopic and morphological properties of composite P3HT/PCBM nanoparticles studied by single particle spectroscopy. *Journal of Luminescence* 130:771-80
171. Xu B, Holdcroft S. 1993. Molecular control of luminescence from poly(3-hexylthiophenes). *Macromolecules* 26:4457-60
172. Tremel K, Ludwigs S. 2014. Morphology of P3HT in Thin Films in Relation to Optical and Electrical Properties. In *P3HT Revisited – From Molecular Scale to Solar Cell Devices*, ed. S Ludwigs:39-82. Berlin, Heidelberg: Springer Berlin Heidelberg. Number of 39-82 pp.
173. Sirringhaus H, Brown PJ, Friend RH, Nielsen MM, Bechgaard K, et al. 1999. Two-dimensional charge transport in self-organized, high-mobility conjugated polymers. *Nature* 401:685-8
174. Hallam T, Lee M, Zhao N, Nandhakumar I, Kemerink M, et al. 2009. Local Charge Trapping in Conjugated Polymers Resolved by Scanning Kelvin Probe Microscopy. *Phys. Rev. Lett.* 103:256803
175. Jimison LH, Toney MF, McCulloch I, Heeney M, Salleo A. 2009. Charge-Transport Anisotropy Due to Grain Boundaries in Directionally Crystallized Thin Films of Regioregular Poly(3-hexylthiophene). *Adv. Mater.* 21:1568-72

176. Rivnay J, Jimison LH, Northrup JE, Toney MF, Noriega R, et al. 2009. Large modulation of carrier transport by grain-boundary molecular packing and microstructure in organic thin films. *Nat. Mater.* 8:952
177. Sirringhaus H, Bird M, Zhao N. 2010. Charge Transport Physics of Conjugated Polymer Field-Effect Transistors. *Adv. Mater.* 22:3893-8
178. Redecker M, Bradley DDC, Inbasekaran M, Woo EP. 1999. Mobility enhancement through homogeneous nematic alignment of a liquid-crystalline polyfluorene. *Appl. Phys. Lett.* 74:1400-2
179. Sirringhaus H, Wilson RJ, Friend RH, Inbasekaran M, Wu W, et al. 2000. Mobility enhancement in conjugated polymer field-effect transistors through chain alignment in a liquid-crystalline phase. *Appl. Phys. Lett.* 77:406-8
180. Takacs CJ, Collins SD, Love JA, Mikhailovsky AA, Wynands D, et al. 2014. Mapping Orientational Order in a Bulk Heterojunction Solar Cell with Polarization-Dependent Photoconductive Atomic Force Microscopy. *ACS Nano* 8:8141-51
181. Ke T-H, Gehlhaar R, Chen C-H, Lin J-T, Wu C-C, Adachi C. 2009. High efficiency blue light emitting unipolar transistor incorporating multifunctional electrodes. *Appl. Phys. Lett.* 94:153307
182. Watts B, Schuettfort T, McNeill CR. 2011. Mapping of Domain Orientation and Molecular Order in Polycrystalline Semiconducting Polymer Films with Soft X-Ray Microscopy. *Adv. Funct. Mater.* 21:1122-31
183. Lu DY, Chen J, Deng SZ, Xu NS, Zhang WH. 2008. The most powerful tool for the structural analysis of tungsten suboxide nanowires: Raman spectroscopy. *J. Mater. Res.* 23:402-8
184. Gao Y, Grey JK. 2009. Resonance Chemical Imaging of Polythiophene/Fullerene Photovoltaic Thin Films: Mapping Morphology-Dependent Aggregated and Unaggregated C═C Species. *J. Am. Chem. Soc.* 131:9654-62
185. Gao Y, Martin TP, Thomas AK, Grey JK. 2010. Resonance Raman Spectroscopic- and Photocurrent Imaging of Polythiophene/Fullerene Solar Cells. *J. Phys. Chem. Lett.* 1:178-82
186. Tsoi WC, James DT, Kim JS, Nicholson PG, Murphy CE, et al. 2011. The Nature of In-Plane Skeleton Raman Modes of P3HT and Their Correlation to the Degree of Molecular Order in P3HT:PCBM Blend Thin Films. *J. Am. Chem. Soc.* 133:9834-43
187. Spano FC, Silva C. 2014. H- and J-Aggregate Behavior in Polymeric Semiconductors. *Annu. Rev. Phys. Chem.* 65:477-500
188. Kasha M, Rawls HR, Ashraf El-Bayoumi M. 1965. The exciton model in molecular spectroscopy. In *Pure Appl. Chem.*, p. 371
189. Spano FC. 2005. Modeling disorder in polymer aggregates: The optical spectroscopy of regioregular poly(3-hexylthiophene) thin films. *J. Chem. Phys.* 122:234701
190. Spano FC. 2010. The Spectral Signatures of Frenkel Polarons in H- and J-Aggregates. *Acc. Chem. Res.* 43:429-39
191. Spano FC, Yamagata H. 2011. Vibronic Coupling in J-Aggregates and Beyond: A Direct Means of Determining the Exciton Coherence Length from the Photoluminescence Spectrum. *J. Phys. Chem. B* 115:5133-43
192. Spano FC. 2006. Absorption in regio-regular poly(3-hexyl)thiophene thin films: Fermi resonances, interband coupling and disorder. *Chem. Phys.* 325:22-35

193. Mannanov AA, Bruevich VV, Feldman EV, Trukhanov VA, Pshenichnikov MS, Paraschuk DY. 2018. Real-Time Tracking of Polymer Crystallization Dynamics in Organic Bulk Heterojunctions by Raman Microscopy. *J. Phys. Chem. C* 122:19289-97
194. Zaumseil J, Kline RJ, Sirringhaus H. 2008. Electroluminescence imaging and microstructure of organic light-emitting field-effect transistors. *Appl. Phys. Lett.* 92:073304
195. Pingel P, Zen A, Abellón RD, Grozema FC, Siebbeles LDA, Neher D. 2010. Temperature-Resolved Local and Macroscopic Charge Carrier Transport in Thin P3HT Layers. *Adv. Funct. Mater.* 20:2286-95
196. Fatma D, Niko Van den B, Bruno Van M, Sabine B, Dirk V, et al. 2011. Isothermal crystallization of P3HT:PCBM blends studied by RHC. *J. Therm. Anal. Calorim.* 105:845-9
197. Siebbeles LDA, Huijser A, Savenije TJ. 2009. Effects of molecular organization on exciton diffusion in thin films of bioinspired light-harvesting molecules. *J. Mater. Chem.* 19:6067-72
198. Tennakone K, Pitigala PKDDP, Perera AGU. 2013. Exciton transport and electron mobility of organized aggregates of cationic dye thiocyanates. *RSC Adv.* 3:2770-5
199. Más-Montoya M, Janssen RAJ. 2017. The Effect of H- and J-Aggregation on the Photophysical and Photovoltaic Properties of Small Thiophene–Pyridine–DPP Molecules for Bulk-Heterojunction Solar Cells. *Adv. Funct. Mater.* 27:1605779
200. Hestand NJ, Spano FC. 2015. Interference between Coulombic and CT-mediated couplings in molecular aggregates: H- to J-aggregate transformation in perylene-based π-stacks. *J. Chem. Phys.* 143:244707
201. Hajduk B, Bednarski H, Jarząbek B, Janeczek H, Nitschke P. 2018. P3HT:PCBM blend films phase diagram on the base of variable-temperature spectroscopic ellipsometry. *Beilstein J. Nanotechnol.* 9:1108-15
202. Banach MJ, Friend RH, Sirringhaus H. 2003. Influence of the Molecular Weight on the Thermotropic Alignment of Thin Liquid Crystalline Polyfluorene Copolymer Films. *Macromolecules* 36:2838-44
203. Stewart ME, Anderton CR, Thompson LB, Maria J, Gray SK, et al. 2008. Nanostructured plasmonic sensors. *Chemical Reviews* 108:494-521
204. Koen KA, Weber ML, Mayer KM, Fernandez E, Willets KA. 2012. Spectrally-Resolved Polarization Anisotropy of Single Plasmonic Nanoparticles Excited by Total Internal Reflection. *The Journal of Physical Chemistry C* 116:16198-206
205. Marchuk K, Ha JW, Fang N. 2013. Three-dimensional high-resolution rotational tracking with superlocalization reveals conformations of surface-bound anisotropic nanoparticles. *Nano Lett.* 13:1245-50
206. Sweeney CM, Stender CL, Nehl CL, Hasan W, Shuford KL, Odom TW. 2011. Optical Properties of Tipless Gold Nanopyramids. *Small* 7:2032-6
207. Sonnichsen C, Alivisatos AP. 2005. Gold Nanorods as Novel Nonbleaching Plasmon-based Orientation Sensors for Polarized Single-Particle Microscopy. *Nano Lett.* 5:301-4
208. Ko SH, Park I, Pan H, Grigoropoulos CP, Pisano AP, et al. 2007. Direct nanoimprinting of metal nanoparticles for nanoscale electronics fabrication. *Nano Letters* 7:1869-77
209. Herderick ED, Tresback JS, Vasiliev AL, Padture NP. 2007. Template-directed synthesis, characterization and electrical properties of Au-TiO(2)-Au heterojunction nanowires. *Nanotechnology* 18

210. Bluemel A, Klug A, Eder S, Scherf U, Moderegger E, List EJW. 2007. Micromolding in capillaries and microtransfer printing of silver nanoparticles as soft-lithographic approach for the fabrication of source/drain electrodes in organic field-effect transistors. *Organic Electronics* 8:389-95
211. Ozbay E. 2006. Plasmonics: Merging photonics and electronics at nanoscale dimensions. *Science* 311:189-93
212. Oldenburg SJ, Jackson JB, Westcott SL, Halas NJ. 1999. Infrared extinction properties of gold nanoshells. *Applied Physics Letters* 75:2897-9
213. Maier SA, Atwater HA. 2005. Plasmonics: Localization and guiding of electromagnetic energy in metal/dielectric structures. *Journal of Applied Physics* 98
214. Bozhevolnyi SI, Volkov VS, Devaux E, Laluet JY, Ebbesen TW. 2006. Channel plasmon subwavelength waveguide components including interferometers and ring resonators. *Nature* 440:508-11
215. Yin LL, Vlasko-Vlasov VK, Pearson J, Hiller JM, Hua J, et al. 2005. Subwavelength focusing and guiding of surface plasmons. *Nano Letters* 5:1399-402
216. Lal S, Hafner JH, Halas NJ, Link S, Nordlander P. 2012. Noble Metal Nanowires: From Plasmon Waveguides to Passive and Active Devices. *Accounts of Chemical Research* 45:1887-95
217. Chang W-S, Lassiter JB, Swanglap P, Sobhani H, Khatua S, et al. 2012. A Plasmonic Fano Switch. *Nano Letters* 12:4977-82
218. Haes AJ, Haynes CL, McFarland AD, Schatz GC, Van Duyne RR, Zou SL. 2005. Plasmonic materials for surface-enhanced sensing and spectroscopy. *Mrs Bulletin* 30:368-75
219. Brolo AG, Gordon R, Leathem B, Kavanagh KL. 2004. Surface plasmon sensor based on the enhanced light transmission through arrays of nanoholes in gold films. *Langmuir* 20:4813-5
220. Liu JW, Lu Y. 2006. Fast colorimetric sensing of adenosine and cocaine based on a general sensor design involving aptamers and nanoparticles. *Angewandte Chemie-International Edition* 45:90-4
221. Lee J-S, Han MS, Mirkin CA. 2007. Colorimetric detection of mercuric ion (Hg2+) in aqueous media using DNA-functionalized gold nanoparticles. *Angewandte Chemie-International Edition* 46:4093-6
222. Haes AJ, Chang L, Klein WL, Van Duyne RP. 2005. Detection of a biomarker for Alzheimer's disease from synthetic and clinical samples using a nanoscale optical biosensor. *Journal of the American Chemical Society* 127:2264-71
223. Lin JY, Stuparu AD, Huntington MD, Mrksich M, Odom TW. 2013. Nanopatterned Substrates Increase Surface Sensitivity for Real-Time Biosensing. *The Journal of Physical Chemistry C* 117:5286-92
224. Chen J, Wang D, Xi J, Au L, Siekkinen A, et al. 2007. Immuno gold nanocages with tailored optical properties for targeted photothermal destruction of cancer cells. *Nano Letters* 7:1318-22
225. Loo C, Lowery A, Halas NJ, West J, Drezek R. 2005. Immunotargeted nanoshells for integrated cancer imaging and therapy. *Nano Letters* 5:709-11
226. Huang XH, El-Sayed IH, Qian W, El-Sayed MA. 2006. Cancer cell imaging and photothermal therapy in the near-infrared region by using gold nanorods. *Journal of the American Chemical Society* 128:2115-20

227. Lee K-S, El-Sayed MA. 2006. Gold and silver nanoparticles in sensing and imaging: Sensitivity of plasmon response to size, shape, and metal composition. *Journal of Physical Chemistry B* 110:19220-5
228. Kelly KL, Coronado E, Zhao LL, Schatz GC. 2003. The optical properties of metal nanoparticles: The influence of size, shape, and dielectric environment. *Journal of Physical Chemistry B* 107:668-77
229. Murphy CJ, Sau TK, Gole A, Orendorff CJ. 2005. Surfactant-directed synthesis and optical properties of one-dimensional plasmonic metallic nanostructures. *Mrs Bulletin* 30:349-55
230. Stoerzinger KA, Lin JY, Odom TW. 2011. Nanoparticle SERS substrates with 3D Raman-active volumes. *Chemical Science* 2:1435-9
231. Suh JY, Huntington MD, Kim CH, Zhou W, Wasielewski MR, Odom TW. 2011. Extraordinary Nonlinear Absorption in 3D Bowtie Nanoantennas. *Nano Letters* 12:269-74
232. Gao H, Hyun JK, Lee MH, Yang J-C, Lauhon LJ, Odom TW. 2010. Broadband Plasmonic Microlenses Based on Patches of Nanoholes. *Nano Lett.* 10:4111-6
233. Yang J-C, Gao H, Suh JY, Zhou W, Lee MH, Odom TW. 2010. Enhanced Optical Transmission Mediated by Localized Plasmons in Anisotropic, Three-Dimensional Nanohole Arrays. *Nano Lett.* 10:3173-8
234. Hoffman R, Gross L. 1970. Reflected-light differential-interference microscopy: principles, use and image interpretation. *J. Microsc-Oxford* 91:149-72
235. Tsunoda M, Isailovic D, Yeung ES. 2008. Real-time three-dimensional imaging of cell division by differential interference contrast microscopy. *J. Microsc-Oxford* 232:207-11
236. Sun W, Fang N, Trewyn BG, Tsunoda M, Slowing II, et al. 2008. Endocytosis of a single mesoporous silica nanoparticle into a human lung cancer cell observed by differential interference contrast microscopy. *Analytical and Bioanalytical Chemistry* 391:2119-25
237. Sun W, Wang GF, Fang N, Yeung ES. 2009. Wavelength-Dependent Differential Interference Contrast Microscopy: Selectively Imaging Nanoparticle Probes in Live Cells. *Analytical Chemistry* 81:9203-8
238. Stender AS, Wang GF, Sun W, Fang N. 2010. Influence of Gold Nanorod Geometry on Optical Response. *Acs Nano* 4:7667-75
239. Wang GF, Sun W, Luo Y, Fang N. 2010. Resolving rotational motions of nano-objects in engineered environments and live cells with gold nanorods and differential interference contrast microscopy. *J. Am. Chem. Soc.* 132:16417-22
240. Gu Y, Sun W, Wang GF, Fang N. 2011. Single Particle Orientation and Rotation Tracking Discloses Distinctive Rotational Dynamics of Drug Delivery Vectors on Live Cell Membranes. *Journal of the American Chemical Society* 133:5720-3
241. Gu Y, Sun W, Wang G, Jeftinija K, Jeftinija S, Fang N. 2012. Rotational dynamics of cargos at pauses during axonal transport. *Nature Communications* 3
242. Wang G, Sun W, Luo Y, Fang N. 2010. Resolving rotational motions of nano-objects in engineered environments and live cells with gold nanorods and differential interference contrast microscopy. *J. Am. Chem. Soc.* 132:16417-22
243. Yakar O, Balci O, Uzlu B, Polat N, Ari O, et al. 2020. Hybrid J-Aggregate–Graphene Phototransistor. *ACS Applied Nano Materials* 3:409-17

244. Yi D, Jeon S, Hong SW. 2018. Selectively Patterned Regrowth of Bilayer Graphene for Self-Integrated Electronics by Sequential Chemical Vapor Deposition. *ACS Applied Materials & Interfaces* 10:40014-23
245. Roddaro S, Pingue P, Piazza V, Pellegrini V, Beltram F. 2007. The Optical Visibility of Graphene: Interference Colors of Ultrathin Graphite on SiO2. *Nano Lett.* 7:2707-10
246. Masubuchi S, Machida T. 2019. Classifying optical microscope images of exfoliated graphene flakes by data-driven machine learning. *npj 2D Materials and Applications* 3:4
247. Vaupel M, Dutschke A, Wurstbauer U, Hitzel F, Pasupathy A. 2013. Topography, complex refractive index, and conductivity of graphene layers measured by correlation of optical interference contrast, atomic force, and back scattered electron microscopy. *J. Appl. Phys.* 114:183107
248. Wang YY, Ni ZH, Shen ZX, Wang HM, Wu YH. 2008. Interference enhancement of Raman signal of graphene. *Appl. Phys. Lett.* 92:043121
249. Ferrari AC, Meyer JC, Scardaci V, Casiraghi C, Lazzeri M, et al. 2006. Raman Spectrum of Graphene and Graphene Layers. *Phys. Rev. Lett.* 97:187401
250. Casiraghi C, Hartschuh A, Qian H, Piscanec S, Georgi C, et al. 2009. Raman Spectroscopy of Graphene Edges. *Nano Lett.* 9:1433-41
251. Casiraghi C, Pisana S, Novoselov KS, Geim AK, Ferrari AC. 2007. Raman fingerprint of charged impurities in graphene. *Appl. Phys. Lett.* 91:233108
252. Dresselhaus MS, Jorio A, Hofmann M, Dresselhaus G, Saito R. 2010. Perspectives on Carbon Nanotubes and Graphene Raman Spectroscopy. *Nano Lett.* 10:751-8
253. Ferrari AC, Basko DM. 2013. Raman spectroscopy as a versatile tool for studying the properties of graphene. *Nat. Nanotechnol.* 8:235-46
254. Graf D, Molitor F, Ensslin K, Stampfer C, Jungen A, et al. 2007. Spatially Resolved Raman Spectroscopy of Single- and Few-Layer Graphene. *Nano Lett.* 7:238-42
255. Hao Y, Wang Y, Wang L, Ni Z, Wang Z, et al. 2010. Probing Layer Number and Stacking Order of Few-Layer Graphene by Raman Spectroscopy. *Small* 6:195-200
256. Malard LM, Pimenta MA, Dresselhaus G, Dresselhaus MS. 2009. Raman spectroscopy in graphene. *Physics Reports* 473:51-87
257. Cançado LG, Jorio A, Ferreira EHM, Stavale F, Achete CA, et al. 2011. Quantifying Defects in Graphene via Raman Spectroscopy at Different Excitation Energies. *Nano Lett.* 11:3190-6
258. Eckmann A, Felten A, Mishchenko A, Britnell L, Krupke R, et al. 2012. Probing the Nature of Defects in Graphene by Raman Spectroscopy. *Nano Lett.* 12:3925-30
259. Beams R, Gustavo Cançado L, Novotny L. 2015. Raman characterization of defects and dopants in graphene. *Journal of Physics: Condensed Matter* 27:083002
260. Wu J-B, Wang H, Li X-L, Peng H, Tan P-H. 2016. Raman spectroscopic characterization of stacking configuration and interlayer coupling of twisted multilayer graphene grown by chemical vapor deposition. *Carbon* 110:225-31
261. Poncharal P, Ayari A, Michel T, Sauvajol JL. 2009. Effect of rotational stacking faults on the Raman spectra of folded graphene. *Phys. Rev. B* 79:195417
262. Puretzky AA, Liang L, Li X, Xiao K, Wang K, et al. 2015. Low-Frequency Raman Fingerprints of Two-Dimensional Metal Dichalcogenide Layer Stacking Configurations. *ACS Nano* 9:6333-42
263. Liu K, Zhang L, Cao T, Jin C, Qiu D, et al. 2014. Evolution of interlayer coupling in twisted molybdenum disulfide bilayers. *Nat. Commun.* 5:4966

264. Yeh C-H, Lin Y-C, Nayak PK, Lu C-C, Liu Z, et al. 2014. Probing interlayer coupling in twisted single-crystal bilayer graphene by Raman spectroscopy. *Journal of Raman Spectroscopy* 45:912-7
265. Ni Z, Liu L, Wang Y, Zheng Z, Li L-J, et al. 2009. G-band Raman double resonance in twisted bilayer graphene: Evidence of band splitting and folding. *Phys. Rev. B* 80:125404
266. Yao W, Wang E, Bao C, Zhang Y, Zhang K, et al. 2018. Quasicrystalline 30° twisted bilayer graphene as an incommensurate superlattice with strong interlayer coupling. *Proc. Natl. Acad. Sci. USA* 115:6928
267. Lee CC, Suzuki S, Xie W, Schibli TR. 2012. Broadband graphene electro-optic modulators with sub-wavelength thickness. *Opt. Express* 20:5264-9
268. Balandin AA. 2011. Thermal properties of graphene and nanostructured carbon materials. *Nat. Mater.* 10:569-81
269. Frank IW, Tanenbaum DM, van der Zande AM, McEuen PL. 2007. Mechanical properties of suspended graphene sheets. *Journal of Vacuum Science & Technology B: Microelectronics and Nanometer Structures Processing, Measurement, and Phenomena* 25:2558-61
270. Nagal V, Li T, Khurgin JB, Gracias DH. 2020. Large-Area Arrays of Quasi-3D Au Nanostructures for Polarization-Selective Mid-Infrared Metasurfaces. *ACS Applied Nano Materials* 3:7029-39
271. Barnes WL, Dereux A, Ebbesen TW. 2003. Surface plasmon subwavelength optics. *Nature* 424:824-30
272. Suh JY, Huntington MD, Kim CH, Zhou W, Wasielewski MR, Odom TW. 2012. Extraordinary Nonlinear Absorption in 3D Bowtie Nanoantennas. *Nano Lett.* 12:269-74
273. Henzie J, Lee J, Lee MH, Hasan W, Odom TW. 2009. Nanofabrication of Plasmonic Structures. *Annu. Rev. Phys. Chem.* 60:147-65
274. Zhao L, Kelly KL, Schatz GC. 2003. The Extinction Spectra of Silver Nanoparticle Arrays: Influence of Array Structure on Plasmon Resonance Wavelength and Width. *J. Phys. Chem. B* 107:7343-50
275. Haynes CL, McFarland AD, Zhao L, Van Duyne RP, Schatz GC, et al. 2003. Nanoparticle Optics: The Importance of Radiative Dipole Coupling in Two-Dimensional Nanoparticle Arrays. *J. Phys. Chem. B* 107:7337-42
276. Gramotnev DK, Bozhevolnyi SI. 2010. Plasmonics beyond the diffraction limit. *Nat. Photonics* 4:83-91
277. Kawata S, Ono A, Verma P. 2008. Subwavelength colour imaging with a metallic nanolens. *Nat. Photonics* 2:438-42
278. Kawata S, Inouye Y, Verma P. 2009. Plasmonics for near-field nano-imaging and superlensing. *Nat. Photonics* 3:388-94
279. Atwater HA, Polman A. 2010. Plasmonics for improved photovoltaic devices. In *Materials for Sustainable Energy*:1-11: Co-Published with Macmillan Publishers Ltd, UK. Number of 1-11 pp.
280. Kelzenberg MD, Boettcher SW, Petykiewicz JA, Turner-Evans DB, Putnam MC, et al. 2010. Enhanced absorption and carrier collection in Si wire arrays for photovoltaic applications. *Nat. Mater.* 9:239-44
281. Li SQ, Guo P, Zhang L, Zhou W, Odom TW, et al. 2011. Infrared Plasmonics with Indium–Tin-Oxide Nanorod Arrays. *ACS Nano* 5:9161-70

282. Chýlek P, Zhan J. 1990. Absorption and scattering of light by small particles: the interference structure. *Appl. Optics* 29:3984-
283. Stender AS, Marchuk K, Liu C, Sander S, Meyer MW, et al. 2013. Single Cell Optical Imaging and Spectroscopy. *Chem. Rev.* 113:2469-527
284. Gu Y, Sun W, Wang G, Fang N. 2011. Single Particle Orientation and Rotation Tracking Discloses Distinctive Rotational Dynamics of Drug Delivery Vectors on Live Cell Membranes. *J. Am. Chem. Soc.* 133:5720-3
285. Gu Y, Sun W, Wang G, Jeftinija K, Jeftinija S, Fang N. 2012. Rotational dynamics of cargos at pauses during axonal transport. *Nat. Commun.* 3:1030
286. Mehta SB, Sheppard CJR. 2008. Partially coherent image formation in differential interference contrast (DIC) microscope. *Opt. Express* 16:19462-79
287. Swaminathan R, Hoang CP, Verkman AS. 1997. Photobleaching recovery and anisotropy decay of green fluorescent protein GFP-S65T in solution and cells: Cytoplasmic viscosity probed by green fluorescent protein translational and rotational diffusion. *Biophys. J.* 72:1900-7
288. Ha T, Laurence TA, Chemla DS, Weiss S. 1999. Polarization spectroscopy of single fluorescent molecules. *J. Phys. Chem. B* 103:6839-50
289. Salamon Z, Tollin G. 2001. Optical anisotropy in lipid bilayer membranes: Coupled plasmon-waveguide resonance measurements of molecular orientation, polarizability, and shape. *Biophys. J.* 80:1557-67
290. Bohmer M, Enderlein J. 2003. Orientation imaging of single molecules by wide-field epifluorescence microscopy. *J. Opt. Soc. Am. B* 20:554-9
291. Patra D, Gregor I, Enderlein J, Sauer M. 2005. Defocused imaging of quantum-dot angular distribution of radiation. *Appl. Phys. Lett.* 87
292. Toprak E, Enderlein J, Syed S, McKinney SA, Petschek RG, et al. 2006. Defocused orientation and position imaging (DOPI) of myosin V. *Proc. Natl. Acad. Sci. USA* 103:6495-9
293. Uji-i H, Melnikov SM, Deres A, Bergamini G, De Schryver F, et al. 2006. Visualizing spatial and temporal heterogeneity of single molecule rotational diffusion in a glassy polymer by defocused wide-field imaging. *Polymer* 47:2511-8
294. Stender AS, Wang G, Sun W, Fang N. 2010. Influence of gold nanorod geometry on optical response. *ACS Nano* 4:7667-75
295. Wei L, Xu J, Ye Z, Zhu X, Zhong M, et al. 2016. Orientational imaging of a single gold nanorod at the liquid/solid interface with polarized evanescent field illumination. *Anal. Chem.* 88:1995-9
296. Xiao L, Qiao Y, He Y, Yeung ES. 2010. Three dimensional orientational imaging of nanoparticles with darkfield microscopy. *Anal. Chem.* 82:5268-74
297. Xiao L, Qiao Y, He Y, Yeung ES. 2011. Imaging translational and rotational diffusion of single anisotropic nanoparticles with planar illumination microscopy. *J. Am. Chem. Soc.* 133:10638–45
298. Ha JW, Sun W, Wang G, Fang N. 2011. Differential interference contrast polarization anisotropy for tracking rotational dynamics of gold nanorods. *Chem. Commun.* 47:7743-5
299. Gu Y, Sun W, Wang G, Jeftinija K, Jeftinija S, Fang N. 2012. Rotational dynamics of cargos at pauses during axonal transport. *Nat. Commun.* 3:1030

300. Yildiz A, Forkey JN, McKinney SA, Ha T, Goldman YE, Selvin PR. 2003. Myosin V walks hand-over-hand: single fluorophore imaging with 1.5-nm localization. *Science* 300:2061-5
301. Enderlein J, Toprak E, Selvin PR. 2006. Polarization effect on position accuracy of fluorophore localization. *Opt. Express* 14:8111-20
302. Mortensen KI, Churchman LS, Spudich JA, Flyvbjerg H. 2010. Optimized localization analysis for single-molecule tracking and super-resolution microscopy. *Nat. Methods* 7:377-81
303. Lew MD, Backlund MP, Moerner WE. 2013. Rotational mobility of single molecules affects localization accuracy in super-resolution fluorescence microscopy. *Nano Lett.* 13:3967-72
304. Titus EJ, Willets KA. 2013. Superlocalization surface-enhanced Raman scattering microscopy: comparing point spread function models in the ensemble and single-molecule limits. *ACS Nano* 7:8284-94
305. Gelles J, Schnapp BJ, Sheetz MP. 1988. Tracking kinesin-driven movements with nanometre-scale precision. *Nature* 331:450-3
306. Gu Y, Di X, Sun W, Wang G, Fang N. 2012. Three-dimensional super-localization and tracking of single gold nanoparticles in cells. *Anal. Chem.* 84:4111-7
307. Gu Y, Wang G, Fang N. 2013. Simultaneous Single-Particle Superlocalization and Rotational Tracking. *ACS Nano* 7:1658-65
308. Rasband WS. http://imagej.nih.gov/ij/, 1997-2016.
309. Preza C, Snyder DL, Conchello JA. 1999. Theoretical development and experimental evaluation of imaging models for differential-interference-contrast microscopy. *J. Opt. Soc. Am. A* 16:2185-99
310. Yildiz A, Selvin PR. 2005. Fluorescence imaging with one manometer accuracy: Application to molecular motors. *Acc. Chem. Res.* 38:574-82
311. Yildiz A, Tomishige M, Vale RD, Selvin PR. 2004. Kinesin walks hand-over-hand. *Science* 303:676-8
312. Xiao L, Ha JW, Wei L, Wang G, Fang N. 2012. Determining the full three-dimensional orientation of single anisotropic nanoparticles by differential interference contrast microscopy. *Angew. Chem. Int. Ed.* 51:7734-8
313. Shribak M, Inoué S. 2006. Orientation-independent differential interference contrast microscopy. *Appl. Optics* 45:460-9
314. Pluta M. 1989. *Advanced Light Microscopy*. pp 168. Elsevier Science Publishing CO., INC
315. Shribak M. 2013. Quantitative orientation-independent DIC microscope with fast switching shear direction and bias modulation. *J. Opt. Soc. Am. A* 30:769-82
316. Shribak M, Inoué S. 2008. Orientation-independent differential interference contrast microscopy. In *Collected Works of Shinya Inoué*:953-62: WORLD SCIENTIFIC. Number of 953-62 pp.
317. Shribak M. 2013. Quantitative orientation-independent differential interference contrast microscope with fast switching shear direction and bias modulation. *Journal of the Optical Society of America. A, Optics, image science, and vision* 30:769-82
318. Van Munster EB, Van Vliet LJ, Aten JA. 1997. Reconstruction of optical pathlength distributions from images obtained by a wide-field differential interference contrast microscope. *J. Microsc-Oxford* 188:149-57